UNIVERSIDADE TÉCNICA DE LISBOA

INSTITUTO SUPERIOR TÉCNICO

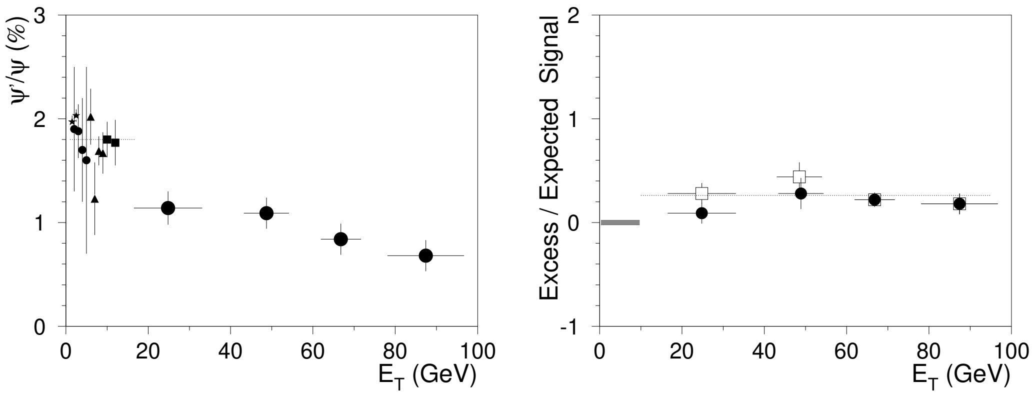

J/ψ, ψ' and dimuon production in p–A and S–U collisions at 200 GeV / nucleon

Carlos Manuel A. L. Lourenço

(Licenciado em Física)

Tese de doutoramento para obtenção do grau de Doutor em Física

Janeiro de 1995

Juri:
Jorge Dias de Deus
Louis Kluberg (arguente)
José Mariano Gago
Helmut Satz
Peter Sonderegger
João Varela (arguente)

To my parents, my wife and my children

"The time has come," the Walrus said,
"To talk of many things:
Of shoes — and ships — and sealing wax —
Of cabbages — and kings —
And why the sea is boiling hot —
And whether pigs have wings."

— Lewis Carroll, *Alice's Adventures in Wonderland* (1865)

Abstract

We report on the production of intermediate and high mass muon pairs in p–W, p–U and S–U collisions, at beam momentum of 200 GeV per incident nucleon, as measured by the NA38 experiment at the CERN SPS.

From the analysis of the S–U data collected in 1990 and 1991, we have obtained results on the dimuon mass region above the J/ψ resonance. Besides the study of the ψ' behaviour, identifying the high mass continuum with Drell–Yan dimuons provides a baseline for the study of the intermediate mass region (IMR) continuum and a cleaner reference in the J/ψ suppression studies.

The study of the IMR continuum, where thermal production is sought for, is notably more difficult than the studies of the resonance regions. Both because it is ambiguous to disentangle two or three processes contributing to a continuum (while the resonances are prominent features of the mass spectra) and because of its sensitivity to a correct combinatorial background subtraction.

In this work, the dimuon mass spectra (above 1.5 GeV) produced in proton–nucleus and nucleus–nucleus collisions, is compared to the expectations from conventional sources: the J/ψ and ψ' resonances, decaying into muon pairs, the Drell–Yan mechanism and the contribution from the semi-leptonic decays of charmed mesons.

Besides presenting absolute cross sections for J/ψ, ψ' and Drell–Yan production, an estimation of the total charm production cross section in nucleon–nucleon collisions is derived (under certain hypothesis) from the p–A results and compared to the direct measurements of other experiments.

The main results are the following. In S–U collisions, the ratio between ψ' and J/ψ yields decreases as the transverse energy released in the collision, E_{T}, increases. The integrated values also show a decrease of this ratio when going from p–W or p–U to S–U interactions. The p–A intermediate mass continuum is well explained by the superposition of the Drell–Yan and charm contributions. In the S–U data, however, the observed signal is significantly larger than what is expected from a linear extrapolation of the proton–nucleus results.

Key words

Dimuon production; Ultra-relativistic Heavy Ion Collisions; J/ψ and ψ' suppression; J/ψ, ψ' and Drell–Yan cross–sections; Charm production; Intermediate Mass Region 'Excess'; Quark Gluon Plasma

Resumo

Neste trabalho abordamos a produção de pares de muões de massa intermédia e alta, em colisões p–W, p–U e S–U, com feixes de impulsão 200 GeV por cada nucleão incidente, de acordo com as medições efectuadas pela experiência NA38, no acelerador SPS, do CERN.

A partir da análise dos dados S–U colhidos em 1990 e 1991, obtiveram-se resultados correspondentes à região de massa acima da ressonância J/ψ. Para além do estudo do comportamento do ψ', identificando o contínuo de alta massa com dimuões Drell–Yan fornece uma linha de base para o estudo do contínuo da região de massa intermédia (IMR) e uma referência mais limpa nos estudos da supressão do J/ψ.

O estudo do contínuo IMR, onde se procuram sinais da produção de dimuões térmicos, é sensivelmente mais difícil do que o estudo das regiões das ressonâncias. Por causa da ambiguidade na separação de dois ou três processos que contribuem para um contínuo (enquanto que as ressonâncias sobressaiem do espectro em massa) e por causa da sua sensibilidade a uma correcta subtração do fundo combinatorial.

Neste trabalho, o espectro em massa dos dimuões (acima de 1.5 GeV) produzido em colisões protão–núcleo e núcleo–núcleo, é comparado com o que se espera de fontes convencionais: as ressonâncias J/ψ e ψ', decaindo em pares de muões, o mecanismo Drell–Yan e a contribuição dos decaimentos semi-leptónicos dos mesões D e $\bar{D}$.

Para além de apresentarmos secções eficazes absolutas para a produção de J/ψ, ψ' e Drell–Yan, uma estimativa da secção eficaz total de produção de charme em colisões nucleão–nucleão é derivada (mediante certas hipoteses) dos resultados p–A e comparada com as medições directas efectuadas por outras experiências.

Os resultados principais são os seguintes. Em colisões S–U, a razão entre as taxas de produção de ψ' e J/ψ diminui à medida que a energia transversa libertada na colisão, E_{T}, aumenta. Os valores integrados também evidenciam um decréscimo desta razão entre interacções p–W ou p–U e S–U. O contínuo na região de massa intermédia é bem compreendido como uma sobreposição das contribuições Drell–Yan e charme. Nos dados S–U, no entanto, o sinal observado é superior ao que se esperaria com base na extrapolação linear dos resultados protão–núcleo.

Palavras chave

Produção de dimuões; Colisões de Iões Pesados Ultra-relativísticos; Supressão do J/ψ e do ψ'; Secções eficazes de produção de J/ψ, ψ' e Drell–Yan; Produção de charme; 'Excesso' na Região de Massa Intermédia; Plasma de Quarks e Gluões

Acknowledgments

It gives me great pleasure to thank the many people that contributed to the preparation of this work.

I would like to start by thanking all the NA38 collaborators, specially Jean Castor, Jacques Fargeix, Paul Force and Roger Haroutunian, for the many discussions concerning some of the information used in this work, Bernard Chaurand, Olivier Drapier, Claudie Gerschel, Louis Kluberg and Albert Romana, for the lively discussions on the analysis methods used and on the results obtained, and the LIP group, coordinated by Paula Bordalo and Siocha Ramos, for providing the logistic framework where most of my work was done. Working together with all these people, for the last 8 years, has been a very fruitful experience, which I am looking forward to pursue. The valuable guidance of João Varela and Peter Sonderegger should be noticeable through the present text and is deeply appreciated.

I want to thank the help provided by Fernando Barão, René Brun, Lau Gatignon, Jorge Gomes, Paulo Gomes, Fred James, Hatti Plothow-Besch and Torbjörn Sjöstrand. Some very useful discussions with Ivan Králik and Georges London, from the HELIOS-3 collaboration, Rob Veenhof, from the HELIOS-1 collaboration, and Itzhak Tserruya, from the CERES collaboration, are also acknowledged.

A special word of thanks goes to the following people, for several reasons but, above all, for their friendship: Gaspar Barreira, José Mariano Gago, Hans Gutbrod, Louis Kluberg, Gilbert Landaud, Engelbert Quack, Helmut Satz, Jurgen Schukraft, Peter Sonderegger, Hans Specht, João Varela, Rob Veenhof, Glenn Young and Bill Zajc.

The financial support of LIP (Laboratório de Instrumentação e Física Experimental de Partículas) and JNICT (Junta Nacional de Investigação Científica e Tecnológica) is gratefully acknowledged.

Contents

Abstract **vii**

Resumo **ix**

Acknowledgments **xi**

Introduction **1**

1 Review of previous knowledge **5**

1.1 General overview of QGP physics 5
1.2 QGP signatures 7
1.3 Thermal production of dimuons and photons 8
1.4 Strangeness enhancement 9
1.5 Charmonia suppression 10
1.6 Open charm production 12
1.7 General overview of dilepton physics 13
1.8 Drell-Yan process 14
1.9 Hadroproduction of J/ψ and ψ' 20
1.10 Open charm hadroproduction 21
1.11 Dimuons from charm decays 23

2 The NA38 experiment **29**

2.1 Design strategy 30
2.2 Apparatus overview 32
2.3 Detailed description 33
2.3.1 Beam 33
2.3.2 Target region 35
2.3.3 Electromagnetic calorimeter 36
2.3.4 Muon spectrometer 38
2.3.4.1 Hadron absorbers 38
2.3.4.2 Magnet 39
2.3.4.3 Detectors 40
2.3.4.4 Alignment 42

2.3.4.5 Mass resolution 43
2.4 Trigger 43
2.5 Data-acquisition system 44

3 Data reduction and normalization 47
3.1 Data taking periods and setup description 47
3.2 Event selection and luminosity calculations 48
3.3 Kinematical region studied 51
3.4 The 'image' cut 52
3.5 Efficiency of sub-target identification 53

4 Processes contributing to the dimuon mass spectra 55
4.1 Simulation of the signal processes 55
4.2 Acceptances 58
4.3 Functional forms representing the signal contributions 62
4.3.1 The J/ψ line shape 63
4.3.2 The ψ' line shape 65
4.3.3 The Drell–Yan and D$\bar{\mathrm{D}}$ mass spectra 66
4.4 Combinatorial Background 68

5 Data analysis of the high and intermediate mass regions 75
5.1 Alternative ways to study the signal 75
5.1.1 Do not consider the background 75
5.1.2 Get the signal directly 76
5.1.3 Simultaneous fit of opposite-sign and like-sign distributions . 76
5.1.4 Consider the meson decays as a signal contribution 77
5.2 E_{T} distributions and vertex efficiency correction in S–U collisions . 78
5.2.1 Differences between data sets 78
5.2.2 Definition of the 4 E_{T} classes 79
5.2.3 Vertex efficiency correction in the mass distributions 80
5.2.3.1 No correction at all 80
5.2.3.2 Event per event correction 80
5.2.3.3 Check for some mass dependence 81
5.2.3.4 Global correction on the fitting functions 83
5.2.3.5 Like-sign versus opposite-sign correction 83
5.3 Relative results in the High Mass Region 85
5.3.1 p–W, p–U and S–U (integrated in E_{T}) 85
5.3.1.1 Results from each data set 86
5.3.1.2 Results from a simultaneous fit 86
5.3.2 Comparison with previous measurements 89
5.3.3 Relative A-dependences 89
5.3.4 S–U results in 4 E_{T} bins 90
5.4 Absolute cross sections in the HMR 92

5.4.1 Drell-Yan cross-sections and K factors 93
5.4.2 J/ψ and ψ' cross sections 93
5.4.3 Comparison with previous measurements 94
5.5 The Intermediate Mass Region in p–A collisions 95
5.5.1 Relative studies 95
5.5.2 Absolute studies 96
5.5.3 Comparison with previous direct measurements 97
5.6 The IMR in S–U interactions 98
5.6.1 S-U excess relative to p–A linear extrapolation 98
5.6.2 Quantification: measured over expected signal 99
5.7 Systematical uncertainties 100
5.8 Interpretation of the results 101
5.8.1 The ψ' suppression 101
5.8.2 The IMR continuum enhancement 102

Concluding remarks **107**

List of Tables

1.1 'K factors' previously measured at energies similar to NA38's. . . . 16

1.2 Values of $B\sigma$ ($x_F > 0$) for J/ψ production, as a function of the energy of the incident protons. [Data taken from Bad 83, Bra 77, And 79a and Ant 92] 20

2.1 Detector components of the muon spectrometer. The z scale, inherited from NA10, starts 45 cm downstream of the target center (see figure 2.4). 41

3.1 Target configurations. The number of sub-targets is followed by their dimensions (in mm). W: length and diameter; U: x, y and z dimensions. 48

3.2 Parameters for the luminosity calculations. 52

4.1 $\sigma_{pn}^{c\bar{c}}$ (in μb) from Pythia at $E_{\mathrm{Lab}} = 200$ GeV, versus the structure functions parametrization and m_c. 57

4.2 $\sigma_{pn}^{c\bar{c}}$ (in μb) from Pythia at $E_{Lab} = 200$ GeV, for *GRV LO* versus m_c and k_{T} 57

4.3 $\sigma_{pp}^{c\bar{c}}$ (in μb) from Pythia versus S.F., m_c and E_{Lab}. 57

4.4 μ and σ values (in GeV) obtained by fitting a gaussian to the J/ψ peak in both the experimental and simulated mass spectra. 64

4.5 Ratios between the amount of background (integrated in two different mass regions) and J/ψ events. 73

4.6 Ratios between the amount of background (in the 1.5–2.5 GeV mass region) and the integrated luminosity of the corresponding data set. 73

5.1 Mean values (and RMS) per ΔE_{T} slice and data set, obtained from the signal E_{T} distribution (without any cut on the mass of the muon pair). 79

5.2 Difference between the 'global' and the 'event by event' vertex efficiency correction methods. These (mean) values correspond to the opposite-sign events of mass greater than 3 GeV, collected in the SU 91 Psi. 82

5.3 Mean values of ϵ_v (in %) in three different mass ranges: 3.0–3.5 GeV (J/ψ); 3.5–4.1 GeV (ψ'); 4.1–5.5 GeV (DY). These values correspond to the opposite-sign events collected in the SU 91 Psi data set. . . . 82
5.4 Mean values of ϵ_v (in %) for the opposite-sign and like-sign events collected in the SU 91 Psi data set (and their ratio). 84
5.5 Values of the ratios ψ'/ψ and ψ/DY obtained by fitting each data set independently. 86
5.6 Results from the simultaneous fit to all the data sets of each projectile–target combination. N^{DY} is the (total) number of Drell–Yan events, corrected for acceptances and ϵ_v efficiency. 87
5.7 Values of the ratio ψ'/ψ obtained with several targets and energies. 89
5.8 Values of the ratios ψ'/ψ and ψ/DY obtained for each ΔE_{T} bin. . . 91
5.9 Values of several centrality estimators, alternative to E_{T}. 92
5.10 The Drell–Yan K factor in p–W and S–U collisions. 93
5.11 Total number of J/ψ and ψ' events, corrected for acceptances and ϵ_v efficiency. 94
5.12 J/ψ and ψ' cross–sections, times their branching ratio into muons, within our phase space window: $3 < y_{\mathrm{lab}} < 4$, $|\cos(\theta)| < 0.5$. 94
5.13 Values of R^{Bg} per ΔE_{T} bin, if we assume that the 'excess' must be either charm or background. D/S are the corresponding values for the ratio between the measured 'data' and the expected 'sources'. . 103

List of Figures

1.1 *a)* $\mu - T$ phase diagram, showing the HG and QGP regions. *b)* Energy density and pressure, in units of T^4, versus temperature, in units of T_c, through the phase transition region. [Figure taken from Son 93] 6

1.2 The ratio ϕ / $(\rho + \omega)$ as measured by the HELIOS-3 and NA38 experiments. The horizontal line represents 2.5 times the p–W value. [Figure taken from Lou 94b] 10

1.3 The evolution in time of the number of publications refering to the 'J/ψ suppression' topic. [Figure prepared with the help of David Dallman, from CERN's Library.] 11

1.4 $M_{\mu\mu}$ and $M_{\mu\mu\gamma}$ distributions from p–Be collisions at 450 GeV, as measured by the HELIOS-1 experiment. The Dalitz decays dominate the signal up to $M_{\mu\mu} \sim 0.7$ GeV. [Figure taken from Vee 93] 14

1.5 Mean p_{T} values for p–A and π–A dimuons, versus M. [Figure redone from Gro 86] 16

1.6 α as a function of M and of p_{T}, as measured by the E288 experiment. [Figures taken from Ito 81] 18

1.7 Ratio of the dimuon cross sections versus M. *a)* π^+ over π^-. *b)* π^- over proton. [Figures taken from Str 81] 19

1.8 a) p–A values of ψ'/ψ, ratio of cross–sections times branching ratios, measured by several experiments. b) J/ψ and ψ' production reveal the same A-dependence in the E772 experiment [Ald 91]. 21

1.9 Charm production cross–sections, in nucleon–nucleon interactions, as a function of incident energy. [Figure inspired on Ber 88 with more data points] 22

1.10 Cross section times branching ratio for D^+ and D^0 production as a function of A. [Figure redone from App 92] 23

1.11 Dimuon mass and missing energy distributions measured by the HELIOS-1 experiment. The shaded area represents the charm contribution expected from a Monte Carlo based on PYTHIA, normalized to the EHS cross section measurement. [Figures taken from Aub 93] . 24

2.1 Overview of the NA38 detector: target region, muon filter, chambers (MWPC), hodoscopes (R), magnet, iron wall. 29
2.2 Layout of the muon spectrometer. 32
2.3 Schematic view of the NA38 beam line. [Courtesy of L. Gatignon] . 33
2.4 Overview of the target region. The center of the NA38 target is placed 45 cm upstream from the location of the NA10 target position ($z = 0$). 35
2.5 Field map in the transverse plane of the magnet (left) and along the z axis (right). B values are shown in the *air* sectors (top), for $r = 50$, 75 and 100 cm — leading to $\int B\,dl$ values of 1.89, 1.26 and 0.95 T m — and in the *iron* sectors (bottom), for $r = 75$ cm. 39
2.6 Trigger hodoscopes information in a typical p–A event. 42
2.7 Chambers information for the same event as figure 2.6. 42

3.1 Configurations of the 'pre-dump' absorber materials as parametrized in the simulation and reconstruction programs. The dashed arrows show the angular acceptance of the spectrometer (35 to 120 m rad), while the solid arrows represent the start of the 'NA10' muon filter. The calorimeter is identified as 'calo' while 'tgt' stands for 'target box'. 49
3.2 Left: Event distribution in the x_1–x_2 plane, from the SU 91 Psi data. Border lines for $y = 3$, 4 and $M = 1.5$, 5.5 GeV are indicated. Right: Event distribution in the $M_{\rm T}$–y plane, from the SU 91 Psi data. The insert shows the corresponding *mass* distribution. 52
3.3 Left: Target hodoscope pattern of a S-U collision in sub-target 16. Right: Distributions of the 'signal' (open squares) and 'opposite-sign' (closed circles) events versus the interaction sub-target, for the SU 91 Psi data set. 53
3.4 $E_{\rm T}$ distributions in the SU 91 Psi data set (left) before and after correcting for the vertex efficiency (right). 54

4.1 y and $p_{\rm T}$ 'signal' distributions measured for mass values between 2.7 and 3.5 GeV (black circles) compared to those obtained by Monte Carlo for J/ψ production (open squares). This figure corresponds to the SU 90 St data set. 56
4.2 Ratio $\sigma_{\rm Ca}/\sigma_{\rm D}$ of Drell–Yan cross–sections, from E 772 (closed circles) [Ald 90] compared to the DIS results of NMC (open circles) [Ama 91], as a function of x. [Figure taken from Arn 94] 58
4.3 Left: Differential mass acceptance for the Drell–Yan process in the SU 91 Phi (open squares) and SU 91 Psi (closed circles) setups. Right: Illustration of the smearing effect in the mass variable (using Drell–Yan dimuons in the SU 91 Phi setup). 59

4.4 Left: p_{T}, y and $\cos(\theta)$ acceptances, in the SU 91 Phi setup, for the J/ψ and ψ' resonances (top) and for the Drell–Yan and D$\bar{\mathrm{D}}$ processes (bottom). Right: Table of J/ψ acceptance (in %) in y and p_{T} cells, for the SU 91 Phi setup. 60
4.5 Ratios of differential acceptances, in the SU 91 Phi setup, for ψ'/ψ (top), ψ/DY (middle) and D$\bar{\mathrm{D}}$/DY (bottom). 60
4.6 Distributions in $\cos(\theta)$ for the Drell–Yan and charm processes. . . . 61
4.7 p_{T}, y and $\cos(\theta)$ distributions, as collected by the four S–U setups, for three types of events: 'J/ψ' (top), 'continuum' (middle) and 'like-sign' (bottom). 61
4.8 Ratio of p_{T}, y and $\cos(\theta)$ distributions, for the 'J/ψ' (top) and 'continuum' (bottom) mass ranges, between the SU 91 Psi and the SU 90 St data sets. The effect of the 80 cm of iron in cutting the low p_{T} and low mass muon pairs is clearly visible. 62
4.9 J/ψ and ψ' shapes, as simulated for the SU 91 Phi data set. 63
4.10 Shapes of the simulated (generated above and reconstructed below) Drell–Yan (left) and D$\bar{\mathrm{D}}$ (right) mass distributions, as they appear in the SU 91 Psi data set. 67
4.11 Drell–Yan (left) and D$\bar{\mathrm{D}}$ (right) mass distributions, as reconstructed in the p–A and S–U data sets (SU 91 Psi excepted). 67
4.12 Ratio between the Drell–Yan mass distributions simulated for the S–U and p–A data sets, at the generated (left) and reconstructed (right) levels. 68
4.13 Opposite-sign and background dimuon mass distributions from the pU 87 (left) and SU 90 St (right) data sets. The inserts display the corresponding ratio 'background over opposite-sign'. 68
4.14 Ratio 'background over opposite-sign' for p–W (left) and S–U (right) data sets: closed circles for pW 88 V and SU 90 St; open squares for pW 88 D and SU 91 Psi. 69
4.15 Fit of the like-sign mass spectra in the SU 91 Phi data set (all E_{T}). Each 40 channels map the mass region between 1.5 and 5.5 GeV. . 71
4.16 Same as previous figure but for the SU 91 Psi data set. 72

5.1 E_{T} distributions (corrected for ϵ_v) of the signal events with mass above 1.5 GeV, from the SU 90 (left) and SU 91 (right) data sets. . 78
5.2 Ratio between the signal mass distribution corrected for the vertex efficiency and the same mass distribution without any correction, for the SU 90 St (left) and SU 91 Psi (right) data sets. 83
5.3 Left: E_{T} distributions (from the SU 91 Psi data set) associated with signal events in 1.5–2.5 GeV (circles) and 3.0–5.5 GeV (squares) and with background events in 1.5–2.5 GeV (triangles). Right: their ratios, "J/ψ over continuum" (circles) and "background over signal" (squares). 84

5.4 Illustration of the (simultaneous) fitting method, in the p–W (left) and p–U (right) data. 87
5.5 Result of the (simultaneous) fit, in the p–W (left) and p–U (right) data. 87
5.6 Result of the (simultaneous) fit to the S–U data sets: SU 90 St (left top); SU 90 Al (left bottom); SU 91 Phi (right top); SU 91 Psi (right bottom). 88
5.7 Ratio $B\sigma^{\psi'}$ / $B\sigma^{\psi}$ in p–A collisions as a function of A (left) and as a function of the reaction energy (right). 90
5.8 Same as figure 5.6 but only using events with E_{T} above 75 GeV. . . 91
5.9 Ratios ψ'/ψ and ψ/DY in the 4 E_{T} bins of S–U. The p–A values are included merely as an illustration. 92
5.10 J/ψ cross-sections (times branching ratios into muons), per target nucleon and for $x_F > 0$, as a function of p_{lab}. 95
5.11 'Signal' dimuon mass distributions in p–W (left) and p–U (right) collisions, with the J/ψ, ψ' and Drell–Yan normalized from the HMR fit. 96
5.12 Charm cross-section value estimated (within some hypothesis, see text) from the NA38 p–W data, compared to the values already presented in figure 1.9 on page 22. 97
5.13 'Signal' dimuon mass distributions in the four S–U data sets, in the same order as in figure 5.6, wherefrom the normalization of the HMR processes is taken. 98
5.14 'Signal' dimuon mass distributions from the SU 91 Psi data set, in the 4 ΔE_{T} bins. The J/ψ, ψ' and Drell–Yan contributions are normalized from the corresponding HMR fit. 99
5.15 Ratio between the measured and the expected signal, as a function of E_{T}, for a constant (left) or variable (right) R^{Bg}. 100
5.16 Comparison between the measured values and the curves predicted by the 'QGP' and 'nuclear absorption' models. 101
5.17 Ratio background over signal versus $M_{\mu\mu}$, for sub-targets 1–3 (closed circles), 4–6 (open squares) and 7–10 (stars), in the SU 90 St (left) and SU 91 Psi (right) data sets. 104

Introduction

Following the predictions of Quark Gluon Plasma (QGP) formation in nucleus–nucleus collisions and of the signatures that would signal experimentally the existence of such a state of matter [QM 82, QM'83, QM'84], an 'exploratory' program was developed, using the SPS accelerator at CERN to acelerate ions of oxygen (in 1986) and sulphur (from 1987 onwards).

It is in this context that the NA38 experiment was designed [Bal 85], aiming at being particularly suited to search for the production of thermal dimuons, at those times extensively studied [McL 85, Hwa 85, Čer 86, Kaj 86].

Meanwhile, Matsui and Satz published their prediction that, in the presence of a QGP, the production of the J/ψ resonance would be suppressed in relation to the production of Drell–Yan dimuons [Mat 86]. Naturaly, NA38 was the better placed experiment to observe such effect. The analysis of the experimental data corresponding to this signal, relatively fast due to its simplicity, was presented in the QM'87 conference [Bus 87], getting famous the expression 'J/ψ suppression'.

The results presented by NA38 lead to intense discussions and, in the following years, many theory articles were published trying to explain them, either as a signal of QGP formation, as had been predicted [Bla 87, Kar 87, Chu 88], or on the basis of nuclear absorption mechanisms, an explanation put forward *a posteriori* [Fta 88, Gav 88, Vog 88, Bla 89].

This discussions strongly supported the continuity in operation of the NA38 experiment [Abr 88], with new data taking periods between 1990 and 1992, and has motivated a strong interest in the behaviour of the ψ'/ψ ratio, for which both kinds of models have different predictions [Gup 92].

Other signatures observable in the dimuon mass spectra were, meanwhile, proposed: thermal and hadronic charm production, $\pi^+ \pi^-$ annihilation in the pion gas, etc. These studies increased the interest in the analysis of the dimuon mass region between the ϕ and the J/ψ (the 'intermediate mass region' — IMR).

This analysis is particularly difficult in view of the large background due to the combinatorial decays of π and K mesons, in ion collisions. The analysis of the data collected in 1986 and 1987, with oxygen and sulphur beams, has revealed some problems in the subtraction of this background. Following this work, some changes were introduced in the experimental setup, giving hope that the data collected afterwards can be accurately analysed in what concerns this mass region, particularly sensitive ($M \sim 1.5$ GeV). Therefore, the present study is conducted essentially on these more recent data.

The analysis described in this thesis is original in relation to several topics. It is the first study of Drell–Yan production in nucleus–nucleus collisions. Absolute cross–sections for J/ψ and ψ' production are presented, in proton–nucleus and nucleus–nucleus collisions. In the case of the J/ψ, these new values are affected by smaller statistical and systematical uncertainties than the ones previously available. For the ψ', the values presented in this thesis are original. Naturaly, the ratio ψ'/ψ (ratio of cross–sections times branching ratios) is also derived, both in p–A and S–U collisions, its systematical uncertainties having been carefully studied. An almost original study of the nature of the IMR continuum, in what concerns its Drell–Yan and charm composition, is performed, both in the p–A and S–U data.

We have analysed several data sets, taken with different experimental setups, corresponding to 3 projectile–target combinations: p–W, p–U and S–U. The information on the 'signal' processes that contribute to the measured dimuon mass spectra is extracted by means of a *simultaneous* fit to all the data sets of a given B–A combination, a somewhat original procedure.

The statistical details of the data analysis procedure deserved always some special care. To prevent any problems from low statistics bins, we have always used the 'log likelihood' fitting method instead of using the, more usual, 'χ^2' method. All the fits were done on the *measured* (opposite-sign) dimuon spectra, of a truly poissonian nature, instead of using the 'signal' spectra, which involve the subtraction of the background contribution.

We have always worked with distributions on the 'measured' variables (sometimes called 'reconstructed') and not with spectra obtained from these by correcting the acceptance and smearing (finite resolution) effects of the dectector. The procedure we have adopted must be followed when, as is our case, processes with different kinematical distributions contribute to the same region of the dimuon mass spectra. In this situation, such corrections can only be applied if we know the fractions contributed by each process, which are only known *a posteriori* (as in the p–A spectra) or never (as in the S–U case) if there is an unknown process also contributing. An alternative procedure consists in making the acceptance correction event per event, using a multi-dimensional acceptance matrix, but this involves a much bigger (and unnecessary) complexity.

An early version of the data analysis and results obtained in this work was presented in the Quark Matter '93 conference [Lou 93]. More recent information was presented in other conferences [Lou 94a, Lou 94b and Lou 95].

This work is organized in the following way. It starts with an overview of QGP and dimuon physics (chapter 1), followed by a global description of the NA38 detector (chapter 2) and of the data reduction and normalization (chapter 3). After presenting the physical processes known to contribute to the dimuon mass spectra (chapter 4) we present the data analysis and its results for the high and intermediate mass regions (chapter 5).

References:

[Abr 88] M. Abreu *et al.* (NA38 Coll.), SPSC/88-24/P211/Add.2; SPSC/89-2/P211/Add.3.

[Bal 85] A. Baldit *et al.* (NA38 Coll.), SPSC/85-20/P211; SPSC/85-42/P211/Add.1.

[Bla 87] J.-P. Blaisot and J.-Y. Ollitrault, Phys. Lett. **B199** (1987) 499.

[Bla 89] J.-P. Blaisot and J.-Y. Ollitrault, Phys. Rev. **D39** (1989) 232.

[Bus 87] A. Bussière *et al.* (NA38 Coll.), Proc. of QM'87, Nordkirchen, Germany, 1987; Z. Phys. **C38** (1988) 117.

[Čer 86] V. Černý, P. Lichard and J. Pišút, Z. Phys. **C31** (1986) 163.

[Chu 88] M.-C. Chu and T. Matsui, Phys. Rev. **D37** (1988) 1851.

[Fta 88] J. Ftačnik, P. Lichard and J. Pišut, Phys. Lett. **B207** (1988) 194.

[Gav 88] S. Gavin, M. Gyulassy and A. Jackson, Phys. Lett. **B207** (1988) 257.

[Gup 92] S. Gupta and H. Satz, Phys. Lett. **B283** (1992) 439.

[Hwa 85] R. Hwa and K. Kajantie, Phys. Rev. **D32** (1985) 1109.

[Kaj 86] K. Kajantie, M. Kataja, *et al.*, Phys. Rev. **D34** (1986) 811. K. Kajantie, J. Kapusta, *et al.*, Phys. Rev. **D34** (1986) 2746.

[Kar 87] F. Karsch and R. Petronzio, Phys. Lett. **B193** (1987) 105. F. Karsch, M.T. Mehr and H. Satz, Z. Phys. **C37** (1988) 617. F. Karsch and R. Petronzio, Z. Phys. **C37** (1988) 627.

[Lou 93] C. Lourenço *et al.* (NA38 Coll.), Proc. of QM'93, Borlänge, Sweden, 1993; Nucl. Phys. **A566** (1994) 77c; LIP Preprint PHYS 94-03.

[Lou 94a] C. Lourenço, Proc. of the 'Workshop on Dilepton Production in Relativistic Heavy Ion Collisions', GSI, Darmstadt, Germany, 1994 (Ed. GSI), p. 178; LIP Preprint PHYS 94-01.

[Lou 94b] C. Lourenço, Proc. of the 'Fifth Conference on the Intersections of Particle and Nuclear Physics', St. Petersburg, Florida, USA, 1994; LIP Preprint PHYS 94-02.

[Lou 95] C. Lourenço, Proc. of the Hirschegg '95 Workshop, 'Hadrons in Nuclear Matter', Hirschegg, Austria, 1995 (Ed. GSI); LIP Preprint 95-03.

[Mat 86] T. Matsui and H. Satz, Phys. Lett. **B178** (1986) 416.

[McL 85] L. McLerran and T. Toimela, Phys. Rev. **D31** (1985) 545.

[QM'82] Proc. of QM'82, Bielefeld, Germany, 1982 (World Scientific, 1983).

[QM'83] Proc. of QM'83, BNL, USA, 1983; Nucl. Phys. **A418** 1984.

[QM'84] Proc. of QM'84, Helsinki, Finland, 1984; Lecture Notes in Physics, Vol. 221 (Springer-Verlag, 1985).

[Vog 88] R. Vogt, M. Prakash, *et al.*, Phys. Lett. **B207** (1988) 263.

Chapter 1

Review of previous knowledge

Besides the study of the general properties of hadronic matter, as produced by ultra-relativistic nucleus–nucleus collisions, the primary goal of the heavy ion experimental program (to which NA38 belongs) is to search for experimental evidence of the existence of the Quark–Gluon Plasma (QGP), a deconfined phase of quarks and gluons predicted by statistical QCD, the fundamental theory of strongly interacting matter. Therefore, it is mandatory to briefly review the signatures that might reveal the formation of this hypothetic state of matter, giving emphasis to those observable through the production of muon pairs, within the context of the NA38 experiment. Since the 'classical' mechanisms of dimuon production constitute the reference frame in NA38's search of any new phenomena, they also deserve some attention, both concerning the experimental observations and their theoretical understanding.

1.1 General overview of QGP physics

Some simple and intuitive arguments, based on the 'MIT bag model' [Cle 86], are confirmed by sophisticated Lattice-QCD numerical simulations [Kar 92], that require the intensive use of the most powerful supercomputers existing nowadays, in the prediction that quarks and gluons should become deconfined from the parent hadrons, when compression makes them overlap each other, reaching densities 3 to 5 times higher than those of ordinary nuclear matter (0.17 fm^{-3}), or when heating makes the temperature of such medium exceed some critical threshold. Figure 1.1 *a* is the usual pictorial representation of such a $\mu - T$ 'phase diagram' (μ being the baryon chemical potential, or the baryonic density).

At the *deconfinement temperature*, predicted to be $T_c \simeq 150 - 200$ MeV, the *energy density* of the medium jumps from the Hadron Gas (HG) value to the QGP value, following the change in the *number of degrees of freedom* between both phases. In order to illustrate this point, and get a feeling of the numbers involved, it is enough to consider a simplified scenario [Mül 85, Mül 92]. A massless and

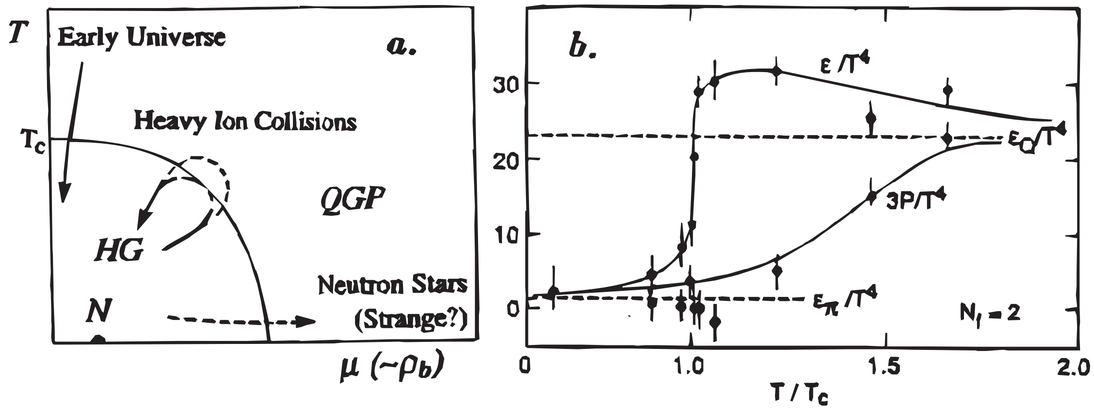

Figure 1.1: *a*) $\mu - T$ phase diagram, showing the HG and QGP regions. *b*) Energy density and pressure, in units of T^4, versus temperature, in units of T_c, through the phase transition region. [Figure taken from Son 93]

non-interacting hadron gas has basically the 3 pion degrees of freedom (π^+, π^-, π^0, neglecting the resonances), the Stefan-Boltzmann relation ($\epsilon = aT^4$) giving

$$\epsilon_{HG} = 3\ \epsilon_\pi = 3\frac{\pi^2}{30}T^4\ , \tag{1.1}$$

while a 2-flavour QGP, of massless (u and d) quarks and baryon-free (vanishing net baryonic number, $\rho_b \sim \mu = 0$), has 16 gluonic *d.o.f.* (2 spin states times $3^2 - 1$ SU(3) colour states) plus 12 (anti)quark *d.o.f.* (spin $\times$ colour $\times$ flavour), yielding an energy density of

$$\epsilon_{QGP} = 16\ \epsilon_g + 12\ (\epsilon_q + \epsilon_{\bar{q}}) = 16\frac{\pi^2}{30}T^4 + 12\frac{7}{4}\frac{\pi^2}{30}T^4 = 37\frac{\pi^2}{30}T^4. \tag{1.2}$$

Both these energy density values are included in figure 1.1 *b* as dashed horizontal lines, together with the more realistic Lattice QCD results [Got 87]. When the strange quark is included in the ideal gas of partons, the energy density increases to $(47.5\ \pi^2/30)\ T^4$.

In real life, however, such a naive 'ideal' scenario turns into something much more complicated. For instance, the order of the phase transition, computed in Lattice QCD, is not certain since it seems to depend on the starting assumptions. Even if there is no *mixed phase*, any real experiment (at least at the presently available energies) will always detect a majority of events *without* QGP formation and it is certainly not easy to separate them out from the 'interesting' ones.

The values quoted above refer to the *initial* energy densities, of the medium existing at the early stages of the QGP evolution, and must be translated into a *final* energy density definition, that can be applied to the detected secondary particles. Bjorken [Bjo 83] has introduced such a relation, currently widely used, that estimates the energy density achieved in the central region of the nucleus–nucleus collision through the particle multiplicity measured in the central rapidity unit, dN/dy, times their mean transverse mass, $\langle m_T \rangle$, divided by the effective interaction volume, $A_T \cdot \tau$,

$$\epsilon = \frac{\left.\frac{dN}{dy}\right|_{y=0} \cdot \langle m_T \rangle}{A_T \cdot \tau} \,. \tag{1.3}$$

In the case of NA38, this relation is calculated using the neutral transverse energy measured by the electromagnetic calorimeter, E_T^0, normalized to the rapidity window it covers, Δy, while the overlap area, A_T, is computed by a geometrical model that reproduces well the measured transverse energy distributions,

$$\epsilon = \frac{3 \cdot E_T^0}{\Delta y \cdot A_T \cdot \tau} \,. \tag{1.4}$$

In these expressions, τ is the spatial[1] extension of the interaction region, also interpreted as the *formation time of the partons* or the *thermalization time*, and is usually taken as 1 fm.

1.2 QGP signatures

Many different effects have been proposed, in the last decade, as possible ways to experimentally detect the formation of the QGP state of matter, from the 'old' mean p_T as a function of particle multiplicity ($T-\epsilon$ phase diagram *a la* JACEE[2]), to the recent ideas about using the (narrow) width of the ϕ peak in the $\mathrm{K}^+\mathrm{K}^-$ channel ($m_\phi \sim 2m_K$) to check for medium induced (chiral symmetry restoration) changes in the ϕ and/or K mesons [Lis 91]. Quite often, new developments in these ideas are reported in specialized reviews, workshops, schools and conferences [see, among many others, Kaj 87, BNL'88, GIF'88, QGPS'90, NASI'92, QM'93].

Nucleus–nucleus collisions are extremely complex phenomena, certainly not instantaneous, evolving in time from the pre-equilibrium phase to the post-hadronization phase. Actually, it is difficult to imagine how a violent collision of highly energetic nuclei leads to a phase of *thermal equilibrium*. Anyway, it is a challenge to find in the detected final state particles some information about the several stages of their (eventually formed) parent QGP system, long gone by then.

While some probes give a sort of 'surface' information, like the hadron's p_T distributions, the strangeness production and the interference effects, some others reveal deeper ('volume') aspects. Most of these harder processes (jets excluded)

[1] As is becoming common practice, we are using the natural system of units, in which $c = 1$.

[2] See, for example, the much debated plot presented by the JACEE collaboration in its contribution to the QM'84 conference [Bur 84].

are expected to be visible through a dimuon experiment: high mass Drell–Yan; $D\bar{D}$ pairs; charmonia (and bottonia) spectra; energetic dileptons and photons. All of these different clues have to be investigated (as a function of the associated particle multiplicity, or E_{T}) to get a good understanding of such a complex system, with the surface probes giving information on global characteristics (equation of state, collective flow, expansion dynamics, size and lifetime of the system) while the volume ones are better suited to address the features of the QGP it self.

In the following we will mention in some detail the signals that are relevant for the NA38 (dimuon) experiment.

1.3 Thermal production of dimuons and photons

Among the several signatures proposed to probe the nature of the matter formed in highly energetic nucleus–nucleus collisions, the electromagnetic signals, photons and dileptons, are particularly interesting. Indeed, once created, they travel through the nuclear matter around them without being influenced by processes involving strong interactions, like the hadronization, bringing to the detectors information on the initial stages of the reaction in which they are produced.

Since quite some years, theoretical studies have been done on the thermal production of dimuons, supposed to be emitted by the QGP as a result of the quark–antiquark annihilation in thermal equilibrium (actually, this was the main reason to justify the NA38 proposal). Yet, besides this process, which continues to raise a considerable interest [Ruu 91], recent developments show that also a hadron gas (HG) emits thermal dimuons, through pion annihilation: $\pi^+\pi^- \rightarrow \mu^+\mu^-$ [Kap 91]. For a given (QGP or HG) medium temperature, the dimuon (thermal) distributions are identical, not being possible to distinguish the mechanism that originated them. Although, once created, they are immune to further (strong) interactions, they don't tell us *when* they were created in the time evolution of the collision. Still, the observation of such a *thermometer* would allow a measurement of the temperature of the emitting source (whether it is a QGP or a HG).

One of the identifying signatures of the thermal dimuons (or photons) production, originated by quark or pion annihilation, is their quadratical dependence on the particle multiplicity, since it is a combinatorial process. So, if there are indeed thermal dimuons or photons, their production rate is expected to increase (quadratically) with the transverse energy released in the collisions[3].

[3] Up to present, a linear correlation between particle multiplicity and transverse energy has been observed by all ion experiments done at CERN.

1.4 Strangeness enhancement

Another effect considered to be a signal of QGP formation, also observable by the NA38 experiment but outside the scope of the present work, is the increase in strangeness production [Raf 82, Koc 86].

A possible way to study strangeness production in the context of NA38, consists in using the like-sign muon pairs, produced from the decay in flight of the π and K mesons, to estimate the (parents) ratio K/π [Per 91]. The enhancement of this ratio has been *directly* observed by the E802/AGS and HELIOS-2/CERN experiments, when comparing nucleus–nucleus collisions to proton–nucleus ones [see, for example, the review of Que 92] as has been predicted to occur if a QGP is formed. Yet, this is not a unique feature of QGP formation. In quite the same way as for the thermal dimuons signal, a hadronic gas of sufficiently high density also prefers to produce $s\bar{s}$ pairs rather than the lighter quark flavours, u and d, when the Fermi energy increases beyond the strange quark mass [Koc 90a]. Besides, such an increase is already visible at the AGS energies (15 GeV per incident nucleon; $\epsilon \sim 0.7 - 1$ GeV/fm^3), not considered to be high enough to form a QGP.

Also the dimuon mass distribution gives information on strangeness production, 'hidden' in this case, through the behaviour of the ϕ vector meson, a $s\bar{s}$ bound state. The increase of the ϕ production rate was first proposed to be a QGP signal by Shor [Sho 85]. While ϕ production in p–p collisions is suppressed by the OZI rule, if a QGP is formed a quite considerable amount of such mesons could be produced by coalescence of s and $\bar{s}$ quarks during the hadronization process. The ϕ production has been studied by NA38 [Fer 91], by comparing it to the production of the non-strange resonances ρ and ω. A quite similar data analysis has been done by the HELIOS-3 collaboration [Maz 93, Lon 94]. These experimental results are summarized in figure 1.2, where one can see that the ϕ production increases with the multiplicity faster than the ρ/ω resonances.

Although, such a behaviour has been predicted to signal QGP formation, the following two notes of caution advise a more conservative approach to the interpretation of these results. From the theory side, it has been argued [Koc 90b] that a high absorption cross section (~ 10 mb) of ϕ mesons by a pion cloud implies that ϕ production is enhanced by the meson–meson (rescattering) interactions in a dense hadronic gas. From the experimental side, the HELIOS-1 experiment has found hints [Vee 93], in p–Be collisions at 450 GeV, that the ϕ shows a quadratic multiplicity dependence in contrast to the ρ and ω mesons, that exhibit the expected linear dependence.

At BNL, the E859 experiment (E802 collaboration) studies the ϕ behaviour through its decay into K^+K^- pairs, which allows them to get results with a truly exceptional precision [Wan 93], considering the high multiplicity environment of the ion experiments: $m_\phi = 1020.4 \pm 0.4$ MeV and $\Gamma_\phi = 4.6 \pm 1.1$ MeV (in excellent agreement with the values of the PDG tables [PDG 94]: $m_\phi = 1019.413 \pm 0.008$ MeV and $\Gamma_\phi = 4.43 \pm 0.06$ MeV).

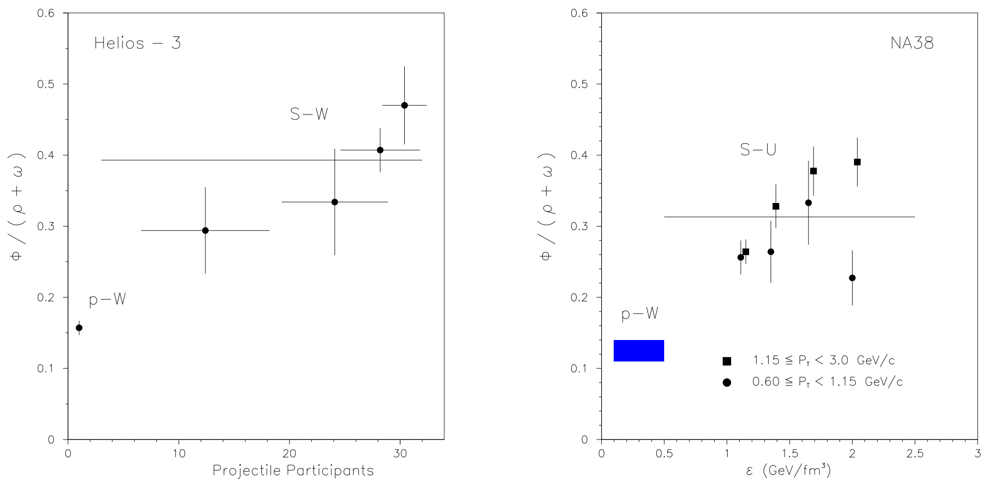

Figure 1.2: The ratio ϕ / $(\rho + \omega)$ as measured by the HELIOS-3 and NA38 experiments. The horizontal line represents 2.5 times the p–W value. [Figure taken from Lou 94b]

1.5 Charmonia suppression

Shortly after the NA38 proposal being approved, Matsui and Satz [Mat 86] gave it a new *raison d'être* by arguing that the J/ψ vector meson, clearly visible as a resonance in the dimuon mass distribution, would have its production strongly suppressed if a QGP forms in nuclear collisions. The argument is basicaly the following. The heavy $c\bar{c}$ (or $b\bar{b}$) pairs can only be produced in the hard interactions that might occur before the thermal equilibrium phase. In a deconfining medium, colour (Debye) screening prevents the quarks from binding to each other to form the 'quarkonia' states (J/ψ, ψ' ... , Υ, Υ', ...), as they would otherwise. Instead, they just 'fly apart' and when the plasma expands, cools off and hadronizes, these massive quarks will find a different (lighter[4]) partner to form open charm (or beauty) mesons. The faster $c\bar{c}$ pairs are expected to escape from the plasma region close enough so that they will still form a (high transverse momentum) J/ψ [Kar 87].

The NA38 collaboration showed that, indeed, the J/ψ is suppressed relative to the dimuon 'continuum', when going from low to high E_{T} values, or from proton to ion induced reactions [Bag 89]. Following the first presentation of these results [Bus 87], a large number of ideas were expressed concerning their interpretation. Presently, a few *hundred* publications refer the (by now famous) 'J/ψ suppression',

[4]Heavy quark (hard) production is a rare process and thermal production is (exponentially) suppressed relative to the lighter quarks, by $\sim \exp(-m_c/T_c) \sim 10^{-4}$.

as is illustrated in figure 1.3 (notice that the NA38 experiment was approved in 1985). It is clearly beyond the scope of this work to review them [see Sal 89, Bla 90 and Sat 92 for such surveys].

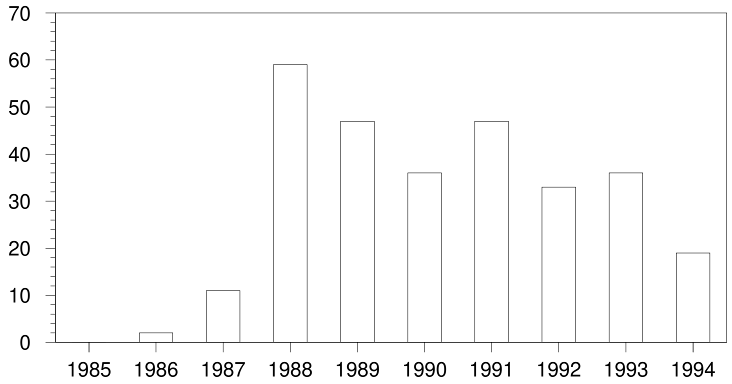

Figure 1.3: The evolution in time of the number of publications refering to the 'J/ψ suppression' topic. [Figure prepared with the help of David Dallman, from CERN's Library.]

Basically, the alternative (non-QGP) explanations deal with nuclear absorption effects: the J/ψ is destroyed by inelastic scattering with the mesons and baryons, basic constituents of the *confined* hot hadronic matter. In order to reproduce the experimental results, it is necessary to combine *initial state* nuclear scattering, of the quarks and gluons that will later give the $c\bar{c}$ pair, with *final state* absorption of the J/ψ in an *extremely dense* (but confined) hadronic matter, the dominant break-up reaction being

$$J/\psi + h \rightarrow D + \bar{D} + X \; . \tag{1.5}$$

Presently, both alternative scenarios reproduce the behaviour seen in the data, as a function of E_{T} and p_{T}, with essentially the same (good) agreement. Therefore, and in quite the same way as the previously referred 'QGP signatures', it is not yet clear what is the physical significance of the observed J/ψ suppression. Nevertheless, the very high densities required by the absorption models to explain the observations (around 4 hadrons/fm^3) raises an obvious conceptual question: how can a pion remain a pion when it overlaps a few others in the same volume?

A comparison of the J/ψ and ψ' production yields, is expected to provide some further inputs into this discussion, since the deconfinement and absorption mechanisms predict different suppression patterns for their ratio [Gup 92].

In the deconfinement scenario, the mixed origin of the observed J/ψ signal is responsible for the variation pattern of the ψ'/ψ ratio as the energy density, ϵ, changes. Indeed, as we will see in section 1.9, about 30 % of the observed J/ψ

events result from χ_c decays. The χ_c has a large radius, $r = 0.70$ fm [Kar 91], and so is expected to 'melt' close to the deconfinement (critical) temperature, T_c. The same happens to the ψ', $r = 0.88$ fm, but the smaller radius of the (directly produced) J/ψ, $r = 0.45$ fm, makes it more difficult to 'melt' by Debye screening, requiring higher temperatures (energy densities above $\sim 1.9\epsilon_c$). This is why the ratio (of 'survival probabilities') ψ'/ψ, normalized to the p–A value, is expected to evolve with ϵ according to

$$\frac{\psi'}{J/\psi} = \begin{cases} 1 & \text{if} \quad \epsilon < \epsilon_c \, , \\ 1 \ / \ [0.3 + 0.7\,(\epsilon/\epsilon_c)^{9/4}] & \text{if} \quad \epsilon_c < \epsilon < 1.9\,\epsilon_c \, , \\ 0.13 & \text{if} \quad 1.9\,\epsilon_c < \epsilon \, . \end{cases} \tag{1.6}$$

In the absorption scenario, the ratio of the ψ' and J/ψ 'survival probabilities' decreases exponentially as a function of the energy density. This is just the ratio of two exponentials with different 'slopes', since the absorption cross–sections of the ψ' and J/ψ are different.

The comparisons of these 'ideal curves' with the experimental data should be taken with some care. Nuclear geometry effects, for instance, will probably tend to smooth away part of the difference between both predictions.

Very recently, the cross section for the J/ψ–h inelastic reaction has been calculated in the formalism of short distance QCD [Kha 94]. The energy dependence of this cross section is shown to be essentially determined by the x-dependence of the gluon structure function (the low energy values of $\sigma_{\psi h}$ being set by the hard tail, as $x \to 1$). For low energy collisions, only hard gluons are able to break the tightly bound J/ψ state (of binding energy $\epsilon_\psi \sim 0.65$ GeV). In a hadronic medium, the mean momentum of the gluons confined inside a pion is estimated to be 20 % of the pion's momentum, of average 0.6 GeV if they have a thermal momentum distribution, $\exp(-p_\pi/T)$, and if $T = 0.2$ GeV. For matter in a deconfined state, the gluons are the thermally distributed constituents, with an average momentum five times higher than when inside the pions. Therefore, a large fraction of the guons will be hard enough to break the $c\bar{c}$ bound state, dissolving the J/ψ.

The authors (after cross-checking their results with charm photoproduction data) conclude that the hadronic matter produced in nuclear collisions, even at high densities, is not able to break up a significant amount of slow J/ψ mesons (the survival probabilities being above 95 %). On the contrary, the hard gluons found in deconfined matter can easily break a J/ψ into open charm mesons.

1.6 Open charm production

Open charm production is expected to become enhanced in a QGP if high enough initial temperatures (around 500 MeV) would be achieved [Sho 88]. Such (unrealistic) temperatures imply that this is not seriously considered as a useful signal to clearly identify the formation of a QGP. But it is important to keep it in mind as a potential background in the search for thermal dimuons as well as in the interpretation of the J/ψ suppression relative to the dimuon 'continuum'.

1.7 General overview of dilepton physics

The first measurements of muon pair production were carried on at the AGS (BNL) at the end of the 60's, and revealed an essentially continuous dimuon mass distribution going all the way up to the kinematical limit [Chr 70]. This exponentially falling continuum was soon interpreted by Drell and Yan [in their classical paper Dre 70] as the result of the decay of virtual photons, produced by the annihilation of (symmetrically charged) 'partons', point-like nucleon constituents that had been proposed by Feynman just some time before to explain the deep inelastic scattering (DIS) experimental data. Although a shoulder around $3-4$ GeV was already visible in these data, only in 1974 it was identified as the first particle of a new quark family, charm, whose dual name, J/ψ, reflects the 'excitement' that surrounded its discovery. The heavier $c\bar{c}$ and $b\bar{b}$ bound states were discovered shortly after.

The main feature of the dimuon mass spectrum is the exponentially decreasing continuum due to quark–antiquark annihilation,

$$q\bar{q} \rightarrow \gamma^* \rightarrow \mu^+\mu^- \ . \tag{1.7}$$

The electromagnetic decays of vector mesons (who share the photon quantum numbers, $J^P=1^-$), through a virtual photon,

$$V \rightarrow \gamma^* \rightarrow \mu^+\mu^- \ , \tag{1.8}$$

add to the global continuum a prominent structure of resonances. Therefore, it is quite natural to identify a 'high mass region' (HMR), characterized by the J/ψ and ψ' resonances superimposed on the Drell–Yan continuum, and a 'low mass region' (LMR), dominated by the low mass vector mesons (ρ, ω and ϕ) standing out of a very complex (but somewhat continuous) structure (see figure 1.4 a), involving, in particular, the Dalitz decays of the ω, η and η' [Vee 93]. Another major contribution comes from the uncorrelated decays of π and K mesons, a 'background' that extends into the intermediate mass region (IMR), where it adds to the Drell–Yan dimuons and to the muon pairs resulting from the simultaneous semi-leptonic decays of $D\bar{D}$ mesons.

Since in this work we report on the analysis of the intermediate and high mass regions (above 1.5 GeV), a more detailed reference to its contributing processes (J/ψ, ψ', Drell–Yan and 'charm') is required. The Υ family and the $B\bar{B}$ decays contribute with such a small cross section that they are beyond the sensitivity of the present NA38 experiment. The same is probably true for the (intermediate mass) vector mesons excited states: $\rho(1450)$, $\omega(1600)$, $\rho(1700)$.

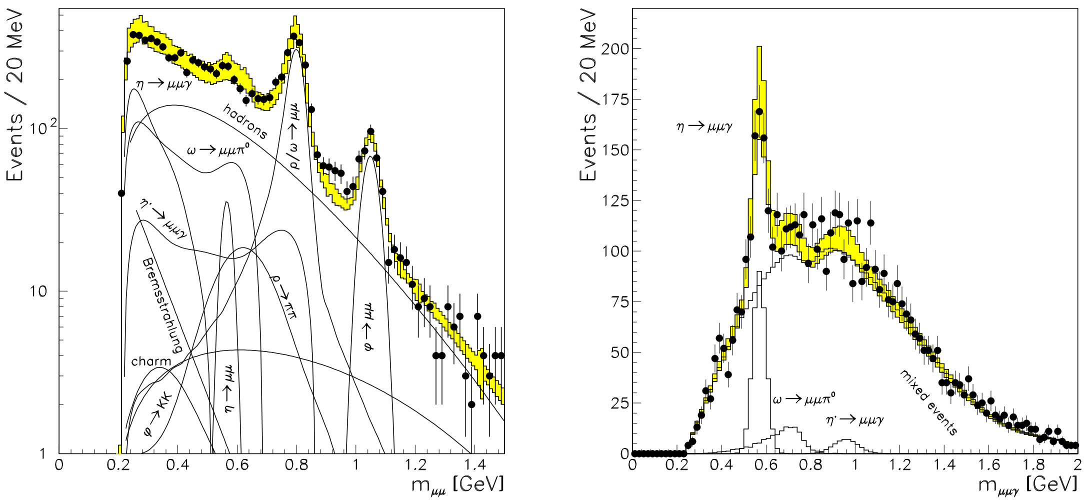

Figure 1.4: $M_{\mu\mu}$ and $M_{\mu\mu\gamma}$ distributions from p–Be collisions at 450 GeV, as measured by the HELIOS-1 experiment. The Dalitz decays dominate the signal up to $M_{\mu\mu} \sim 0.7$ GeV. [Figure taken from Vee 93]

A short review concerning the global features of the dilepton production in hadronic collisions, in the absence of collective phenomena, can be found in [Var 90], where special attention is given to the nuclear effects, in view of understanding the reference (non-QGP) results before studying the nucleus–nucleus collisions.

1.8 Drell-Yan process

The Drell–Yan process has been the subject of several extended review articles that cover both the experimental information and the theoretical developments required for their understanding [Cra 78, Mat 81, Str 81, Ber 82, Ken 82, Gro 86, Fre 90, You 92].

If a quark–antiquark pair share the same flavour, i, they can annihilate each other electromagnetically with the elementary cross section (given by QED and in analogy with $e^+e^- \to \mu^+\mu^-$)

$$\sigma_i(q_i\bar{q}_i \to \gamma^*) = \frac{4\pi\alpha^2}{3M^2} e_i^2 \; , \tag{1.9}$$

where e is the quark electric charge ($e_u = +2/3$, $e_d = -1/3$, ...) and M is the mass of the produced virtual photon, or the invariant mass of the lepton pair in which it decays. Convoluting this factor with the probability to find such a quark *and* such an antiquark in a given pair of colliding hadrons, A and B, given by the *parton distribution functions* and dependent on their fraction of the hadron's longitudinal momentum (x_1 for the projectile, x_2 for the target), we get the Drell–Yan differential cross section

$$\frac{d^2\sigma}{dx_1 dx_2} = \frac{1}{3} \cdot \frac{4\pi\alpha^2}{3M^2} \cdot \sum_i e_i^2 \left[f_i^A(x_1) \bar{f}_i^B(x_2) + \bar{f}_i^A(x_1) f_i^B(x_2) \right] , \tag{1.10}$$

where the factor 1/3 ensures that we only count annihilations of a quark with its corresponding (same colour) antiquark.

Perturbative QCD adds to this (Born) term the contributions from other subprocesses (involving gluons). The influence of the 'leading' (higher power) logarithm in each term of the perturbative series (the so-called Leading Log Approximation — LLA) is equivalent to introduce a scale dependence in the parton densities (explicitly calculated by the famous Altarelli–Parisi evolution equations), with the scale given by $Q^2 = M^2$,

$$\frac{d^2\sigma}{dx_1 dx_2} = \frac{1}{3} \cdot \frac{4\pi\alpha^2}{3M^2} \cdot \sum_i e_i^2 \left[f_i^A(x_1, M^2) \bar{f}_i^B(x_2, M^2) + \bar{f}_i^A(x_1, M^2) f_i^B(x_2, M^2) \right] . \tag{1.11}$$

The Drell–Yan cross sections calculated in this *leading order* (LO or LLA) formulation under-predict the experimentally measured values by $\sim 2 - 3$, the famous 'K factor'. The 'next-to-leading order' (NLO) QCD corrections, $O(\alpha_s)$, corresponding mainly to soft gluon contributions, are enough to get the theoretical predictions in much better agreement with the experiments [Sti 93][5].

In the present work, to be consistent with all the previous Drell–Yan experiments, we use the definition

$$K^{DY} = \frac{measured\ cross - section}{Leading\ Log.\ DY\ prediction} . \tag{1.12}$$

We have collected in table 1.1 (based on [Gro 86]) the K values found at energies similar to NA38's, since there are (experimental and theoretical) indications that the value of K decreases with increasing energy. The values reported here seem to cluster around 2.3, within a safety margin of the order of 20 %, which is the typical uncertainty in the incident flux normalizations. Bigger discrepancies are attributed to the use of quite different PDF's.

It is useful to introduce some well known kinematical relations between s (the hadron–hadron center of mass energy squared), the *scaling* variable τ, and the usual x_F and center-of-mass rapidity, y^*:

$$M^2 = (x_1 P_A + x_2 P_B)^2 \simeq x_1 x_2 s , \tag{1.13}$$

[5] See ref. 2 of [Sti 93] for the NLO corrections. A perturbative QCD analysis of the higher order diagrams, $O(\alpha_s^2)$, contributing to the Drell–Yan *mass* differential cross section has been performed recently. See ref. 3 of [Sti 93].

Experiment	Beam / Target	p_{Lab} (GeV)	K
NA 3 (1979)	$p : Pt$	200	2.2 ± 0.4
NA 3 (1980)	$(\bar{p} - p) : Pt$	150	2.3 ± 0.4
NA 3 (1980)	$\pi^- : Pt$	200	2.2 ± 0.3
NA 3 (1980)	$\pi^+ : Pt$	200	2.4 ± 0.4
NA 3 (1980)	$(\pi^- - \pi^+) : Pt$	200	2.4 ± 0.4
E 537 (1982)	$\bar{p} :\ Be,\ Cu,\ W$	125	2.25 ± 0.45
E 537 (1982)	$\pi^- :\ Be,\ Cu,\ W$	125	2.5 ± 0.5

Table 1.1: 'K factors' previously measured at energies similar to NA38's.

neglecting the quark's mass and transverse momentum;

$$\tau \equiv M^2/s = x_1 x_2 \ ; \qquad x_F \equiv 2\,p_L^*/\sqrt{s} = x_1 - x_2 \ ; \tag{1.14}$$

$$x_1 = \sqrt{\tau}\, e^{+y^*} \ ; \qquad x_2 = \sqrt{\tau}\, e^{-y^*} \ . \tag{1.15}$$

The p_{T} description of the lowest order Drell–Yan model (even including first-order perturbative QCD effects like gluon emission or absorption) is not good enough to account for the large measured mean p_{T} values, around 1 GeV (see figure 1.5). It is possible to generate more realistic p_{T} distributions by increasing the intrinsic (non-perturbative) transverse momentum of the partons inside the parent hadrons — the 'primordial' k_T.

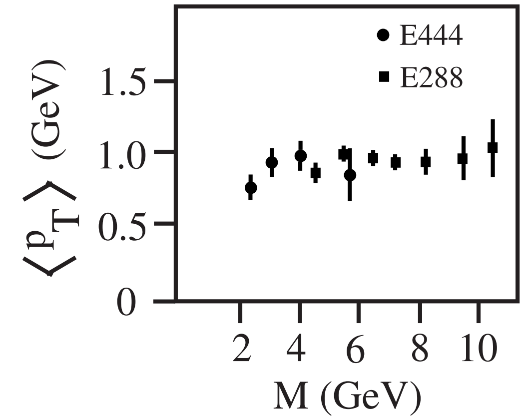

Figure 1.5: Mean p_{T} values for p–A and π–A dimuons, versus M. [Figure redone from Gro 86]

The angular distribution of the leptons in the (parent) virtual photon rest frame is predicted, in the basic Drell–Yan model of (spin-1/2) parton annihilation, to be

$1 + \cos^2(\theta)$, where θ is the (polar) angle between the direction of the (positively charged) lepton and the quark / antiquark ('beam') direction. In a (di)muon experiment, where hadron rejection requires the use of an absorber, it is difficult to accept the low energy muon required to get $\cos(\theta)$ near ± 1. Nevertheless, the existing information is *consistent* with this expectation. A different angular distribution arises [Ber 79] when one includes the effects of the 'higher twist' interactions. These are a kind of Drell–Yan interactions where the confinement forces inside the hadrons lead to the involvement of more than two quarks in the process. Such corrections are particularly visible in pion interactions, as the x of the antiquark approaches 1. The pertinent experimental data was obtained in successive Fermilab experiments [And 79 b, Pal 85, Con 89, Hei 91]. Anyway, the narrow acceptance window of NA38 makes it very little sensitive to any details in the angular distribution.

The higher twist effects are most prominent at 'low' masses and high x (above 0.7). In the NA38 acceptance window, x_1 is not higher than 0.2, therefore such effects should not be apparent (in any case, they were neglected in the present work). Besides, there is no reason why such effects would be different from proton to nucleus beams.

Drell–Yan is understood as a hard (parton level) process, not being affected by the surrounding nuclear matter in a hadron–nucleus collision. This implies a 'linear' A-dependence, usually quantified through the parameterization

$$\sigma(A) = \sigma_0 \, A^{\alpha} \, . \tag{1.16}$$

The α values experimentally measured are systematically consistent with unity. For instance, the E288 experiment [Ito 81] has reported the value $\alpha = 1.007 \pm 0.018 \pm 0.028$, slightly increasing with p_{T} (see figure 1.6).

The modifications (shadowing) induced by the nuclear environment in the quark distribution functions result in an indirect nuclear effect in Drell–Yan production (and in DIS). In the kinematic regime of the NA38 experiment, this is a small effect [Cas 93] and has been neglected in the present work. Changing the PDFs parameterization has a minor effect on the normalization and shape of the calculated Drell–Yan mass distribution.

The nuclear Fermi motion smears the nucleons' energy, affecting the energy of the collision where the dimuons are produced and, therefore, the Drell–Yan differential cross section. Since some collisions get more energy and others get less, most of the effect cancels out. This question was carefully investigated by the E288 collaboration. In their paper [Ito 81] they express the calculated Fermi momentum correction (at central rapidity) as

$$\left(\frac{d^2\sigma}{d\sqrt{\tau}dy} \right)_{corr} \Big/ \left(\frac{d^2\sigma}{d\sqrt{\tau}dy} \right)_{uncorr} = 0.901 + 0.827\sqrt{\tau} - 2.54\,\tau \, . \tag{1.17}$$

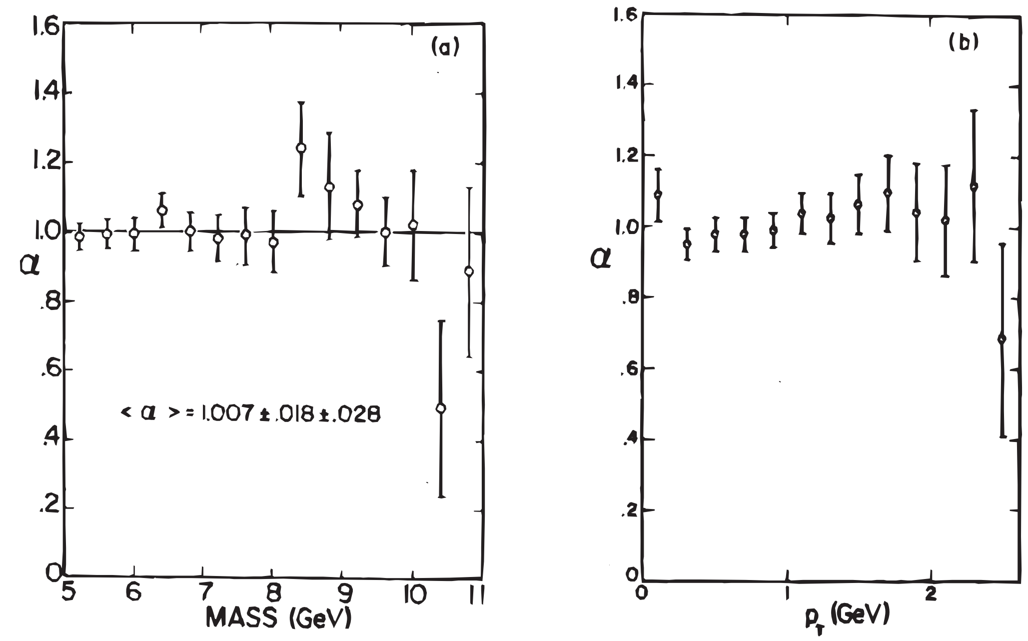

Figure 1.6: α as a function of M and of p_{T}, as measured by the E288 experiment. [Figures taken from Ito 81]

Applying this expression to NA38, we estimate the correction to be above 95 % (almost flat in the mass range we are interested in). The NA38 collaboration is presently investigating the influence of Fermi motion (both in the target and projectile nuclei) in the Drell-Yan contribution to the measured mass distribution. Some first (preliminary) results confirm that the shape of the mass distribution remains essentially unchanged. In the present work we have neglected any such (apparently small) effect.

Besides these nuclear effects, it is important to keep in mind that the Drell–Yan process is quite dependent on the (valence) quark composition of the interacting hadrons. For instance, while a nucleon–nucleon collision (no valence antiquarks available) must rely on the sea components to perform the $q\bar{q}$ annihilation, a meson projectile can annihilate its (valence) antiquark, producing (high mass[6]) dimuons much easily. This 'isospin dependence', expected in the simplest Drell–Yan model, has been quantitatively verified. The ratio between π^+ and π^- induced collisions (with roughly isoscalar nuclear targets) should be equal to the ratio of the valence antiquark electric charges squared, $e^2_{\bar{d}}/e^2_{\bar{u}} = (1/3)^2\,/\,(-2/3)^2 = 1/4$. The corresponding data ratio is shown in figure 1.7 *a*, while figure 1.7 *b* shows the (impressive) π^- over proton ratio. Clearly, a pion (even a positive one) has a larger

[6]To produce a high mass muon pair the x_1 and x_2 values must also be high (equation 1.13), where the valence quark distributions dominate.

cross section to produce a (high mass) dimuon than a proton. At low mass values, however, the sea parton distributions dominate and these isospin dependences disappear (see figure 4.12).

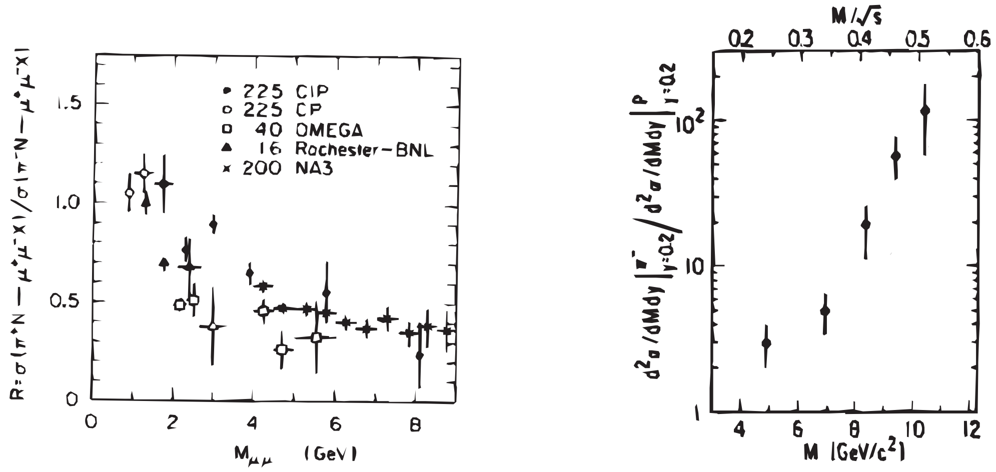

Figure 1.7: Ratio of the dimuon cross sections versus M. a) π^+ over π^-. b) π^- over proton. [Figures taken from Str 81]

A quite pertinent question concerns the lowest mass value where it is still possible to apply the Drell–Yan description. Although a (softer) 'Drell–Yan like' process clearly contributes to the IMR, its understanding is far less advanced than the massive lepton pair production, calculable by perturbative QCD methods[7]. In particular, it is not known whether the (high mass) K factor keeps its (essentially constant) value in the mass region below the J/ψ. Even the factorization, implicit in equation 1.11, between the hadronic structure functions and the elementary partonic cross section, might no longer be valid at low mass values.

It seems reasonable to expect, however, that any low mass deviations (such as the $K(M)$ 'factor', the 'higher twist' effects, etc) from the much better known high mass description, are the same in proton or nucleus induced collisions, leaving some hope in the search for nuclear specific dilepton sources, like thermal emission from dense (quark or hadronic) matter. The experimental information collected up to now concerning this mass region will be reviewed at the end of this chapter, after some words on another source of 'perturbation' in this same domain: heavy flavour production.

[7]At low mass values, $\alpha_s(M^2) \sim 1/\ln(M^2/\Lambda^2)$ is large and perturbative methods become unreliable.

1.9 Hadroproduction of J/ψ and ψ'

It is appropriate to refer in this section the J/ψ cross section measurements made by previous (p–A) experiments. The values reported in table 1.2 are *branching ratios* times cross section and refer to the positive x_F region of the phase space. The values 'per nucleon' are obtained from the measured ones using $\alpha^{J/\psi} = 0.92$.

Experiment	Target	p_{Lab} (GeV)	$B\sigma^{pA}$ (nb)	$B\sigma^{pN}$ (nb)
NA 3 (1983)	Pt	150	371 ± 65	2.90 ± 0.51
NA 3 (1983)	Pt	200	509 ± 93	3.98 ± 0.73
E 331 (1977)	C	225	82 ± 9	8.3 ± 0.9
E 444 (1979)	C	225	53 ± 7	5.4 ± 0.7
E 705 (1992)	Li	300	50.4 ± 5.5	8.4 ± 0.9

Table 1.2: Values of $B\sigma$ ($x_F > 0$) for J/ψ production, as a function of the energy of the incident protons. [Data taken from Bad 83, Bra 77, And 79a and Ant 92]

The most recent measurement of the J/$\psi\to\mu\mu$ branching ratio, reported by the Mark III collaboration [Cof 92], is $5.91 \pm 0.11 \pm 0.20$ %, leading to a new 'world mean value' of 5.97 ± 0.25 % [PDG 94]. The ψ' branching ratio into muons is still $7.7 \pm 1.7 \times 10^{-3}$.

To get the *direct* J/ψ production cross section it is not enough to consider the branching ratios into muon pairs. Indeed, a substantial fraction of the observed J/ψ events result from the radiative decays of the charmonium χ_c states ($\chi_c \to J/\psi + \gamma$) and from ψ' decays. The amount of measured J/ψ that result from the decay of higher charmed states is particularly important in the interpretation of the 'J/ψ suppression' observations. The E705 collaboration [Ant 93] identifies the χ_{c1} and χ_{c2} contributions combining the muon pairs with the non-π^0 photons and conclude that 30 ± 4 % of the J/ψ's produced in p–A interactions at 300 GeV are due to radiative χ_c decays. Furthermore, the ψ' is found to be responsible for 7.5 ± 1.7 % of the observed J/ψ events, a reasonable number in view of the high $\psi'\to$J/ψ+*anything* branching ratio, 57 ± 4 %. Neglecting other indirect sources, like B decays, the direct J/ψ production is found to contribute with only 62 ± 4 % of the measured J/ψ events. These results are in perfect agreement with the values previously found by the WA11 experiment [Lem 82].

The already published values of NA38, concerning J/ψ cross sections in proton and sulphur induced reactions [Bag 91], are not considered in this work as 'previous knowledge', being presented in chapter 5.

For later comparison with our own results, figure 1.8 *a* has a summary of the p–A values measured for the ratio ψ'/ψ (ratio of cross–sections times branching ratios) by other experiments [Sny 76, Cla 78, And 79 a and Ant 92]. Figure 1.8 *b* is a different way of seeing that, in p–A collisions, the J/ψ and ψ' vector mesons have the same behaviour, both having $\alpha = 0.92 \pm 0.01$. Even in $\pi^- - N$ collisions,

ψ'/ψ is found [Hei 91] to be slightly below 2 %, at moderate x_F, where gluon fusion dominates, steadily increasing as x_F approaches 1, because of the more important $q\bar{q}$ contribution (since the projectile has a valence antiquark).

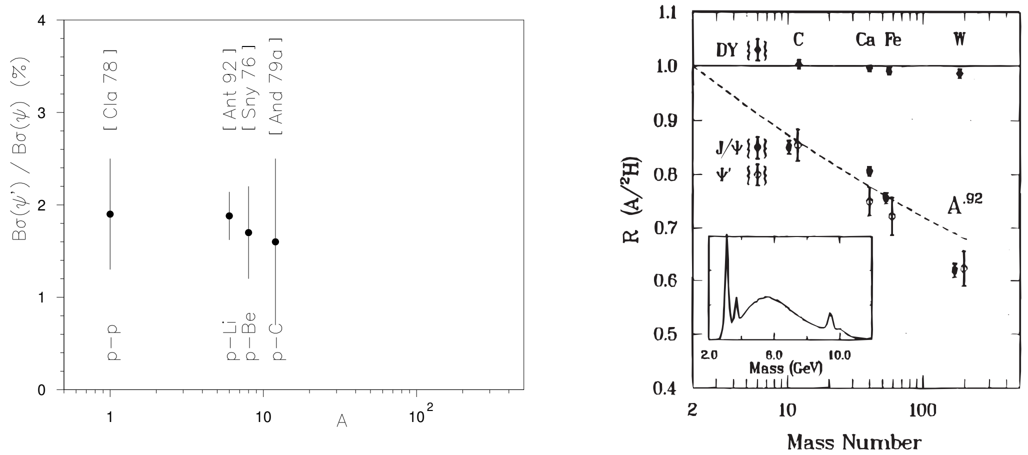

Figure 1.8: a) p–A values of ψ'/ψ, ratio of cross–sections times branching ratios, measured by several experiments. b) J/ψ and ψ' production reveal the same A-dependence in the E772 experiment [Ald 91].

1.10 Open charm hadroproduction

In this last decade, the field of charm production has become increasingly mature, with considerable improvements both on the experimental and on the theoretical side. An extensive and up-to-date review of this subject has been done by Appel [App 92].

The measurements of the NA27 and E743 experiments, at 400 GeV and 800 GeV, respectively, are still considered very good references in what concerns the absolute cross sections of charm production. Both experiments used the high resolution bubble chamber LEBC as 'vertex detector' and (liquid Hydrogen) target, followed by the 'downstream' (EHS or MPS) particle spectrometers. Studies of differential distributions and correlations have become possible in the most recent years, mainly through the high statistics data collected by several ('electronic' rather than 'visual') Fermilab experiments, where a reasonable charm selection is introduced already at the trigger level.

The NA27 and E743 experiments have measured the cross sections corresponding to the production of single charmed mesons (D^+, D^-, D^0 and $\bar{D}^0$). Adding these values gives the $D/\bar{D}$ inclusive cross sections: $\sigma(D/\bar{D})\ =\ 30.2 \pm 3.3\ \mu$b

[Agu 87], at 400 GeV, and $\sigma(D/\bar{D}) = 48^{+10}_{-8}$ μb [Amm 88], at 800 GeV. The $D\bar{D}$ *pair* cross sections are roughly a factor of two smaller. Taking into account an estimated limit on the extra contribution from the associated $\Lambda_c\bar{D}$ and $\bar{\Lambda}_c D$ production and using the Lund scheme of charm quark fragmentation, it is possible to go back to the parent level and infer the $c\bar{c}$ production cross sections [see ref. 1 of Ber 88]. The values obtained for $\sigma(pp \rightarrow c\bar{c}X)$ are 14 to 23 μb, at 400 GeV, and 29 to 55 μb, at 800 GeV.

These estimates of the absolute cross section for the production of a $c\bar{c}$ pair, in a proton–proton collision, are very important to verify the normalization of the theoretical calculations, and are showed in figure 1.9. The more recent values of NA32 [Bar 88] and E653 [Kod 91] have been added, as done in [App 92].

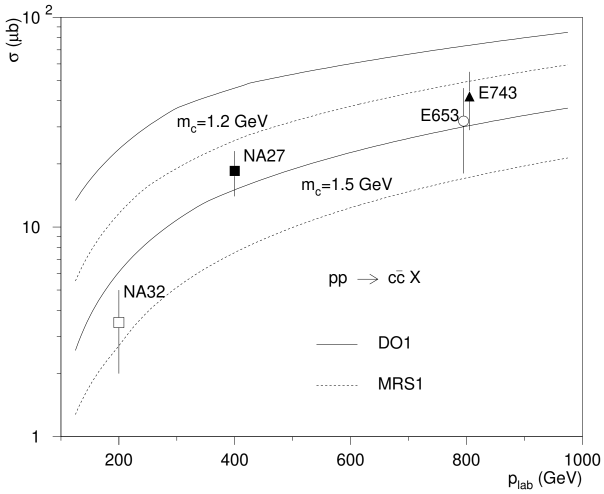

Figure 1.9: Charm production cross–sections, in nucleon–nucleon interactions, as a function of incident energy. [Figure inspired on Ber 88 with more data points]

The curves included in this figure are $pp \rightarrow c\bar{c}X$ cross sections, versus p_{lab} of the incident proton, from a next to leading order calculation (order α_s^3) [Nas 88], using two values for the charm quark mass and two different sets for parton densities. While the energy dependence of the cross section seems to be roughly independent of the other parameters, its absolute value changes considerably as a function of the c quark mass and is also quite dependent on the PDFs used in the calculations (see chapter 4). The c quark mass has not been measured with the desired precision, up to now. The most common value used lately in the literature is 1.5 GeV.

The charm pair production cross section in proton–nucleon interactions has also been measured by the NA25 experiment [Err 86] at 200 GeV, $3.9^{+2.5}_{-1.9}$ μb, and at 360 GeV, $24.6^{+12.}_{-8.3}$ μb. These values were determined from a sample of 8 events at 200 GeV and 15 events at 360 GeV, including an estimated background of 2 events in both cases. The Λ associated production is not considered in these numbers. Since a heavy (liquid) target was used, a linear A-dependence was assumed to get the quoted values.

The charm cross section is expected to increase linearly with the atomic mass weight, A. Indeed, similarly to what happens in the Drell–Yan process, the hard parton scattering required for heavy quark production is insensitive to the nucleus where the (target) parton exists. Furthermore, and in contrast to Drell–Yan production, the isospin effects can be neglected, since charm production is understood as being mainly ($\sim$ 80%) produced through gluon fusion, the (light) quark–antiquark annihilation playing only a minor role. The latest experimental information gives support to this expectation. The E769 collaboration has recently published [Alv 93] the value $\alpha = 1.00 \pm 0.05 \pm 0.02$ (see equation 1.16) for $D\bar{D}$ production by 250 GeV pions (illustrated in figure 1.10). The very small systematic uncertainty is due to sending the beam through all 4 target materials at the same time. The (even more recent) results from E789 [Lei 94], with a beam of 800 GeV protons, are also in perfect agreement with a linear A-dependence: $\alpha = 1.02 \pm 0.03 \pm 0.02$.

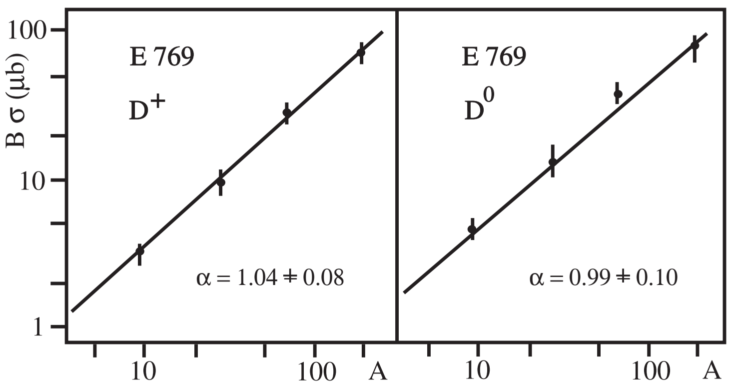

Figure 1.10: Cross section times branching ratio for D^+ and D^0 production as a function of A. [Figure redone from App 92]

1.11 Dimuons from charm decays

Already in 1980, the Omega collaboration [Cor 80] addressed the question of the eventual existence of non Drell–Yan contributions to dimuon production in the intermediate mass region, using hadron beams of 39.5 GeV. The K factors necessary to get the Drell–Yan predictions in agreement with the measurements were found to be 2.45 ± 0.42, 2.52 ± 0.49 and 2.22 ± 0.41, for the π^-, π^+ and $(\pi^- - \pi^+)$ data, respectively. Since all three values are quite similar and any hadronic effect would cancel out in the $(\pi^- - \pi^+)$ data, any such contribution must be small at these (low) energies.

At higher energies (200 GeV), the NA3 collaboration studied the mass region from 1.8 to 2.6 GeV, using π^+, π^- and proton beams [Bad 84]. Again, the measured difference between the π^- and the π^+ cross sections, compared to the Drell–Yan model predictions, lead to a K factor (clean of contaminations from hadronic sources) of 2.47 ± 0.5, in this mass region. Assuming that this value still holds in proton induced interactions (at least it is consistent with the measured higher mass values), it is possible to normalize the expected Drell–Yan contribution, finding that it only accounts for about half of the observed cross section. The contribution from the muonic decay of D mesons was identified as a natural explanation for the remaining events.

At 450 GeV, the HELIOS-1 collaboration (using a refurbished NA3 muon spectrometer) has been able to explain the mass region between 1.2 and 2.8 GeV produced in p–Be collisions, as a superposition of Drell–Yan and charm contributions [Aub 93]. Profitting from a sophisticated detector, put together to study the (*a posteriori* non-existing) 'anomalous' low mass dileptons, they were able to use a better strategy than the previous experiments to study this question. Indeed, having an almost complete calorimetric coverage (added to the experiment in view of the ion program version, HELIOS-2), the missing energy distribution of

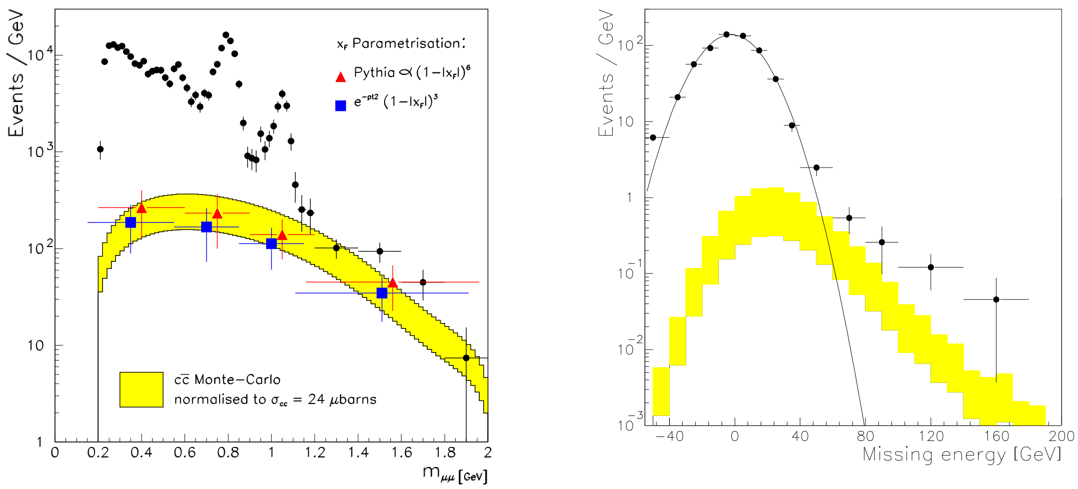

Figure 1.11: Dimuon mass and missing energy distributions measured by the HELIOS-1 experiment. The shaded area represents the charm contribution expected from a Monte Carlo based on PYTHIA, normalized to the EHS cross section measurement. [Figures taken from Aub 93]

the p–Be interactions allows a much clearer identification of the contribution from semi-leptonic decays of charmed mesons (see figure 1.11).

They have derived a value for the charm production cross section, relative to the ϕ, $\sigma_{c\bar{c}} = 24 \pm 8 \pm 16$ μb/nucleon. Unfortunately, the dimuon data does not extend beyond the J/ψ leaving the Drell–Yan contribution without a proper (high mass) normalization. The relative importance of the Drell–Yan and charm contributions to this mass region was reported in the form of their ratio:

$$DY/charm = 0.49^{+0.56}_{-0.40}(statistics)^{+0.30}_{-0.20}(systematics) \tag{1.18}$$

Although the uncertainties are large, it seems reasonable to say that, at 450 GeV and in this intermediate mass region, the charm contribution to dimuon production is more important than the Drell–Yan mechanism.

The HELIOS-3 collaboration is doing a study of the dimuon intermediate mass region in p–W and S–W collisions [Maz 93, Lon 94], in parallel with the analysis presented in this work. Also the CERES collaboration is doing a similar analysis, comparing the (low mass region) e^+e^- spectra obtained in collisions of (450 GeV) protons with Be and Au targets to those obtained in S–Au collisions [Dre 95]. These results are not considered in this work as 'previous knowledge'.

References:

[Agu 87] M. Aguilar-Benitez *et al.* (LEBC-EHS Coll.), Phys. Lett. **B189** (1987) 476; Z. Phys. **C40** (1988) 321.

[Ald 91] D.M. Alde *et al.* (E772 Coll.), Phys. Rev. Lett. **66** (1991) 133.

[Alv 93] G.A. Alves *et al.* (E769 Coll.), Phys. Rev. Lett. **70** (1993) 722.

[Amm 88] R. Ammar *et al.* (LEBC-EHS Coll.), Phys. Rev. Lett. **61** (1988) 2185.

[And 79a] K.J. Anderson *et al.* (E444 Coll.), Phys. Rev. Lett. **42** (1979) 944.

[And 79b] K.J. Anderson *et al.* (E444 Coll.), Phys. Rev. Lett. **43** (1979) 1219.

[Ant 92] L. Antoniazzi *et al.* (E705 Coll.), Phys. Rev. **D46** (1992) 4828.

[Ant 93] L. Antoniazzi *et al.* (E705 Coll.), Phys. Rev. Lett. **70** (1993) 383.

[App 92] J. Appel, Ann. Rev. Nucl. Part. Sci. **42** (1992) 367.

[Aub 93] P. Aubry, Université de Montreal Thesis, 1993.

[Bad 83] J. Badier *et al.* (NA3 Coll.), Z. Phys. **C20** (1983) 101.

[Bag 89] C. Baglin *et al.* (NA38 Coll.), Phys. Lett. **B220** (1989) 471; Phys. Lett. **B251** (1990) 465, 472; Phys. Lett. **B255** (1991) 459.

[Bag 91] C. Baglin *et al.* (NA38 Coll.), Phys. Lett. **B270** (1991) 105.

[Bar 88] S. Barlag *et al.* (NA32 Coll.), Z. Phys. **C39** (1988) 451.

[Ber 79] E.L. Berger and S.J. Brodsky, Phys. Rev. Lett. **42** (1979) 940.

[Ber 82] E.L. Berger, Proc. of the 'Drell–Yan Workshop', Fermilab, USA, 1982, p. 1.

[Ber 88] E.L. Berger, Proc. of the 'ARW on QCD Hard Hadronic Processes', St. Croix, Virgen Islands, 1987; Argonne Preprint ANL-HEP-CP-88-26; E.L. Berger, Proc. of the 'Workshop on Physics at Fermilab in the 1990s', Breckenridge, Colourado, USA, 1989.

[Bjo 83] J.D. Bjorken, Phys. Rev. **D27** (1983) 140.

[Bla 90] J.-P. Blaizot and J.-Y. Ollitrault, in R.C. Hwa (ed.), 'Quark Gluon Plasma' (World Scientific, 1990).

[BNL'88] Proc. of the 'Third workshop on experiments and detectors for a Relativistic Heavy Ion Collider (RHIC)', BNL, USA, 1988; (BNL 52185).

[Bra 77] J.G. Branson *et al.* (E331 Coll.), Phys. Rev. Lett. **38** (1977) 1331.

[Bur 84] T.H. Burnett *et al.* (JACEE Coll.), Proc. of QM'84, Helsinki, Finland, 1984; Lecture Notes in Physics, Vol. 221 (Springer-Verlag, 1985), p. 187.

[Bus 87] A. Bussière *et al.* (NA38 Coll.), Proc. of QM'87, Nordkirchen, Germany, 1987; Z. Phys. **C38** (1988) 117.

[Cas 93] P. Castorina, A. Donachie and P. Harriman, Z. Phys. **C60** (1993) 135.

[Chr 70] J.H. Christensen *et al.*, Phys. Rev. Lett. **25** (1970) 1523; Phys. Rev. **D8** (1973) 2016.

[Cla 78] A.G. Clark *et al.*, Nucl. Phys. **B142** (1978) 29.

[Cle 86] J. Cleymans *et al.*, Phys. Rep. **130** (1986) 217.

[Cof 92] D. Coffman *et al.*, (MARK III Coll.), Preprint SLAC-PUB-5592 (1992).

[Con 89] J.S. Conway *et al.*, Phys. Rev. **D39** (1989) 92.

[Cor 80] M. Corden *et al.*, Phys. Lett. **B96** (1980) 417.

[Cra 78] N.S. Craigie, Phys. Rep. **47** (1978) 1.

[Dre 70] S.D. Drell and T.M. Yan, Phys. Rev. Lett. **25** (1970) 316.

[Dre 95] A. Drees, Proc. of the Hirschegg '95 Workshop, 'Hadrons in Nuclear Matter', Hirschegg, Austria, 1995 (Ed. GSI).

[Err 86] O. Erriquez *et al.* (NA25 Coll.), Physica Scripta **33** (1986) 202.

[Fer 91] R. Ferreira *et al.* (NA38 Coll.), Proc. of QM'91, Gatlinburg, USA, 1991; Nucl. Phys. **A544** (1992) 497. R. Ferreira, Universidade Técnica de Lisboa Thesis, 1992.

[Fre 90] K. Freudenreich, Int. J. Mod. Phys. **A19** (1990) 3643. K. Freudenreich, Proc. of the 'International Workshop on QGP Signatures', Strasbourg, France, 1990 (Ed. Frontieres, 1991) p. 249.

[GIF'88] 'Ecole de Eté de Physique Nucleaire et de Physique des Particules', Lyon, 1988

[Got 87] S. Gottlieb *et al.*, Phys. Rev. **D35** (1987) 3972.

[Gro 86] C. Grosso-Pilcher and M.J. Shochet, Ann. Rev. Nucl. Part. Sci. **36** (1986) 1.

[Gup 92] S. Gupta and H. Satz, Phys. Lett. **B283** (1992) 439.

[Hei 91] J.G. Heinrich *et al.*, Phys. Rev. **D44** (1991) 1909.

[Ito 81] A.S. Ito *et al.* (E288 Coll.), Phys. Rev. **D23** (1981) 601.

[Kaj 87] K. Kajantie and L McLerran, Ann. Rev. Nucl. Part. Sci. **37** (1987) 293.

[Kap 91] J. Kapusta, P. Lichard and D. Seibert, Phys. Rev. **D44** (1991) 2774.

[Kar 87] F. Karsch and R. Petronzio, Phys. Lett. **B193** (1987) 105. F. Karsch and R. Petronzio, Z. Phys. **C37** (1988) 627. J.-P. Blaizot and J.-Y. Ollitrault, Phys. Lett. **B199** (1987) 199. M.-C. Chu and T. Matsui, Phys. Rev. **D37** (1988) 1851.

[Kar 91] F. Karsch and H. Satz, Z. Phys. **C51** (1991) 209.

[Kar 92] F. Karsch, Proc. of the 'NATO ASI Particle Production in Highly Excited Matter', Il Ciocco, Italy, 1992, NATO ASI Physics **303B** (1993) 207.

[Ken 82] I.R. Kenyon, Rep. Prog. Phys. **45** (1982) 1261.

[Kha 94] D. Kharzeev and H. Satz, "Quarkonium Interactions in Hadronic Matter", CERN Preprint TH.7274/94. H. Satz, Proc. of the 'NATO ARW Hot Hadronic Matter', Divonne, France, 1994, CERN Preprint TH.7410/94.

[Koc 86] P. Koch, B. Müller and J. Rafelski, Phys. Rep. 142 (1986) 167.

[Koc 90a] P. Koch and U. Heinz, Proc. of the 'International Workshop on QGP Signatures', Strasbourg, France, 1990 (Ed. Frontieres, 1991), p. 149.

[Koc 90b] P. Koch, U. Heinz and J. Pišút, Phys. Lett. **B243** (1990) 149.

[Kod 91] K. Kodama *et al.* (E653 Coll.), Phys. Lett. **B263** (1991) 263.

[Lei 94] M.J. Leitch *et al.* (E789 Coll.), Fermilab Preprint Pub-94/012-E.

[Lem 82] Y. Lemoigne *et al.* (WA11 Coll.), Phys. Lett. **B113** (1982) 509.

[Lis 91] D. Lissauer and E.V. Shuryak, Phys. Lett. **B253** (1991) 15.

[Lon 94] G. London, Proc. of the 'Workshop on Dilepton Production in Relativistic Heavy Ion Collisions', GSI, Darmstadt, Germany, 1994 (Ed. GSI), p. 130.

[Lou 94a] C. Lourenço, Proc. of the 'Workshop on Dilepton Production in Relativistic Heavy Ion Collisions', GSI, Darmstadt, Germany, 1994 (Ed. GSI), p. 178.

[Lou 94b] C. Lourenço, Proc. of the 'Fifth Conference on the Intersections of Particle and Nuclear Physics', St. Petersburg, Florida, USA, 1994; LIP Preprint PHYS 94-02.

[Mat 81] G. Matthiae, Riv. Nuovo Cimento **4** (1981) 1.

[Mat 86] T. Matsui and H. Satz, Phys. Lett. **B178** (1986) 416.

[Maz 93] M.A. Mazzoni *et al.* (HELIOS-3 Coll.), Proc. of QM'93, Borlänge, Sweden, 1993; Nucl. Phys. **A566** (1994) 95c.

[Mül 85] B. Müller, 'The Physics of the Quark-Gluon Plasma', Lecture Notes in Physics, Vol. 225 (Springer-Verlag, 1985)

[NASI'92] Proc. of the 'NATO ASI Particle Production in Highly Excited Matter', Il Ciocco, Italy, 1992, NATO ASI Physics **303B** (1993)

[Nas 88] P. Nason, S. Dawson and R.K. Ellis, Nucl. Phys. **B303** (1988) 607; Nucl. Phys. **B327** (1989) 49.

[Pal 85] S. Palestini *et al.* (E615 Coll.), Phys. Rev. Lett. **55** (1985) 2649.

[PDG 94] Particle Data Group, Phys. Rev. **D50** (1994) 1173.

[Per 91] L. Peralta, Universidade de Lisboa Thesis, 1991 M.C. Abreu *et al.* (NA38 Coll.), Z. Phys. **C55** (1992) 365.

[QGPS'90] Proc. of the 'International Workshop on QGP Signatures', Strasbourg, France, 1990 (Ed. Frontieres, 1991)

[QM'93] Proc. of QM'93, Borlänge, Sweden, 1993; Nucl. Phys. **A566** 1994

[Que 92] E. Quercigh, Proc. of the 'NATO ASI Particle Production in Highly Excited Matter', Il Ciocco, Italy, 1992, NATO ASI Physics **303B** (1993) 499.

[Raf 82] J. Rafelski *et al.*, Phys. Rev. Lett. **48** (1982) 1066.

[Ruu 91] P.V. Ruuskanen, Proc. of QM'91, Gatlinburg, USA, 1991; Nucl. Phys. **A544** (1992) 169. P.V. Ruuskanen, Proc. of the 'NATO ASI Particle Production in Highly Excited Matter', Il Ciocco, Italy, 1992, NATO ASI Physics **303B** (1993) 593.

[Sal 89] R.A. Salmeron, Proc. of the '24th Rencontres de Moriond', Les Arcs, France, 1989.

[Sat 92] H. Satz, Proc. of the 'NATO ASI Particle Production in Highly Excited Matter', Il Ciocco, Italy, 1992, NATO ASI Physics **303B** (1993) 615.

[Sho 85] A. Shor, Phys. Rev. Lett. **54** (1985) 1122.

[Sho 88] A. Shor, Phys. Lett. **B215** (1988) 375; Phys. Lett. **B233** (1989) 231. A. Shor, Proc. of the 'International Workshop on QGP Signatures', Strasbourg, France, 1990 (Ed. Frontieres, 1991) p. 235.

[Sny 76] H.D. Snyder *et al.* (E288 Coll.), Phys. Rev. Lett. **36** (1976) 1415.

[Son 93] P. Sonderegger, Proc. of the 'Particles and Nuclei International Conference (PANIC) XIII', Perugia, Italy, 1993 (World Scientific, 1994) p. 146; CERN Preprint PPE/94-21.

[Sti 93] W.J. Stirling and M.R. Whalley, J. Phys. G: Nucl. Part. Phys. **19** (1993) D1.

[Str 81] R. Stroynowski, Phys. Rep. **71** (1981) 1.

[Var 90] J. Varela, Proc. of QM'90, Menton, France, 1990; Nucl. Phys. **A525** (1991) 275c.

[Vee 93] R.J. Veenhof, Universiteit van Amsterdam Thesis, 1993. T. Åkesson *et al.* (HELIOS-1 Coll.), CERN Preprint PPE/94-140; to appear in Z. Phys. **C**.

[Wan 93] Y. Wang *et al.*, (E802 Coll.), Proc. of QM'93, Borlänge, Sweden, 1993; Nucl. Phys. **A566** (1994) 379c. Y. Wang *et al.*, (E802 Coll.), Proc. of 'HIPAGS '93: Heavy Ion Physics at the AGS', 1994, (G. Stephans, S. Steadman and W. Kehoe, ed.s); MITLNS Report 2158.

[You 92] G.R. Young, Proc. of the 'NATO ASI Particle Production in Highly Excited Matter', Il Ciocco, Italy, 1992, NATO ASI Physics **303B** (1993) 555.

Chapter 2

The NA38 experiment

The NA38 detector was situated in the CERN SPS North Area High Intensity Facility (NAHIF), where it replaced the previous NA10 dimuon experiment, keeping its muon spectrometer. An overview of the apparatus is shown in figure 2.1.

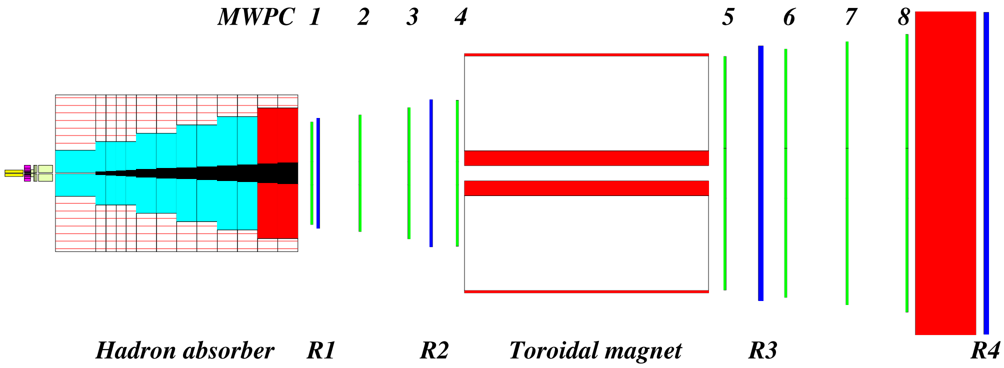

Figure 2.1: Overview of the NA38 detector: target region, muon filter, chambers (MWPC), hodoscopes (R), magnet, iron wall.

The muon spectrometer, its major component, measures the vector momenta of the muons produced in the target, from which the kinematical quantities defining the muon pairs are deduced. Of major relevance are the dimuon mass (M), rapidity (y) and transverse mass (M_{T}) or momentum (p_{T}), where $y = \ln(\,(E + p_{\mathrm{L}})\,/\,M_{\mathrm{T}}\,)$ and $M_{\mathrm{T}}^2 = M^2 + p_{\mathrm{T}}^2$.

The dimuon characteristics were correlated with the geometry of the nucleus–nucleus collisions, on an event by event basis, via the measurement of the released transverse energy, E_{T}, performed by an electromagnetic calorimeter placed after the target box.

2.1 Design strategy

The NA38 experiment was built to measure the characteristics of the muon pairs produced in relativistic ion collisions, but data with proton beams were also taken for reference purposes. The muon spectrometer was set to measure the dimuon events with mass bigger than ~ 0.5 GeV (just below the ρ).

To cope with the rather small cross section for the production of dimuons, the experiment worked with an intense beam (around 5×10^7 ions per burst), a multiple target with 20 % of an interaction length and close to mid rapidity, where the cross section is highest ($0 < y^* < 1$, where y^* is the rapidity in the center of mass frame).

The toroidal magnet was chosen (by NA10) in order to allow a sharp *mass* cut, at the trigger level. Indeed, in this kind of field, the deflection angle is inversely proportional to the *transverse* momentum. Since the dimuon mass, in the acceptance window of the spectrometer, is roughly equal to the sum of both p_{T} values, $M \approx p_{\mathrm{T1}} + p_{\mathrm{T2}}$, measuring the displacement angles gives a reasonable (and fast) estimation of the mass. This way, the NA10 experiment was able to study the mass region above the J/ψ (and even above the Υ), running with a very intense beam (up to $\sim 10^{10}$ pions per burst), without getting the data acquisition system filled with the much more abundant low mass events.

To clearly identify the resonances (to separate the ϕ from the ρ/ω and the ψ' from the J/ψ), it is essential to have a good mass resolution. On the other hand, muons are copiously produced by the decay of pions and kaons, particularly in the (high multiplicity) ion collisions, spoiling the signal to background ratio. Therefore, it is of capital importance to absorb these mesons *before* they decay. This is achieved by placing an absorber between the target and the muon spectrometer, long enough ($\gtrsim 10\ \lambda_I$) to contain all the hadronic shower. The highly penetrating muons are not stopped by these absorbers (except the low energy ones) but they suffer multiple (Coulomb) scattering and energy loss, resulting in a degradation of the mass resolution. Clearly, a compromise solution must be found, between maximizing the absorption probability of π (and K) mesons and minimizing the multiple scattering of the muons.

The design and material composition of the hadron absorber configuration was changed some times in the lifetime of the experiment, using the gained experience to further optimize (within budget constraints) the following data taking periods and providing some specific improvements to better achieve some physics goals. Basically, two (ion) setup configurations were developed, each of them particularly well suited to study the low ('ϕ') or the high ('J/ψ') mass regions.

It is quite important to start absorbing the hadrons immediately after the target, before they decay. In practice, this is not as easy as it sounds, since the experiment works with a multiple sub-target system rather than one single (long) target, having the space between the sub-targets 'filled' with air (a very poor absorber, indeed). Why is this so? Although one single long target would have the same fraction of interaction length than 10 thin sub-targets, it could happen that an incident ion would produce a peripheral collision at the beginning of the target, leaving a spectator fragment go through and produce a second interaction (indistinguishable from the first). Events with such reinteractions would produce the same E_{T} as a central collision while, in fact, the muon pair would be produced in a 'sub-collision'. This would spoil any correlation between the dimuon's variables and the 'centrality', estimated through E_{T}. For instance, it could actually be a 'carbon–uranium dimuon' instead of the assumed 'sulphur–uranium' one. With the multiple sub-target system such (spectator induced) events still occur but they can be identified and tagged as such, being rejected from the final analysis data sample. The space between the sub-targets and their transversal dimensions were optimized so that the number of secondary particle interactions is minimized.

Such a fractioned target requires the existence of a 'detector' system to identify the sub-target(s) where an interaction (or reinteraction) took place. This was provided by a hodoscope of 32 ring scintillators. It is very useful to improve the mass resolution (by constraining the muon tracks, affected by multiple scattering in the hadron absorber, to go through the interaction vertex), to correct the *transverse* energy measured by the calorimeter in a (sub-target dependent) rapidity window, to check the subtraction of the (also sub-target dependent) meson decay background, etc.

The high intensity of the beam also leads to some constraints in the detector design criteria. In particular, the radiation hardness of the beam counters placed up and downstream of the target system (where the beam is focussed, therefore most 'dense') had to be seriously taken into account, leading to the choice of *quartz* Čerenkov detectors. Also, at such high intensities, it happens quite often that *two* beam particles arrive together within the reading time gate of the calorimeter's ADCs, Δt =20 ns. The probability to have n incoming particles, distributed in time according to a Poisson distribution, arriving within the time interval Δt, is given by the expression[1]

$$P(n, \Delta t) = \frac{\mathrm{e}^{-\rho\Delta t}\,(\rho\Delta t)^n}{n!\,(1-\mathrm{e}^{-\rho\Delta t})}\,, \tag{2.1}$$

where ρ is the effective number of incident ions per second. For example, a beam intensity of 5×10^7 ions per burst, with a 3.3 s effective spill, leads in 14 % of the cases to an event with more than one incident ion within the reading gate,

$$1 - P(1, \Delta t) = 1 - \frac{\mathrm{e}^{-\rho\Delta t}\,(\rho\Delta t)}{(1-\mathrm{e}^{-\rho\Delta t})} \quad , \quad \text{with} \quad \rho\Delta t = 0.3\,. \tag{2.2}$$

Such events must be identified and tagged for eventual rejection (in the off-line analysis), otherwise they would bias the E_{T} measurement.

[1]This expression differs from the Poisson since Δt is started by a trigger (induced by an incident ion) rather than placed at random in the beam flux.

The transverse energy released in each collision, measured by the compact electromagnetic calorimeter, provides information on some global event characteristics, such as the particle multiplicity, the centrality of the collision, the number of participant nucleons, the energy density reached, etc. The (ion) events were tagged according to their E_{T} value, from peripheral to central collisions, in the hope of finding some *QGP like* behaviour in the 'high E_{T}' sample, as opposed to the p–A *like* behaviour of the 'low E_{T}' bin.

2.2 Apparatus overview

The NA38 apparatus was mainly composed of a dimuon spectrometer, an electromagnetic calorimeter, an active target and some beam counters.

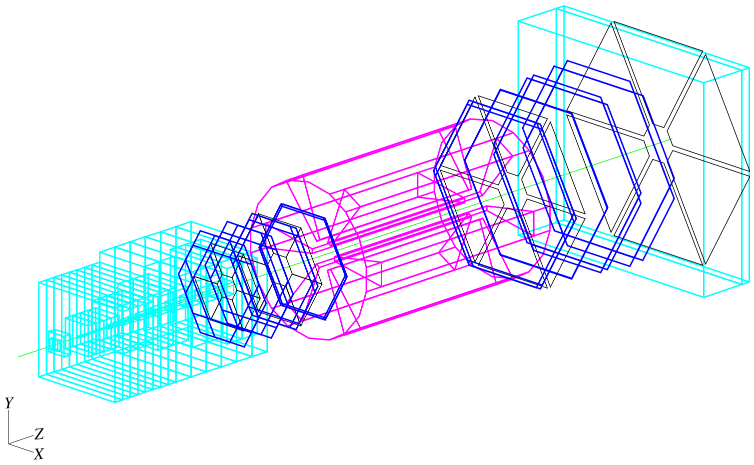

Figure 2.2: Layout of the muon spectrometer.

The muon spectrometer (see figure 2.2) was inherited from the NA10 experiment [And 84] having received some minor improvements. It consisted of a hadron absorber, an air-core toroidal magnet of hexagonal symmetry, 8 multiwire proportional chambers (MWPCs) and 4 hodoscopes of plastic scintillator slabs (of 2 ns time resolution) used to create the trigger.

It has a (RMS) mass resolution of 4 % in the ψ' region ($\sim$ 140 MeV). The acceptance started being meaningful around 0.5 GeV growing up to $\sim$ 20 % (for dimuons from the decay of J/ψ mesons, in the $|\cos(\theta)| < 0.5$ phase space window). Since the beam dump used to stop the non-interacting beam was located far away from the target, and given the good vertex resolution, there was no ambiguity concerning the origin of the muon tracks.

2.3 Detailed description

Below we give a brief description of some experimental features, stressing some points of particular importance for the studies presented in this work.

2.3.1 Beam

The experiment was located in the ('underground') ECN3 hall, at the end of a high-intensity beam line (see figure 2.3). We have both worked with primary and secondary beams. The primary (directly extracted from the SPS) protons had a momentum of 450 GeV while the (also primary) heavier projectiles, of $Z/A = 1/2$, like deuterons, oxygen and sulphur ions, had a momentum of 200 GeV per nucleon (or 400 GeV per charged particle). The beam momentum was gaussian distributed with a relative (RMS) resolution of $\sigma_p/p \sim 1 \times 10^{-3}$.

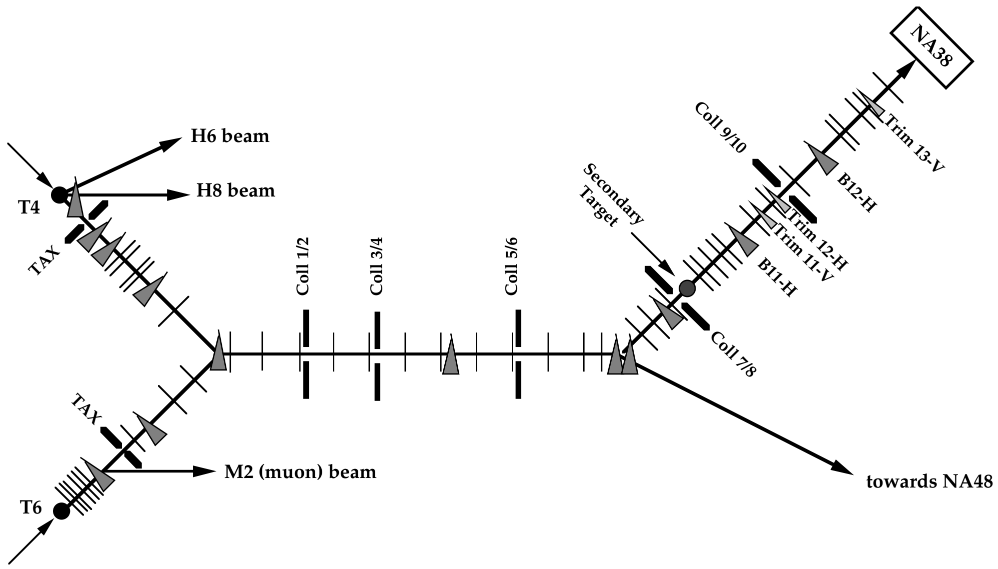

Figure 2.3: Schematic view of the NA38 beam line. [Courtesy of L. Gatignon]

We have also worked with 200 GeV protons, to have 'reference' data at the same energy per incident nucleon (or $\sqrt{s}$ in the nucleon–nucleon rest frame) as the ion data. This *secondary* proton beam was produced in a 'production' beryllium target (either T4 or T6, in figure 2.3), located around 1050 meters upstream of the NA38 target. Its relative (RMS) momentum resolution was of the order of $\sigma_p/p \sim 3 \times 10^{-3}$ (depending on the opening of the collimator 'Coll 1'). Naturally, such a beam is contaminated by positive pions. By extrapolation from measurements on particle production by 400 GeV protons interacting in beryllium targets, a pion contents of 31.5 % is estimated in the 200 GeV *proton* beam [Gat 93]. Roughly speaking, the 200 GeV beam contains about 2/3 of protons and 1/3 of π^+. To identify and tag the pions in the beam, we have used the information provided by 2 Čerenkov gas counters[2] (10 and 20 meters long) located between ~ 50 and ~ 100 m upstream of our target. Their helium pressure was set to 0.27 bar, so that only the pions gave a signal in these threshold counters (the protons have the same momentum but higher mass, therefore lower β). Besides allowing the rejection of the polluting pions on a event per event basis, the information provided by these detectors, integrated along the burst time (therefore not trigger biased), is of crucial importance in the (proton) luminosity counting. Being somewhat slow, these detectors (later removed from the beam line) have limited the maximum beam intensity used in the (200 GeV) proton runs. Still, the beam intensities were quite high, the incident rate on T4 or T6 being typically at the few 10^{12} level.

The beam to NA38 was derived either through T4 or T6, depending on the requirements of the neighbouring experiments. The 'secondary target' marked in figure 2.3, located some 200 meters upstream of the NA38 target, was used to provide electron beams, essential for the (*in loco*) calibration of the electromagnetic calorimeter.

The horizontal and vertical beam profiles were continuously monitored by a small proportional wire chamber, located ~ 70 cm upstream of the target center and containing two perpendicular sets of 0.5 mm inter-spaced wires. Typical (RMS) values for the beam spot size were[3] $\sigma_x \sim 0.3$ mm and $\sigma_y \sim 0.6$ mm.

The fraction of the beam that did *not* interact in the target was stopped in a 4 meter long tungsten and uranium 'beam dump', plugged in the hadron absorber but starting only 1.65 m downstream from the target, to prevent any ambiguity (already at the trigger level) concerning the origin of the muon tracks (the vertex resolution was roughly $\sigma_Z \simeq 40/M$ cm$\cdot$GeV).

The beam counting, essential for the absolute cross section measurements, was provided (both trigger and burst gated) by the 'beam hodoscope' (BH), composed of 2 scintillator planes, whose dimensions were: 20 mm in x, 62 mm in y and 1 mm thick. The scintillator slabs (2×8 in one plane and 2×7 in the other) had different transversal dimensions according to their distance to the center of the beam, so that each slab would see approximately the same fraction of the incident beam. This detector was placed 33 m upstream of the target where the (out of focus) beam spot was large enough (roughly 4 mm of RMS) to allow the incoming ions to be individually counted (and the radiation yield was low enough to allow *plastic* scintillators). The BH could be moved (by remote control) in the plane transverse to the beam, to enable its correct centering so as to intercept the whole beam section. If a second beam particle was counted by the BH within its 20 ns gate the event was flagged as a 'pile-up' event.

[2] Having two such detectors allows some redundancy and checking of their inefficiencies.

[3] As usual, we use a right-handed coordinate system with z along the beam direction and y pointing vertically upwards (see figure 2.2).

The BH efficiency for ion beams was quite high (around 99 %) but for proton beams it was considerably lower (between 80 and 90 %), specially when very high intensity proton beams were used. To deal with this problem there was a second 'beam counting' detector, a multi-foil ionization chamber filled with argon (loaned to the experiment by the BI group, SL Division, and known within the collaboration as 'the argonium'). It gave a signal proportional to the incident flux integrated during the burst time, with an absolute calibration provided, at low intensity, by the BH. Its linearity was verified (by the carbon activation method, for instance) up to very high intensities ($\sim 10^{11}$ protons per second). Having two independent detectors also allowed the continuous monitoring of each other, a very useful way of verifying their proper behaviour.

2.3.2 Target region

The target systems used in the p–U and S–U runs were composed of several sub-targets, surrounded by an hodoscope of (~ 30) tiny cylindrical scintillators, coaxial with and surrounding the targets (see figure 2.4). Such an 'active' target was able to identify (in the off-line processing) the sub-target where the interaction took place and tag, for rejection purposes, events with a reinteraction in a subsequent sub-target. The number, dimensions and positions (along the beam axis) of the sub-targets were different from the p–U to the S–U runs and also among the several sulphur data taking periods. The efficiency of the interaction sub-target recognition depends on the number of charged particles released in the collisions (and therefore on E_{T}).

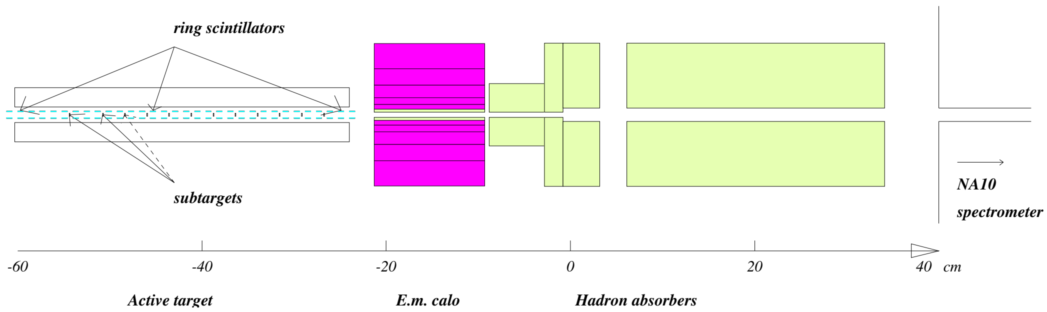

Figure 2.4: Overview of the target region. The center of the NA38 target is placed 45 cm upstream from the location of the NA10 target position ($z = 0$).

The p–W data were collected with a completely different (passive) target, segmented in 5 cylinders, 20 mm long and 4 mm in diameter, inter-spaced by 25 mm of air.

The active target was placed between a 'beam in' (BI) and a 'beam out' (BO) quartz Čerenkov counters, immune to the high radiation level (measured in Grad per day) and divided into four quadrants, to help centering the beam in the targets up to some 50 μm accuracy. The BI was also used to count the (ion) beam, providing some helpful redundancy and some monitoring of the BH stability.

Still in the target region were located 3 'telescopes', pointing at 90° to the target, 2 of them horizontally (to the left and to the right of the beam line) and the other one vertically (above the target). Each one of these monitors had 3 scintillator elements in triple coincidence. They were not used for beam alignment or any other precise task (they were somewhat sensitive to back-scattering from interactions in the dump), but they provided useful information as beam intensity monitors, again to cross check the stability of the other detectors.

For the 1991 data taking period, one more detector was added to the NA38 experiment, in the target box: an 'interaction monitor', placed just after the target (where it replaced the BO) and with a center hole to let the non interacting beam go through (that's why it was named 'Out of Beam' or OB). This quartz Čerenkov detector, only sensitive to the produced (*secondary*) particles, was used to define an interaction ('minimum bias') trigger. Therefore, it allowed the measurement of an $E_{\rm T}$ distribution not biased by the dimuon trigger, quite useful in the comparison of the $E_{\rm T}$ distributions from the 'J/ψ' or 'continuum' dimuon mass ranges. It also provided the best ('jitterless') time reference for the trigger, resulting in a jitter measured to be less than 0.2 ns. This detector was also able to detect whether there were two ions *interacting* in the target within the 20 ns time gate. The event selection cut based on the BH '*beam* pile-up', rejects many good events, since the probability to have an interaction in the target is only 18 % (for a target of 20 % of λ_I). This means that, although the BH counted two ions, 82 % of the times only one of them actually interacts in the target, creating the trigger. An '*interaction* pile-up' selection, therefore, saves a reasonable number of events from being rejected.

Another detector used to fight interaction (rather than beam) pile-up, is the calorimeter, also through the analysis of its signal shape, in 4 gates of 20 ns, recognizing events where there were two interactions superimposed on each other.

2.3.3 Electromagnetic calorimeter

The electromagnetic calorimeter gave us information on the 'centrality' of the event, allowing an estimation of the *nucleus–nucleus* collision energy density, by measuring the released transverse (neutral) energy. It was made of polystyrene scintillating fibers, parallel to the beam direction, embedded in lead. To prevent radiation damage effects, the glue used to fix the fibers in the 1986 and 1987 versions of the calorimeter was replaced by a net of thin steel cylinders positioned in the lead converter, where the fibers (of 0.95 mm diameter) were introduced. The volume occupied by the fibers, steel and air is half the volume of the lead. The assembly was very compact — 12 cm long, corresponding to $13\,X_0$ ($X_0 = 0.94$ cm) and $0.5\,\lambda_I$ ($\lambda_I = 27.2$ cm) — and positioned right after the target box (22 cm downstream from the central sub-target) to help fighting the π and K decays. The inner (beam) hole had a radius of 0.37 cm while the outer (hexagonal) border had a maximum radius of 12 cm. Its pseudo-rapidity acceptance ($1.7 < \eta < 4.1$) overlapped the dimuon window.

The calorimeter followed the hexagonal symmetry of the muon spectrometer and was further divided in 5 rings, in the 'standard' or 'J/ψ' configuration. In the 'ϕ' setups the central part (first three rings) was replaced by Al_2O_3, leaving the calorimeter with only the 2 outer rings (outside of the muon acceptance window). The corresponding 30 (or 12) read-out cells were digitized by fast electronics in a 20 ns time gate. Actually, 4 other 20 ns time gates were used, partially overlapping each other, to allow the pulse shape analysis that recognized double interactions (as long as they followed each other more than 5 ns apart).

While the chambers and hodoscopes of the muon spectrometer, protected by the muon filter, worked in comfortable conditions, illustrated by the trigger rate of about 100 per second, the 'NA38 specific' detectors, placed upstream of the hadron absorber, had to work at the extremely demanding rate of more than 10^6 collisions per second. The corresponding radiation damage was so high that the light collection properties of the calorimeter (specially the central cells) had to be continuously monitored and a (time dependent) efficiency correction applied, on a run per run basis[4]. For example, after 18 days of running in 1990, with the sulphur beam, the inner ring of the calorimeter suffered a radiation dose around 0.4 Mrad, leading to a 16 % decrease in the light collected. After efficiency correction, the overall systematic error on the E_T measurement is estimated to be less than 2 %.

Besides the continuous monitoring provided by a laser, two absolute energy calibrations were usually done per data taking period (one at the beginning and the other at the end), with electron beams of several energies (typically 10, 20 and 30 GeV). The calorimeter was placed on a remotely controlled elevator platform which was able to move (both horizontally and vertically) to allow a complete $x - y$ scanning, so that all the cells could be equally well calibrated. The cells were centered on the beam axis with an accuracy of $\sigma_x = \sigma_y = 0.15$ mm.

From the calibration data taken with the electron beams, the *intrisic* resolution of the calorimeter is found to be

$$\frac{\sigma_E}{E} \approx \frac{20\,\%}{\sqrt{E}} + b\,. \tag{2.3}$$

The constant term, b, is very sensitive to the cell dimensions, decreasing from $\sim 5\,\%$ at the inner ring (where lateral leakage is important) to $\sim 0.3\,\%$ in the outer layer, where the cells are big enough to contain the lateral development of the electromagnetic shower. The radiation damage of the fibers leads, with time, to a deterioration of the resolution.

[4]This was also the case for the target scintillator hodoscope.

The primary purpose of the calorimeter is to measure the transverse *neutral* energy released in the *nuclear* collisions. Therefore, the relevant energy resolution is estimated through a Monte Carlo GEANT simulation, taking into account the energy deposited by the charged particles, and is given by

$$\frac{\sigma_{E_{\mathrm{T}}}}{E_{\mathrm{T}}} \approx \frac{47\,\%}{\sqrt{E_{\mathrm{T}}}}\,. \tag{2.4}$$

For values of E_{T} between 20 and 100 GeV, common in ion collisions, the resolution lies between 10 and 5 %.

Two corrections were applied (in the off-line processing) to the energy measurement given by the calorimeter. One was to correct for the (small) charged particles contribution, from the results of the GEANT simulation, and the other was to correct for the sub-target dependence of the rapidity window. The corrected result, used in the final analysis and referred to as E_{T}, corresponds to the *neutral* transverse energy, released in a given pseudo-rapidity range ($1.7 < \eta < 4.1$), whatever was the z position of the interaction sub-target.

2.3.4 Muon spectrometer

The muon spectrometer started with the hadron absorber, followed by 4 MWPCs (PC1 to PC4) and two trigger hodoscopes (R1 and R2). A second set of chambers and hodoscopes existed after the toroidal magnet, the last hodoscope being protected by an iron wall.

2.3.4.1 Hadron absorbers

The composition of the muon filter has changed between the several data taking periods. Typically, is was made of 40 cm of Al_2O_3 followed by 480 cm of carbon (corresponding to $22\,X_0$ and $11\,\lambda_I$, or 15 pion absorption lengths, enough to stop the hadron showers), completely covering the angular acceptance of the spectrometer ($\sim$ 35 to $\sim$ 120 m rad). For masses above 1 GeV the contamination from events originated in this absorber is negligible. The carbon blocks were involved by iron and concrete shielding and surrounded the tungsten (80 cm) and uranium (320 cm) plug used to stop the non-interacting beam. The muon filter material had to be chosen among low atomic number elements so that the muon trajectories would not be too much affected by the (Coulomb) multiple scattering. Therefore, some energetic hadrons were able to 'punch-through' the graphite blocks and cross the trigger hodoscopes giving a fake trigger. To prevent this from happening the last hodoscope, R4, was placed behind a 1.2 meter thick iron wall that absorbed the remaining hadrons. A higher Z element has been used in this wall since it was placed after all the MWPCs, therefore not affecting the dimuon mass resolution.

2.3.4.2 Magnet

The main component of the muon spectrometer was the air-core analyzing magnet, a 480 cm long toroid with hexagonal symmetry (a property that induced the hodoscopes and chambers geometry). The over-all 'radius' was 205 cm but the magnet acceptance was confined between an inner radius of 29.5 cm and an outer radius of 154 cm, values that determine the angular acceptance (and thus the rapidity window) of the whole experiment. The magnet was centered 11.3 m downstream from the center of the target. The central hole between the coils had a radius of 9.5 cm. In each sextant, 18° in azimuth, centered in the border lines of the hodoscope's sextants, were occupied by one of the 6 iron pole pieces, of 4 m length. To improve the mass resolution, the events (30 %) where one of the muons went through one of these iron sectors, therefore suffering further multiple scattering, were rejected (during the off-line processing). While the NA10 experiment used an exciting current of 10 000 A, the value used by NA38 was 4 000 A (with the exception of some special proton runs) to improve the acceptance in the low mass region. The current was pulsed, syncronized with the SPS cycle. The corresponding field is essentially azimuthal and $1/r$ dependent (see figure 2.5), with a value of 0.3 T at a mean radius of 75 cm:

$$\vec{B}(r) = B_0 \,/\, r \cdot \vec{e}_\phi = 0.219 \,/\, r \cdot \vec{e}_\phi \,. \tag{2.5}$$

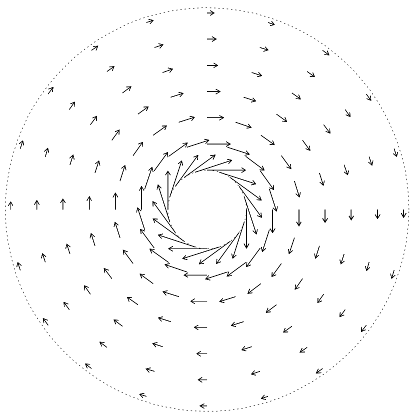

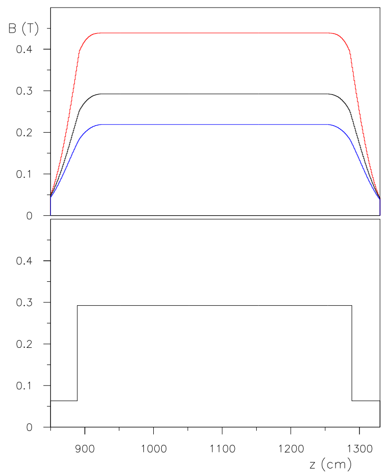

Figure 2.5: Field map in the transverse plane of the magnet (left) and along the z axis (right). B values are shown in the *air* sectors (top), for r = 50, 75 and 100 cm — leading to $\int B\,dl$ values of 1.89, 1.26 and 0.95 T m — and in the *iron* sectors (bottom), for r = 75 cm.

In this kind of field, and with the magnet axis aligned with the beam line, a particle emitted from the target keeps its azimuthal plane (the trigger logic, explained below, was based on this property). The deflection (polar) angle is, to a very good approximation, inversely proportional to the particle's p_{T},

$$\Delta\theta = p_0/p_{\mathrm{T}} \; , \tag{2.6}$$

where p_0 was 23 m rad GeV in the NA38 configuration (it was 61 m rad GeV in the NA10 setup).

This dependence on p_{T}, rather than on p as in the case of a dipole (constant) field, is at the essence of the design of the whole experiment, therefore deserving a more detailed explanation. Consider the curvilinear coordinate s, along the muon track. The deflection angle, $\mathrm{d}\theta$, induced in the track by the magnetic field is, at each incremental step $\mathrm{d}z = \mathrm{d}r/\tan(\theta)$, given by

$$\mathrm{d}\theta = \frac{\mathrm{d}s}{\rho(s)} = \frac{q \cdot B(r)}{p}\,\mathrm{d}s \; , \tag{2.7}$$

where ρ is the radius of curvature of the (helicoidal) path followed by a particle of charge q in the magnetic field B. For energetic particles the deflection is small and the integration path, s, can be replaced by $r\,/\,\sin(\theta)$, leading to

$$\Delta\theta = \int \frac{q \cdot B(r)}{p}\frac{\mathrm{d}r}{\sin(\theta)} = \frac{q \cdot B_0}{p \cdot \sin(\theta)} \int \frac{\mathrm{d}r}{r} = \frac{q \cdot B_0}{p_{\mathrm{T}}}\,\ln(z_2/z_1) \; , \tag{2.8}$$

z_1 and z_2 being the effective entrance and exit planes of the magnetic field, relative to the target position.

To prevent any systematic effects related to the field signal, the polarity has been reversed every few runs. The magnitude of the field was continuously measured by a Hall-effect probe. The measured field map was parameterized analytically by polynomial and spline functions to be used in the off-line simulation and reconstruction programs.

2.3.4.3 Detectors

The muon spectrometer detectors, trigger (R) hodoscopes and Multi-Wire Proportional Chambers (PC), all of hexagonal shape, are listed in table 2.1, in the order traversed by the muons.

The 4 R hodoscopes were used to trigger the data aquisition system. The first two, located upstream of the magnet, had an homothetic geometry pointing to the target region. The 30 scintillator slabs of each sextant, disposed parallel to the outer border, had a width that increased radially, from the most central one, in a geometrical progression[5]. This way, the slabs touched in R1 and R2 by a particle emitted from the target, with any production angle, had always the same sequential index, i (with $i = 1, \ldots, 30$). A coincidence $R_1^i \times R_2^i$ ensured that

[5]The R1 slabs slightly overlapped each other.

Label	z (cm)	Main characteristics
PC 1	547	y, u, v planes; 448 wires per plane; $\oslash = 134$ cm
R 1	560	6×30 scintillator slabs of 1.05–3.55 cm width
PC 2	643	y, u, v planes; 512 wires per plane; $\oslash = 153$ cm
PC 3	740	y, u, v planes; 572 wires per plane; $\oslash = 172$ cm
R 2	784	6×30 scintillator slabs of 1.25–3.85 cm width
PC 4	835	y, u, v planes; 640 wires per plane; $\oslash = 192$ cm
Magnet	850–1333	
PC 5	1365	y, u, v planes; 1024 wires per plane; $\oslash = 306$ cm
R 3	1436	6×24 scintillator slabs of 5.5 cm width
PC 6	1486	y, u, v planes; 1088 wires per plane; $\oslash = 326$ cm
PC 7	1607	y, u, v planes; 1152 wires per plane; $\oslash = 345$ cm
PC 8	1725	y, u, v planes; 1216 wires per plane; $\oslash = 364$ cm
Iron wall	1742–1862	
R 4	1882	6×32 scintillator slabs of 5.5 cm width

Table 2.1: Detector components of the muon spectrometer. The z scale, inherited from NA10, starts 45 cm downstream of the target center (see figure 2.4).

only such configurations could give a trigger. Actually, to account for the spacial extension of the target system, its displacement from the NA10 target position and to allow for some multiple scattering in the muon filter[6], the coincidence $R_1^i \times R_2^{i-1}$ was also made valid (a difference relative to the NA10 setup).

Since each scintillator slab was read only once, at one of its ends, the time taken by the (scintillating) light to reach the PM depended on the point where the muon hit the slab, originating time fluctuations in the trigger (*jitter*). To prevent this from happening, the R2 hodoscope was reversed in relation to its position in the NA10 configuration, so that the slabs in R2 were read from the end opposite to the one used in the reading of the corresponding R1 slabs. Both signals were then sent into a 'mean timer' making the final signal quite insensitive to the specific muon trajectories. The slabs of the R3 and R4 hodoscopes (24 and 32, respectively) had all the same width (5.5 cm). Figure 2.6 illustrates the information provided by the R hodoscopes, displaying a typical event collected with a proton beam.

The 8 MWPCs had 3 independent (anode) wire planes, inter-spaced by 2.2 cm, with a 60° relative rotation, each of them protected by 2 graphited Mylar (cathode) planes. All these 24 wire planes had 20 μm gold-plated tungsten wires of 3 mm inter-spacing. The 4 chambers upstream (downstream) of the magnet had 749 (1229) wires per plane, but only those in the acceptance region were equipped with pre-amplifiers (see table 2.1). The gas mixture used in the chambers contained argon (80 %), isobutane (19.8 %) and freon (0.2 %), being continuously monitored from the 'counting room'. Figure 2.7 illustrates the chambers operation, displaying

[6]The multiple scattering affects more the low masses, not so important for NA10.

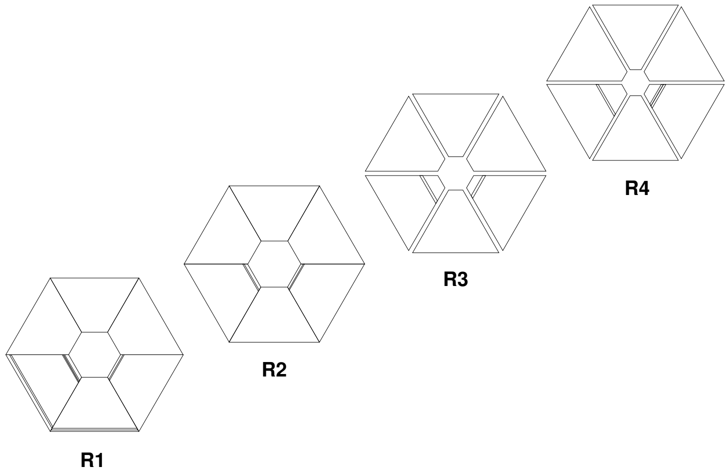

Figure 2.6: Trigger hodoscopes information in a typical p–A event.

the same event as already viewed in figure 2.6. After several years of operation under demanding rates, these reliable and tireless chambers have been recently subject to a check-up before serving a few more years under the command of the NA50 experiment (the follow up of NA38).

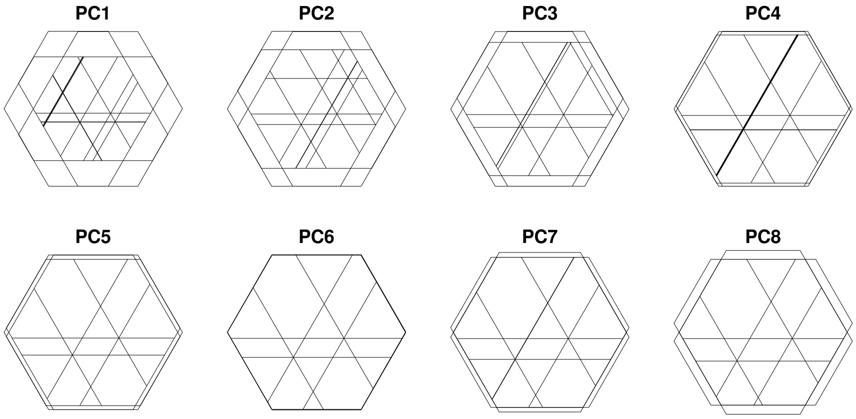

Figure 2.7: Chambers information for the same event as figure 2.6.

2.3.4.4 Alignment

The alignment of all the components of the muon spectrometer is an important factor in the final quality of the measurements. Every new period of data taking started with a special 'alignment' run, using a *single muon* trigger, a low intensity beam and no magnetic field. The off-line track reconstruction of these events imposes adjustments in the set of parameters defining the chambers' geometry, so that perfect straight lines are obtained. Typical displacements were of the order of 0.1 mm. Such special runs only allowed the alignment of the eight chambers among them selfs, while their alignment with the 'theoretical' beam (and magnet) axis would require tracking back the muon tracks through the muon filter, where the multiple scattering deteriorates the precision of such a procedure.

2.3.4.5 Mass resolution

The dimuon mass resolution (actually, the momentum resolution of each muon) is essentially determined by the multiple scattering suffered by the muons while crossing the hadron absorber, therefore depending on its specific configuration (materials and geometry). The magnetic field (through the momentum kick, see equation 2.6) and the inter-spacing of the wires in the chambers (besides the number of chambers), are other important variables in this respect, but were kept constant during the NA38 data taking periods (except for a special proton period when the current in the magnet was 10 000 A instead of 4000 A).

Two setup configurations were developed for the hadron absorber. In the 'standard' (or 'J/ψ') setup the mass resolution at the J/ψ mass was $\sim$ 120 MeV, while in the 'high resolution' (or 'ϕ') version is was closer to $\sim$ 100 MeV. The difference is that the inner part of the calorimeter, in the muon's rapidity window, was replaced by Al_2O_3, thereby removing 11.5 X_0 from the (start of) the muon tracks. The signal to background ratio follows this change. Indeed, the best possible resolution requires the minimum amount of radiation lengths (X_0) in the path of the muons, while to completly absorb the hadronic shower, thereby minimizing the number of decay muons, a large number of interaction lengths (λ_I) is necessary, ideally in the shortest geometrical length. The materials providing the largest λ_I to X_0 ratio are carbon, Al_2O_3 and Be O.

2.4 Trigger

As already described above, the trigger system was based on the information given by the 4 R hodoscopes. The R1–R2 coincidence, which by it self gives an estimation of the muon's trajectory before the magnet, was combined with the R4 information to provide a rough measurement of the deflection angle (at the magnet central plane) and, therefore, the muon's p_{T}. The R3 hodoscope (redundant) information was very useful to clean away accidental coincidences between two uncorrelated tracks. The 'standard' dimuon trigger required that the two muons were in different sextants.

Some basic 'cleaning' was performed at the trigger level by rejecting events with too many hits (in the hodoscopes alone or including the chambers). In good running conditions these cuts (whose threshold values changed from protons to ions) were barely effective, but at very high beam intensities they were useful in fighting spurious events.

Other, more sophisticated and 'physics oriented', selection cuts have been used at the trigger level during some (partial) periods of data taking, usually when the ion beam provided by the SPS was too intense for the data aquisition system to follow. Since the central ion collisions were considered to be the most interesting ones, a cut based on the total energy collected in the calorimeter was used (for a very short time) to reject peripheral events. The oxygen data collected in 1986 and some of the sulphur data collected in 1987, were subject to the so-called DD cut. Each muon has an associated signal (A, B, C or D) according to its p_{T} value, estimated as explained above. For example, a muon tagged as D has a p_{T} value below ~ 0.6 GeV. If both muons are D, the corresponding dimuon mass, estimated as the sum of the muon's p_{T}, has a small value. This provided a simple way to have a rejection of low mass muon pairs, the most abundant ones. This cut was not applied in the data taking periods that occurred after 1987, both because of the improvements introduced in the data aquisition system (to cope with higher trigger rates) and because it was found that such cuts were dangerous for the background subtraction procedure.

2.5 Data-acquisition system

The events that survived the trigger selection criteria were recorded in tape by the data acquisition system (DAS), also responsible for the on-line monitoring of the experience.

The first NA38 DAS, following the NA10 architecture existing on the floor, was based on the CAMAC bus and on a tandem of Nord computers, ND100 and ND500, sharing a common memory. The CAMAC–NORD system (with a bandwidth around 800 k byte/s) was clearly pushed to its limits in 1987, when it was exposed to the high trigger rate induced by the sulphur beam. Indeed, with almost 500 triggers per burst (of ~ 4 s) and an average event size of ~ 320 (16-bit) words, a data aquisition rate of ~ 80 k byte/s was easily reached, leading to an uncomfortable readout dead time of 10 %. Looking ahead into the future, the follow-up experiment, planned in view of the forecasted lead beam and later named NA50, could not continue with such a system.

This is why a second DAS was designed, with the goal of collecting much larger amounts of data, at a rate ~ 1.5 M byte/s. This new system uses VME as the acquisition bus, burst buffer memories and a VAX computer for the operations control. The data is read at the front-end modules, stored in the burst buffer memories until the burst ends and, during the inter burst time, recorded in tapes directly from the VME. Such a major change had to be implemented in successive steps and preliminary versions of this new system were used in the data taking periods from 1990 onwards, checking and storing up to ~ 2 M bytes every 15 seconds (burst frequency), corresponding to more than 500 triggers per burst.

References:

[And 84] L. Anderson *et al.* (NA10 Coll.), Nucl. Inst. Meth. **223** (1984) 26.

[Gat 93] L. Gatignon, private communication, and CERN Yellow Report 80-07.

Chapter 3

Data reduction and normalization

The data reduction of this experiment was quite a lengthy process, taking more than one year between the 'raw data' collection and the final stage of data compression: the writting of the μDSTs ('*micro* data-summary tapes'). The raw data information is stored, according to a structure containing three hierarchical levels: 'runs', 'bursts' and 'events'. A run is characterized by several parameters, like the beam particle, the target configuration, the trigger type, etc. The burst level contains the kind of information useful for the data normalization, like the 'scallers' that integrate the number of incident particles counted along the burst or the fraction of pions in the (secondary) proton beam, for instance. The event records contain all the information provided by the detectors each time there is a trigger, like which hodoscope slabs and chamber wires were hit, all the ADC contents, etc.

These tapes were processed by the experiment's reconstruction program, named DIMUREC, giving higher level information: the kinematical variables of the muons, the interaction vertex, the transverse energy measured in the calorimeter, etc. It is at this level that some basic off-line selection cuts are applied, like the rejection of events in which one muon (or both) had azimuthal angles covered by the iron pieces of the magnet or had trajectories going outside of the fiducial region where the chambers and hodoscopes have $\sim 100\,\%$ efficiency. The selected events must have 2 tracks reconstructed in the multiwire proportional chambers (pointing to the target region) and in such a way that the corresponding hodoscope counters were fired and satisfy the trigger requirements. For each of the selected events, a restricted set of 'physics oriented' variables are written in the 'final analysis' data files (the μDSTs), small enough to be read numerous times in a reasonable amount of computer time.

3.1 Data taking periods and setup description

The analysis presented in this work has been done using eight sets of data, collected in several time periods and using different experimental setups, two for p–W collisions, two for p–U collisions and four for S–U collisions. They will be refered to by labels containing the projectile and target identification plus the year of data taking (and when two different setups were used for the same projectile–target combination in the same year, a few more letters provide the necessary discrimination): pW 88 V, pW 88 D, pU 87, pU 88, SU 90 St, SU 90 Al, SU 91 Phi and SU 91 Psi. The experimental setups used in each data taking period differ in what concerns the materials and dimensions of the hadron absorbers. The beam momentum was always 200 GeV per incident nucleon. The main specific characteristics of each data set are schematically summarized in the following lines.

We start with the target configuration description. While the p–W data were taken with a fractioned target of 5 cylindrical pieces, the p–U and S–U data used the 'standard' active target, with a number of sub-targets, dimensions and z positions (along the beam axis) variable from data set to data set. See table 3.1 for some numerical values.

Label	Configuration
pW 88 V	5; l=20.0; $\oslash$=4.0
pW 88 D	5; l=20.0; $\oslash$=4.0
pU 87	16; $10 \cdot 10 \cdot 1.7$ (1); $2.0 \cdot 3.5 \cdot 1.7$ (5); $1.0 \cdot 3.0 \cdot 1.0$ (10)
pU 88	16; $10 \cdot 10 \cdot 1.7$ (1); $2.0 \cdot 3.5 \cdot 1.7$ (5); $1.0 \cdot 3.0 \cdot 1.0$ (10)
SU 90 St	10; $10 \cdot 10 \cdot 1.0$ (1); $1.0 \cdot 2.0 \cdot 1.0$ (9)
SU 90 Al	10; $10 \cdot 10 \cdot 1.0$ (1); $1.0 \cdot 2.0 \cdot 1.0$ (9)
SU 91 Phi	10; $10 \cdot 10 \cdot 1.0$ (1); $1.0 \cdot 2.0 \cdot 1.0$ (9)
SU 91 Psi	10; $10 \cdot 10 \cdot 1.0$ (1); $1.0 \cdot 2.0 \cdot 1.0$ (9)

Table 3.1: Target configurations. The number of sub-targets is followed by their dimensions (in mm). W: length and diameter; U: x, y and z dimensions.

The A of the (impure) tungsten is estimated to be 184.7, the corresponding density being $\rho = 19.13$ g/cm^3, while the uranium material has the standard values $A = 238.0$ and $\rho = 19.8$ g/cm^3.

Important changes occured in the experimental setups used in the several data taking periods. The geometrical configurations of the absorber materials placed in the angular acceptance of the spectrometer are displayed in figure 3.1. In this figure, the solid arrows represent the beginning of the 'NA10' muon filter, composed of 480 cm of carbon, except in the setup SU 91 Psi where the last 80 cm were replaced by iron.

3.2 Event selection and luminosity calculations

Since we are interested in measuring absolute cross–sections, we have rejected the runs that seemed to have normalization problems. For instance, we have seen the evolution of the ratio between the number of J/ψ events and the number of incident particles counted by the BH detector, as a function of the run number. In the case of incident protons, we have also seen the evolution of the percentage of protons in the beam as a function of the run number. Runs with values quite different from the mean value were rejected.

In the case of S–U runs from the 1991 data taking periods, we have kept the runs with unknown normalization, to have better statistics in the relative results,

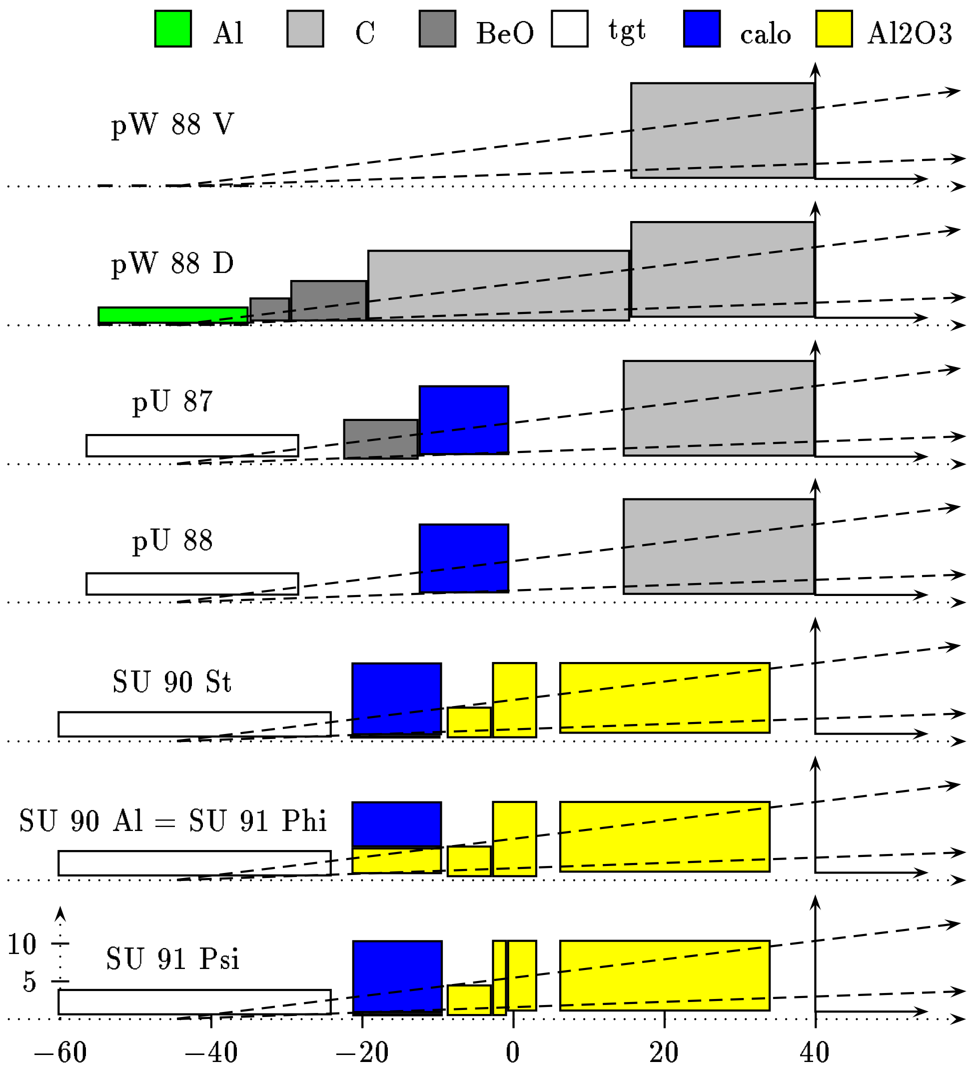

Figure 3.1: Configurations of the 'pre-dump' absorber materials as parametrized in the simulation and reconstruction programs. The dashed arrows show the angular acceptance of the spectrometer (35 to 120 m rad), while the solid arrows represent the start of the 'NA10' muon filter. The calorimeter is identified as 'calo' while 'tgt' stands for 'target box'.

like ratios of particle production. The absolute cross section results are obtained from the luminosity values of the data sets collected in 1990.

In order to extract absolute cross–sections we must know the luminosities ($\mathcal{L}$, specific of each data set) and the acceptances (A, dependent on the physical process). For instance, the J/ψ production cross–section, times its branching ratio into muon pairs, $B\sigma^{J/\psi}$, is given from the number of measured events ($N^{J/\psi}$, already corrected for the event specific efficiencies), according to

$$N^{J/\psi} = \mathcal{L} \cdot B\sigma^{J/\psi} \cdot A^{J/\psi} \,. \tag{3.1}$$

In the p–W case, the (uncorrected) luminosity is calculated as

$$\mathcal{L} = N_{\rm targ} \cdot N_{\rm inc} \cdot \epsilon_{p/(p+\pi)} \,, \tag{3.2}$$

where $N_{\rm inc} \cdot \epsilon_{p/(p+\pi)}$ is the number of beam *particles* that cross the BH monitor times the fraction of *protons* in the beam, estimated to be 58 % from the information provided by the Čerenkov detectors. $N_{\rm targ}$, the number of target nuclei, is calculated to be 0.390 b^{-1}, using the standard formulas

$$N_{\rm targ} = \frac{N_A \cdot \rho \cdot l_{\rm eff}}{A} \qquad l_{\rm eff} = \lambda_I \cdot (1 - {\rm e}^{-L/\lambda_I}) \,, \tag{3.3}$$

where L is the total length of the tungsten target (10 cm). To get the effective luminosity we must consider the efficiencies of the trigger ($\epsilon_{\rm trig} = 94\,\%$) and of the track reconstruction procedure ($\epsilon_{\rm rec} = 99\,\%$). A final correction, of 5 %, has been applied to account for the fraction of the beam, counted by the BH, that is not intercepted by the target. The lifetime corrections are already included in the $N_{\rm inc}$ values.

The integrated luminosities of the p–W data sets (already corrected for the efficiencies) are 0.153 pb^{-1} for pW 88 V ($N_{\rm inc} = 7.65 \times 10^{11}$) and 0.132 pb^{-1} for pW 88 D ($N_{\rm inc} = 6.61 \times 10^{11}$). From these numbers we see that the data set pW 88 V (pW 88 D) contributes with $\sim 54\,\%$ ($\sim 46\,\%$) of the total number of p–W *signal* events.

The p–U and S–U data were taken with the active target, composed of 16 (p–U) or 10 (S–U) thin sub-targets, of which only the first ones are big enough (1 cm^2) to intercept all the beam spot (see table 3.1). We calculate the effective length of the whole target from the length of the first sub-target, $l(1)$, using the ratio between the number of events (with dimuon mass between 2.7 and 3.5 GeV, where the background fraction can be neglected) produced in all sub-targets, $N(all)$, and in the first sub-target, $N(1)$. The BI detector, placed upstream from the target, absorbs a fraction, $a_{\rm BI}$, of the beam counted by the BH detector, $N_{\rm inc}$. The events where a reinteraction in a downstream sub-target is detected are rejected from the final analysis sample. In the case of S–U collisions, in order to have a good measurement of $E_{\rm T}$, the events with pile-up are also rejected. In the analysis of the p–U data sets, where E_{T} is not studied, this cut was not applied. Very peripheral S–U collisions, with E_{T} below 10 GeV, were rejected. The sub-target recognition algorithm has a poor efficiency for such low multiplicity events (more details further down) and the background subtraction is also more uncertain. We have estimated the fraction of events surviving this cut, $A_{E_{\mathrm{T}}}$, using the E_{T} distribution before applying the sub-target recognition algorithm. We must correct for this 'acceptance' to obtain the total (all E_{T}) cross sections. In the p–U data, if the interaction sub-target was not identified, the vertex was assumed to be at the center of the target system. This way we overcome the (E_{T} dependent) correction for the vertex identification inefficiency.

The luminosity of the p–U data sets is given by

$$\mathcal{L} = \frac{N_A\ \rho\ l(1)}{A} \cdot \frac{N(\mathrm{all})}{N(1)} \cdot N_{inc} \cdot (1 - a_{\mathrm{BI}}) \cdot \epsilon_{\mathrm{trig}} \cdot \epsilon_{\mathrm{rec}}\ , \tag{3.4}$$

where N_{inc} already includes the corrections for lifetime and for pion contamination, $\epsilon_{p/(p+\pi)}$, while for the S–U data we have

$$\mathcal{L} = \frac{N_A\ \rho\ l(1)}{A} \cdot \frac{N(\mathrm{all})}{N(1)} \cdot N_{\mathrm{inc}} \cdot (1 - a_{\mathrm{BI}}) \cdot \eta_{\mathrm{reint}} \cdot \eta_{\mathrm{pileup}} \cdot \epsilon_{\mathrm{trig}} \cdot \epsilon_{\mathrm{rec}} \cdot A_{E_{\mathrm{T}}}\ . \tag{3.5}$$

where $N(\mathrm{all})/N(1)$ is calculated before rejecting events with reinteractions. Table 3.2 collects the parameters needed for the luminosity calculations and the corresponding results. The derivation of the p–U luminosities reveal the existence of some inconsistencies raising some doubts on their reliability. Indeed, although the target system was the same in both years, the fraction of J/ψ events originating from the first sub-target was quite different (8.9 % in 1987 and 10.5 % in 1988) suggesting some different beam–target alignments. Also, the algorithm that makes the recognition of the interaction sub-target, identifies some events (4 %) with a re-interaction in another sub-target. The existence of such events (rejected from the analysis sample) seems very strange considering that the incident particle is a single proton.

3.3 Kinematical region studied

The final sample of events to be analysed was selected on the basis of the kinematical variables defining the muon pairs: the invariant mass, the rapidity, the transverse momentum, the laboratory azimuthal angle and the angles θ and ϕ, defined by the direction of the μ^+ (if there is one) relative to the beam direction in the muon pair rest frame. In the present analysis we have chosen to work in the mass region above 1.5 GeV (so that the low mass vector mesons can be neglected). The chosen kinematical window is further determined by $3.0 < y < 4.0$ (y being the *lab* rapidity) and $|\cos(\theta)| < 0.5$, since outside of these windows the acceptance

	pU 87	pU 88	SU 90 St	SU 90 Al
$l(1)$ (mm)	1.625	1.625	1.00	1.00
$N(\text{all})/N(1)$	11.2	9.53	9.03	8.80
N_{inc} ($\times 10^{11}$)	16.5	4.85	3.12	1.72
a_{BI} (%)	0.8	0.8	3.15	3.15
η_{reint}	0.963	1	0.871	0.913
$\eta_{\text{pile-up}}$	1	1	0.916	0.834
ϵ_{trig}	0.94	0.94	0.94	0.94
ϵ_{rec}	0.99	0.99	0.992	0.978
$A_{E_{\text{T}}}$	1	1	0.92	0.92
$\mathcal{L}$ (nb^{-1})	128	33.2	8.95	4.50

Table 3.2: Parameters for the luminosity calculations.

of the detector becomes too small. The results in this work are averaged over the other three (non-cutted) kinematical variables. Figure 3.2 displays the kinematical window in the x_1–x_2 and in the M_{T}–y planes, using S–U data.

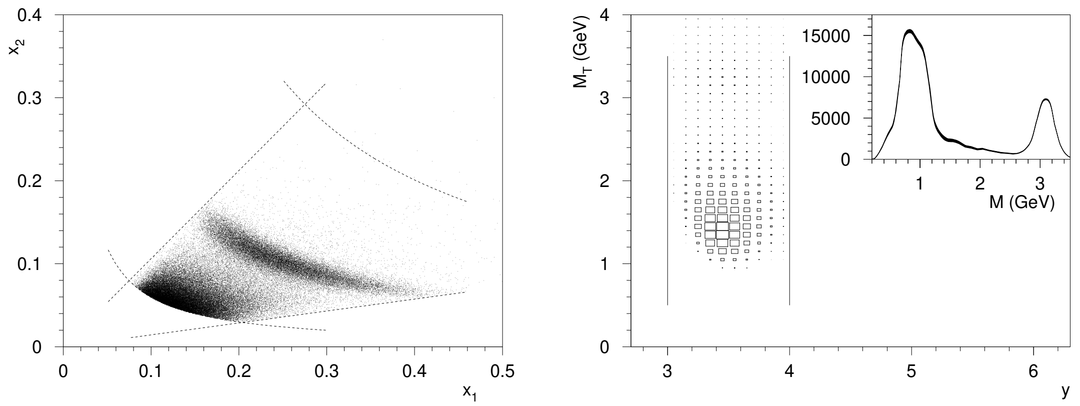

Figure 3.2: Left: Event distribution in the x_1–x_2 plane, from the SU 91 Psi data. Border lines for y = 3, 4 and M = 1.5, 5.5 GeV are indicated. Right: Event distribution in the M_{T}–y plane, from the SU 91 Psi data. The insert shows the corresponding *mass* distribution.

Although the p_{T} and y variables are not emphasized in this work, they were properly taken into account in the Monte Carlo simulation of the experiment (as explained in the next chapter), to ensure the calculation of reliable acceptances.

3.4 The 'image' cut

The estimation of the combinatorial background contribution to the 'opposite-sign' muon pair mass spectra relies heavily on the (also measured) 'like-sign' events. It is, thus, very important to understand whether the detector treats in a different way the $\mu^+\mu^-$ pairs relative to the $\mu^+\mu^+$ or $\mu^-\mu^-$ ones. The high trigger rate of NA38 has allowed the introduction, at the trigger level and in the offline event selection chain, of a special cut, named 'image cut', that eliminates any such bias. Indeed, an event is only accepted for analysis if the other combinations of the muons' charge and spectrometer's magnetic field signal would also fulfill the trigger requirements, implying that

$$A^{+-} = A^{++} = A^{--} \tag{3.6}$$

This 'regularization of acceptances' implies the rejection of around 50 % of the collected events, most of them from the low mass region. The effect of this cut is incorporated in the (Monte Carlo) acceptance calculation, thereby not affecting the luminosity calculations.

3.5 Efficiency of sub-target identification

The sub-target where the interaction took place is identified from the information provided by the 'target hodoscope'. An interaction in a given sub-target is recognized as a peak in the two adjacent scintillators, mainly due to recoil protons, while the downstream scintillators collect the energy lost by the secondary charged particles (mostly pions) and by the charged component of the electromagnetic shower developed by neutral particles (mostly photons from π^0 decays) while crossing the sub-target thickness. This is illustrated in figure 3.3 together with a distribution of events versus the interaction sub-target. Notice the different 'slope' of the opposite-sign and signal data points.

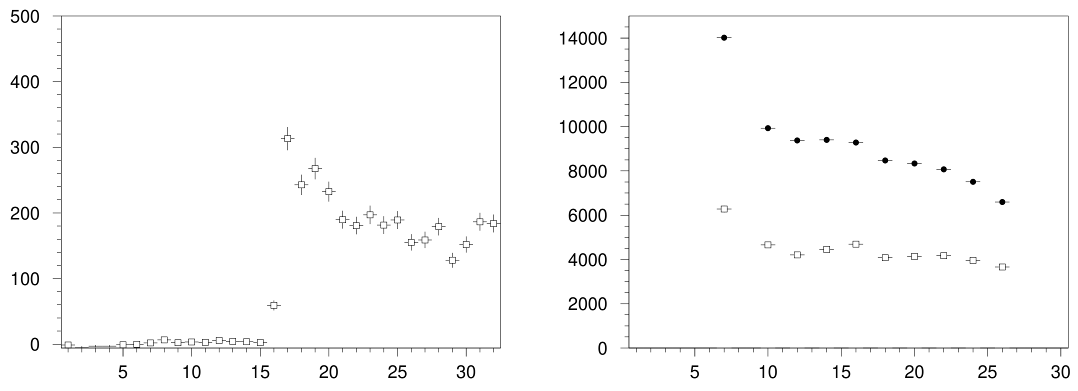

Figure 3.3: Left: Target hodoscope pattern of a S-U collision in sub-target 16. Right: Distributions of the 'signal' (open squares) and 'opposite-sign' (closed circles) events versus the interaction sub-target, for the SU 91 Psi data set.

The algorithm used to identify the interaction sub-target has a very low efficiency for the most peripheral collisions, as can be seen in figure 3.4, for which the scintillator signals are too weak. To prevent the use of large correction factors, the events with E_{T} smaller than 10 GeV were rejected from the final analysis sample.

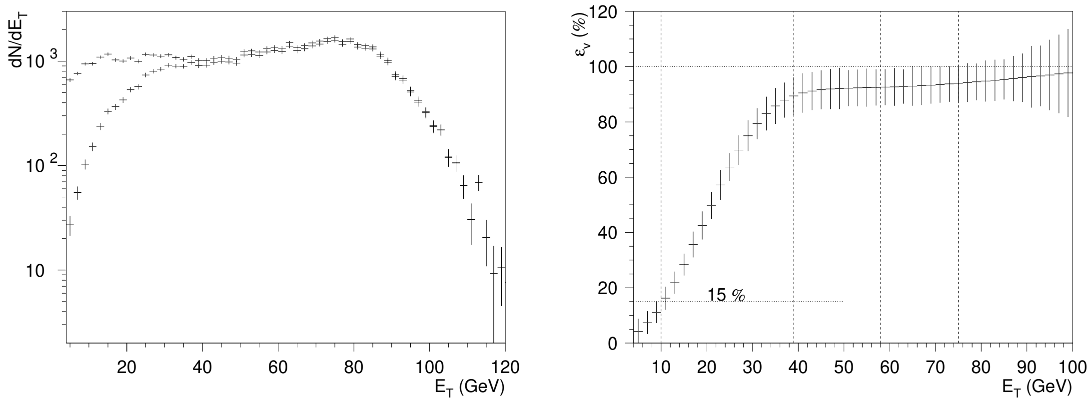

Figure 3.4: E_{T} distributions in the SU 91 Psi data set (left) before and after correcting for the vertex efficiency (right).

In order to get absolute cross–sections in S–U collisions, we must correct for this low E_{T} cut. To do this correction we must estimate the fraction of the *physical* E_{T} distribution (before being biased by the detector's limitations) that we are accepting. How can we get a good estimation of the physical E_{T} distribution when our vertex efficiency is uncertain in the low E_{T} region? Since we cannot properly correct for the sub-target identification cut, we will not use it, in this task of estimating our 'acceptance' in E_{T}. For each event, if the algorithm is unable to find the interaction sub-target, instead of rejecting the event we postulate that the interaction took place in the middle of the target. We still reject the events for which the algorithm was efficient in identifying a re-interaction in the target or an interaction in the 'BI' detector (located up-stream of the sub-targets system). The dimuon mass resolution might be somewhat deteriorated for these events (because the track reconstruction will use an incorrect vertex assignment) but this is irrelevant since, to estimate the E_{T} acceptance, we will only use the spectrometer information to select the (signal) events with mass above 1.5 GeV. Unfortunately, the calculation of E_{T} will also be slightly affected, since it also needs the vertex information (namely to give a value always corresponding to the same rapidity window, whatever the interaction sub-target). A second bias is induced by the interactions that took place in the BI detector *and* were not identified as such by the algorithm. We cannot circumvent these two effects but their influence on the 'measurement' we are after is certainly negligible. The value obtained for $A_{E_{\mathrm{T}}}$ is 92 %, as included in table 3.2. There is no evidence that this value changes between the J/ψ mass window (2.7–3.5 GeV) and the 'continuum' range (1.5–2.5 GeV).

Chapter 4

Processes contributing to the dimuon mass spectra

In order to search for new phenomena in nuclear collisions, through the analysis of dimuon production, it is essential to understand the 'classical sources' — processes known to contribute to the p–A spectra. A realistic model of the properties of such 'expected' sources must be defined on the basis of 'previous knowledge' (as exposed in chapter 1) and checked by comparison with p–A data (see next chapter). The 'expectations' for the S–U data require some hypothesis on the (beam) A-dependence.

When we are trying to understand the observed data as a superposition of several (known to exist) processes, it is of crucial importance to 'correctly disform' the *theoretical* images as if they were being viewed through the 'eye glasses' of the *experimental* detector.

4.1 Simulation of the signal processes

Apart from the combinatorial background, we have assumed that the J/ψ and ψ' production, the Drell–Yan mechanism and the semi-leptonic decays of the $D\bar{D}$ mesons, are the only *signal* processes that give a significant contribution to the mass spectra above 1.5 GeV. These four processes have been simulated for each of the eight experimental setups considered in this work.

For the generation of J/ψ events we have used a gaussian rapidity distribution, with $\sigma = 0.6$, and a uniform $\cos(\theta)$. The M_T was generated as $K_1(M_T/T)$, where K_1 is the modified Bessel function and T=195 MeV for p–A and 236 MeV for S–U. These values were tuned in successive iteractions until they provided a good reproduction of the measured y and p_T distributions of the events with mass between 2.7 and 3.5 GeV (see figure 4.1). The ψ' events were generated with the same functions except for the different mass value.

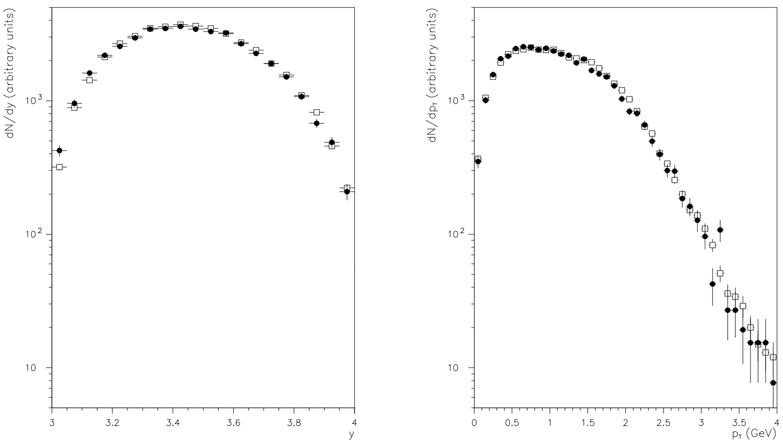

Figure 4.1: y and p_{T} 'signal' distributions measured for mass values between 2.7 and 3.5 GeV (black circles) compared to those obtained by Monte Carlo for J/ψ production (open squares). This figure corresponds to the SU 90 St data set.

We have used the PYTHIA (version 5.6) Monte Carlo program [Sjo 94], as an event generator for the Drell–Yan and charm (hard scattering) processes, using the appropriate leading order (LO) matrix element calculations. We have used the recent GRV LO parametrization [Glu 92] for the nucleon structure functions ($\Lambda_{QCD} = 200$ MeV; $Q^2_{min} = 0.25$ GeV^2), as taken from the PDFLIB package [Plo 93]. The D$\bar{\mathrm{D}}$ events were generated with 0.80 GeV as the width of the gaussian primordial k_{T} distribution (to be in agreement with the measurements of the LEBC-EHS results [Agu 88]). The charm quark was assumed to have a mass, m_c, of 1.5 GeV.

PYTHIA's results are restricted to collisions of protons or neutrons. Since the valence quark composition is relevant for Drell–Yan, we have generated $p-p$, $p-n$, $n-p$ and $n-n$ collisions, in this case. For charm production this is not necessary, since gluon fusion dominates (around 80 % of the cross–section), and only $p-n$ collisions were generated. This simulation was extremely CPU demanding since most of the generated events did not give rise to a pair of muons in our phase space domain. Anyway, at least most of the events had muons in the final state, thanks to a change introduced in the D mesons branching ratios into muons. The correct values were kept in some (lower statistics) generation jobs, to get the parameters necessary for the estimation of the total charm cross–section (see next chapter).

It is important to know if the shape of the predicted charm contribution to the dimuon mass spectrum is sensitive to the m_c value or to the structure functions parametrization. We have addressed this question by comparing the mass distributions of the muon pairs originated by the decay of D and $\bar{D}$ mesons, obtained from PYTHIA (at the generation level, without any detector bias), with three different m_c values (1.20, 1.35 and 1.50 GeV) and three different parametrizations of the parton distribution functions (DO 1, MRS 1 and GRV LO). All the (nine) *shapes* of the resulting mass spectra can be superimposed, within the statistical fluctuations, without any visible (systematic) distinction.

The corresponding predictions for the absolute charm cross section, however, are quite sensitive to the choice we make on these two 'parameters'(see table 4.1). Therefore, the values of our analysis will be directly compared to those previously measured by other experiments (see section 1.10 on page 21).

m_c	Structure Functions		
(GeV)	DO 1	MRS 1	GRV LO
1.20	4.99	2.80	2.50
1.35	2.51	1.37	1.21
1.50	1.29	0.691	0.622

Table 4.1: $\sigma_{pn}^{c\bar{c}}$ (in μb) from Pythia at $E_{\rm Lab}$ = 200 GeV, versus the structure functions parametrization and m_c.

For completeness, we also include the calculated dependence of the charm cross–section on the $k_{\rm T}$ parameter (table 4.2) and on the collision energy (table 4.3).

m_c	$k_{\rm T}$ (GeV)		
(GeV)	0.44	0.64	0.80
1.35	1.23	1.24	1.23
1.50	0.631	0.631	0.630

Table 4.2: $\sigma_{pn}^{c\bar{c}}$ (in μb) from Pythia at E_{Lab} = 200 GeV, for *GRV LO* versus m_c and $k_{\rm T}$

$E_{\rm Lab}$	m_c	Structure Functions		
(GeV)	(GeV)	DO 1	MRS 1	GRV LO
400	1.2	10.7	6.81	6.23
	1.5	3.47	2.06	1.81
800	1.2	19.5	14.0	13.7
	1.5	7.37	4.86	4.40

Table 4.3: $\sigma_{pp}^{c\bar{c}}$ (in μb) from Pythia versus S.F., m_c and $E_{\rm Lab}$.

In what concerns Drell–Yan, it is well known that the leading order predictions (as provided by PYTHIA) have to be multiplied by the K-factor when being compared to measurements (see section 1.8).

To go from the nucleon–nucleon Drell–Yan cross–sections to the p–A and S–U values, we have assumed a linear A-dependence, neglecting any nuclear effects on the quark distributions. This seems to be a reasonable procedure, considering that our data is placed at x values ($\sim$ 0.02 for the projectile and $\sim$ 0.08 for the target) where the *quark* distribution functions are not very much affected by nuclear effects (see ref. [Cas 93]). According to figure 4.2, there is no visible enhancement (anti-shadowing) in Drell–Yan production, in the $x \sim 0.1$–0.2 region.

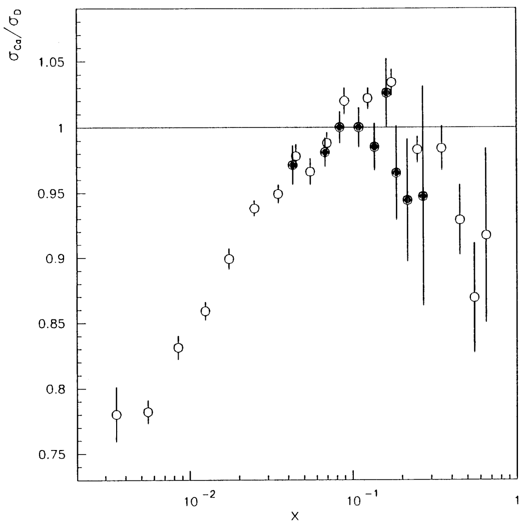

Figure 4.2: Ratio $\sigma_{\mathrm{Ca}}/\sigma_{\mathrm{D}}$ of Drell–Yan cross–sections, from E 772 (closed circles) [Ald 90] compared to the DIS results of NMC (open circles) [Ama 91], as a function of x. [Figure taken from Arn 94]

For the kinematical domain we are interested in, the cross–sections obtained from PYTHIA are: $\sigma_{pp} = 270$ pb; $\sigma_{pn} = 261$ pb; $\sigma_{np} = 215$ pb; $\sigma_{nn} = 199$ pb; $\sigma_{pW} = 48.9$ nb; $\sigma_{pU} = 62.9$ nb; $\sigma_{SU} = 1.79$ μb.

We have verified that PYTHIA gives a correct Drell–Yan 'prediction' by comparing its results for p–Pt collisions, at 400 GeV, in $0 < x_F < 0.4$, with the corresponding data of NA3, published as detailed numerical tables [Bad 84]. The agreement in the mass region from 4.5 to 8.5 GeV is very good, as long as PYTHIA's distribution is multiplied by the K-factor, found to be 2.1 ± 0.3 (independent of the mass).

4.2 Acceptances

The acceptance of the detector was calculated for each (signal) process and each data set. This was done by following the generated events through the detector simulation program and writting them in 'Monte Carlo' DST's, that are then processed with the same reconstruction procedure as the one applied to the experimental data. The acceptance is defined to be the ratio between the number of events accepted by the detector's simulation–reconstruction chain and the number of generated events, in the same (restricted) phase space domain. The left-side of figure 4.3 displays the detector's acceptance, in the SU 91 Phi and SU 91 Psi configurations, for Drell–Yan dimuons, as a function of their mass. The effect of the 80 cm of Iron in the 'dump' hadron absorber is clearly visible in this figure, deteriorating the acceptance in the lower region of the mass spectra in the case of the SU 91 Psi setup.

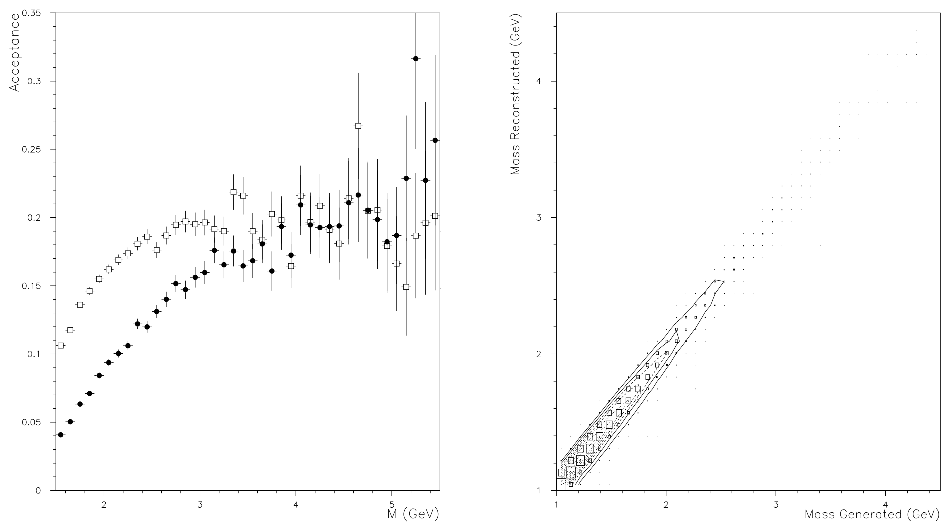

Figure 4.3: Left: Differential mass acceptance for the Drell–Yan process in the SU 91 Phi (open squares) and SU 91 Psi (closed circles) setups. Right: Illustration of the smearing effect in the mass variable (using Drell–Yan dimuons in the SU 91 Phi setup).

It is important to realise that the finite resolution of the detector induces changes (smearing) in the values of the kinematical variables. This means that the events will be accepted with (slightly) different kinematics from those at the generation level (see right-side of figure 4.3). Some events generated outside of the acceptance window will be 'smeared' into it (and vice-versa). That is why, in order to correctly evaluate the detector's acceptance in some given region of phase space, it is necessary to generate events in a bigger region. For the kinematical window chosen in the present work (see section 3.3), we have generated events with mass above 1.0 GeV and rapidity between 2.8 and 4.1, no restrictions being used in the p_{T} or $\cos(\theta)$ variables. We should emphasize that the calculation of the number of events accepted in our kinematical window is done using the 'reconstructed' variables, while the number of events generated in the same phase space region (and accepted or not) is calculated using the 'generation' variables.

The differential acceptances in p_{T}, y and $\cos(\theta)$, are presented in figure 4.4, for the J/ψ, ψ', Drell–Yan and $\mathrm{D\bar{D}}$ processes, in the case of the SU 91 Phi setup. This figure strongly suggests that the J/ψ and ψ' resonances have very similar

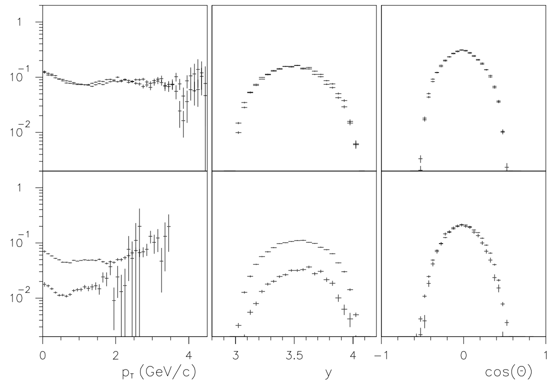

p_T (GeV)	3–3.1	3.1–3.2	3.2–3.3	3.3–3.4	3.4–3.5	3.5–3.6	3.6–3.7	3.7–3.8	3.8–3.9	3.9–4
3.5–4	3	10	11	15	20	31	12	7		15
3–3.5	11	20	20	22	20	19	20	15	17	8
2.5–3	4	15	23	27	26	23	13	10	11	7
2–2.5	5	17	24	30	31	32	23	17	9	6
1.5–2	4	13	22	29	32	31	28	20	11	5
1–1.5	3	11	19	24	28	26	25	18	11	4
0.5–1	3	11	17	25	29	29	28	20	12	4
0–0.5	3	11	22	30	39	42	37	25	18	8

Figure 4.4: Left: p_{T}, y and $\cos(\theta)$ acceptances, in the SU 91 Phi setup, for the J/ψ and ψ' resonances (top) and for the Drell–Yan and $\mathrm{D\bar{D}}$ processes (bottom). Right: Table of J/ψ acceptance (in %) in y and p_{T} cells, for the SU 91 Phi setup.

acceptances, both in absolute terms and in shape, while the $\mathrm{D\bar{D}}$ and Drell–Yan processes are seen by the detector in a substantially different way.

Since we will be interested in relative comparisons between the several processes, it is useful to compare the shape of their differential acceptances. This is done in figure 4.5, where the ratios of acceptances are displayed, in the three kinematical variables, for ψ'/ψ, ψ/DY and $\mathrm{D\bar{D}}/\mathrm{DY}$. Except for some points at the borders of the domains we have chosen, all the processes have similar acceptance *shapes*.

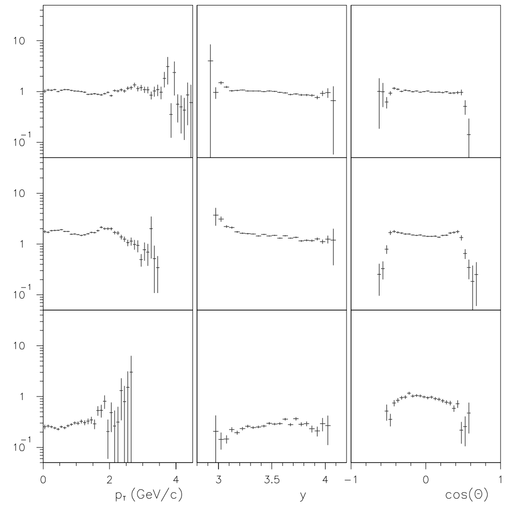

Figure 4.5: Ratios of differential acceptances, in the SU 91 Phi setup, for ψ'/ψ (top), ψ/DY (middle) and $\mathrm{D\bar{D}}/\mathrm{DY}$ (bottom).

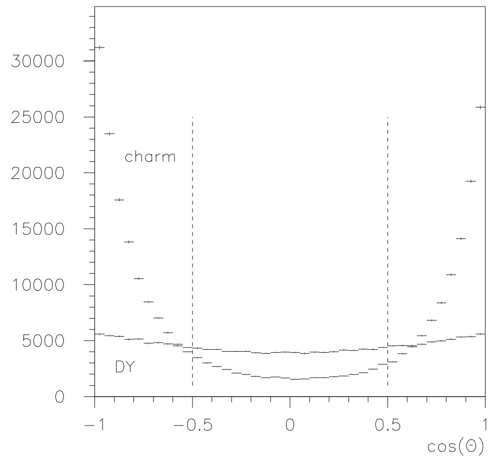

Figure 4.6: Distributions in $\cos(\theta)$ for the Drell–Yan and charm processes.

The integrated values of the acceptances, in the restricted kinematical domain chosen for the analysis, are $A^{J/\psi} = 19.8\,\%$, $A^{\psi'} = 20.5\,\%$, $A^{\mathrm{DY}} = 15.0\,\%$ and $A^{D\bar{D}} = 11.9\,\%$, for all data sets except SU 91 Psi, whose corresponding values are $A^{J/\psi} = 15.7\,\%$, $A^{\psi'} = 17.4\,\%$, $A^{\mathrm{DY}} = 8.5\,\%$ and $A^{D\bar{D}} = 5.0\,\%$.

The difference between the charm and Drell–Yan acceptances is mainly due to their different distributions in the $\cos(\theta)$ variable, as is shown in figure 4.6.

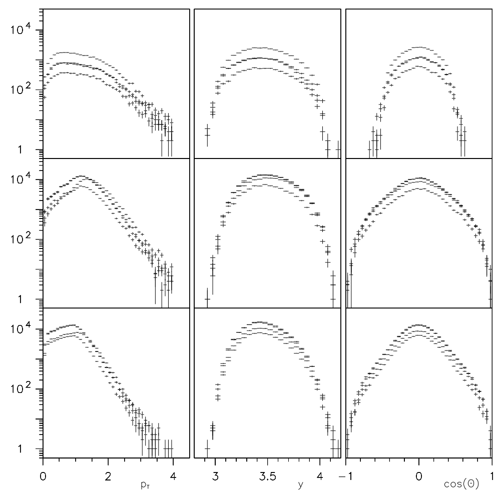

Figure 4.7: p_{T}, y and $\cos(\theta)$ distributions, as collected by the four S–U setups, for three types of events: 'J/ψ' (top), 'continuum' (middle) and 'like-sign' (bottom).

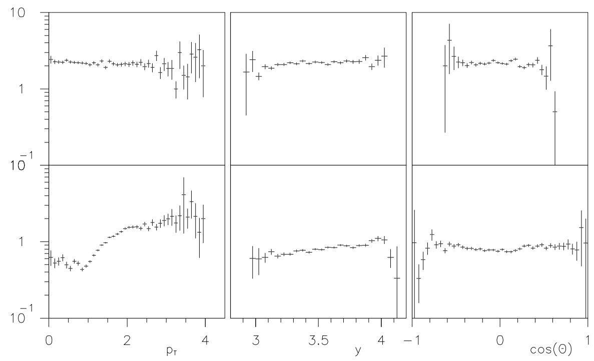

Figure 4.8: Ratio of p_{T}, y and $\cos(\theta)$ distributions, for the 'J/ψ' (top) and 'continuum' (bottom) mass ranges, between the SU 91 Psi and the SU 90 St data sets. The effect of the 80 cm of iron in cutting the low p_{T} and low mass muon pairs is clearly visible.

Since the several data sets were taken with different experimental setups it is clear that they can have different acceptances. For the same reason, the *measured* kinematical distributions have different shapes. This can be seen in figure 4.7, where the p_{T}, y and $\cos(\theta)$ distributions are presented, for the four S–U data sets. The three rows correspond to 'the J/ψ' (signal events with mass between 2.7 and 3.5 GeV — top row), 'the continuum' (signal events with mass between 1.5 and 2.5 GeV — middle row), and 'the background' (like-sign events with mass between 1.5 and 2.5 GeV — bottom row).

To better illustrate the differences between the distortions introduced by the several setups on the shapes of the kinematical distributions, figure 4.8 presents the ratio of these distributions, between the SU 91 Psi and the SU 90 St data sets (the other setups are very similar to the SU 90 St).

4.3 Functional forms representing the signal contributions

We want to compare the measured mass spectra to a superposition of the known physical processes, to investigate their relative normalizations and to search for any discrepancy between the observations and the expectations. This implies a good understanding of the line shape of each contribution.

From the Monte Carlo simulation (event generation and reconstruction) of the four considered 'signal' processes, we get the corresponding mass distributions, in the 'reconstructed' variable, presumably as they appear in the measured mass spectra. These histograms are then fitted by functional forms, selected empirically to provide a good agreement with the simulated line shapes. This way we smooth away the statistical fluctuations, imposed by the computer time required by the simulations. In the following we give the details of this procedure.

4.3.1 The J/ψ line shape

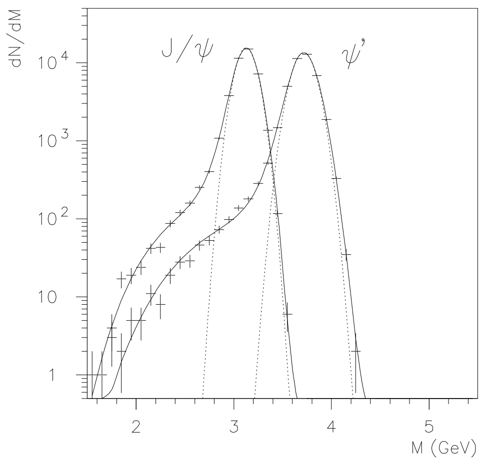

Figure 4.9: J/ψ and ψ' shapes, as simulated for the SU 91 Phi data set.

The J/ψ and ψ' resonances are well represented (see figure 4.9) by a functional form, $R(m)$, that can be described as a gaussian whose standard deviation, σ, increases as we move away from the center of the peak, μ:

$$R(m) = \exp\{-\frac{(m-\mu)^2}{2\,\sigma^2}\} \; ,$$

$$\sigma = \begin{cases} \sigma_0 & \text{if} \quad 0.98\mu < m < 1.02\mu \; , \\ \sigma_0\,[1 + (r_1\,\delta_l)^{(r_2 - r_3\,\delta_l)}] & \text{if} \quad \delta_l \equiv 0.98\mu - m > 0 \; , \\ \sigma_0\,[1 + r_4\,\delta_r] & \text{if} \quad \delta_r \equiv m - 1.02\mu > 0 \; . \end{cases} \tag{4.1}$$

The six parameters $(\mu, \sigma_0, r_1, \ldots, r_4)$, are determined from a fit to the Monte Carlo distributions, for each resonance and each data set.

The very large sample of collected J/ψ events and the sensitivity of the ψ' normalization to the J/ψ line shape, imposes the use of the (complicated) form $R(m)$ rather than a simple gaussian reflecting the mass resolution of the spectrometer. To get a better agreement between the J/ψ shape obtained by Monte Carlo and the collected data, some slight adjustments on μ and σ_0 were found to be necessary, revealing the approximate nature of the simulation. For instance, the multiple scattering was treated as purely gaussian distributed, which is a reasonable approximation for small deflection angles induced by a single material, but is systematically too small in our case. Other minor effects exist, such as slight differences between the actual properties or dimensions of the materials used in the experimental setups and their parametrization in the simulation, some fluctuations on the energy loss the muons suffer while crossing the hadron absorbers and the dispersion of the sub-targets along the beam direction.

To adjust the μ and σ_0 parameters of the J/ψ simulated shapes, we have started by fitting a gaussian to the experimental 'signal' mass spectra, between 2.9 and 3.3 GeV, obtaining the mean and standard deviation values: $\mu_{\rm Exp}$ and $\sigma_{\rm Exp}$. Then we have done the same fit to the simulated J/ψ mass spectra, extracting the corresponding mean and standard deviation values: $\mu_{\rm Sim}$ and $\sigma_{\rm Sim}$.

The ratio between the values obtained from the fit to the experimental data and from the fit to the simulated data (presented in table 4.4), provides the scale to correct the parameters $\mu^{J/\psi}$ and $\sigma_0^{J/\psi}$, therefore getting the simulated J/ψ shape in better agreement with the collected data:

$$\mu^{J/\psi} = \mu^{J/\psi}\Big|_{MC} \times \frac{\mu_{\rm Exp}}{\mu_{\rm Sim}} \quad , \tag{4.2}$$

$$\sigma_0^{J/\psi} = \sigma_0^{J/\psi}\Big|_{MC} \times \frac{\sigma_{\rm Exp}}{\sigma_{\rm Sim}} \; . \tag{4.3}$$

Data set	$\mu_{\rm Exp}$	$\mu_{\rm Sim}$	$\mu_{\rm Exp}$ / $\mu_{\rm Sim}$	$\sigma_{\rm Exp}$	$\sigma_{\rm Sim}$	$\sigma_{\rm Exp}$ / $\sigma_{\rm Sim}$
pW 88 V	3.162	3.150	1.0038	0.1296	0.1010	1.283
pW 88 D	3.151	3.138	1.0039	0.1315	0.1070	1.229
pU 87	3.097	3.118	0.9931	0.1386	0.1184	1.171
pU 88	3.094	3.119	0.9919	0.1401	0.1160	1.208
SU 90 St	3.112	3.123	0.9966	0.1422	0.1252	1.136
SU 90 Al	3.133	3.125	1.0027	0.1246	0.1037	1.202
SU 91 Phi	3.091	3.124	0.9896	0.1240	0.1032	1.202
SU 91 Psi	3.087	3.125	0.9880	0.1472	0.1319	1.116

Table 4.4: μ and σ values (in GeV) obtained by fitting a gaussian to the J/ψ peak in both the experimental and simulated mass spectra.

Although these are small changes, they must be taken into account since a discrepancy in the reproduction of the J/ψ shape might induce an incorrect adjustment of the (less pronounced, therefore more sensitive) ψ' contribution.

For the studies of the mass region above 3 GeV, as will be shown in the next chapter, these corrections to the Monte Carlo J/ψ line shape provide a reasonable agreement with the measured distributions. However, a simple increase of the σ_0 parameter, of equation 4.1, while providing a good matching of the region around and above the J/ψ peak, induces a discrepancy in the preceding mass bins. We can keep the same analytical function by tunning the r_1 parameter. The basic idea is that the Monte Carlo simulation has a wrong (too simple) description of the multiple scattering, mechanism responsible for the width of the (central) shape, but has a reasonable description of the energy loss process, responsible for the low mass tail. Therefore, we should prevent the increase in σ_0 from changing the analytical parametrization of the 'energy loss' tail. We can achieve this, without introducing more parameters, dividing r_1 by the same amount that multiplies σ_0. This procedure provides a reasonable description of the 'left side' of the J/ψ peak, allowing the analysis of the mass 'continuum' below 2.5 GeV to be safely done. Notice that we have chosen the mass range between 1.5 and 2.5 GeV to study the IMR 'continuum' in order to be (as much as possible) insensitive to the resonances.

4.3.2 The ψ' line shape

In principle, the ψ' shape resulting from the Monte Carlo simulation must also be corrected in much the same way as done for the J/ψ. If the approximations used in the simulation affect both resonances in the same way, we can expect that the correction deduced from the J/ψ peak should also be applied to the ψ' shape. This assumption is based on the fact that the computer simulation is basically the same for both resonances. Afterall, the shape of the resonances is essentialy related to the changes ('biases') induced by the detector, which are determined by some physics processes (like the muon energy loss and the multiple scattering) and the description of the setup geometry and material properties. Under this hypothesis, the new μ and σ_0 values of the ψ' would be:

$$\mu^{\psi'} = \mu^{\psi'}\Big|_{MC} \times \frac{\mu_{\text{Exp}}}{\mu_{\text{Sim}}}\Big|_{J/\psi} \quad , \tag{4.4}$$

$$\sigma_0^{\psi'} = \sigma_0^{\psi'}\Big|_{MC} \times \frac{\sigma_{\text{Exp}}}{\sigma_{\text{Sim}}}\Big|_{J/\psi} \quad . \tag{4.5}$$

Actually, the ψ' shape obtained in this way does not provide the best possible fit of the data. The width of the shape (corrected using equation 4.5) seems to be correct but a higher $\mu^{\psi'}$ would give a better matching with the data points.

If we find that a slight translation of the J/ψ Monte Carlo shape should be done to get a better fit, the same should be done to the ψ'. An alternative way of doing it is to take the 'corrected' $\mu^{J/\psi}$ and multiply it by the ratio of the resonance masses, as taken from the PDG tables,

$$\mu^{\psi'} = \mu^{J/\psi} \times \frac{m_{\psi'}}{m_{J/\psi}}\Big|_{PDG} \quad . \tag{4.6}$$

This procedure completly neglects the ψ' simulation in what concerns the $\mu^{\psi'}$ value. Anyway, it gives similar (unsatisfying) matching with the data points.

If we take the Monte Carlo ψ' shape, without applying any correction to $\mu^{\psi'}$, we get a closer agreement with the data, in most of the data sets. The exceptions are the pW 88 D and the SU 90 St data sets, where a corrective factor of 1.01 allows a better fit. This procedure of correcting $\mu^{\psi'}$ and $\mu^{J/\psi}$ independent of each other (while $\sigma_0^{\psi'}$ is 'properly' corrected by equation 4.5), although not very satisfying, provides the best agreement with the data and is, therefore, adopted.

The ratio ψ'/ψ remains virtually insensitive to such (small) translations of the ψ' shape, typical changes being about 10 times smaller than the statistical error bar. The corresponding values of the reduced χ^2, however, express a considerable improvement in the fit quality (decreasing by $\sim 30\,\%$).

A good description of the resonances line shapes is particularly important in the case of the S–U data sets, where the same mass fit will be performed on 4 event sub-samples (the 4 E_T bins). We prefer to start by reaching a good matching between the signal input shapes and the 'all E_T' mass distribution, so that the E_T dependence of the results is not (too much) affected by the bigger statistical fluctuations of the sub-samples.

4.3.3 The Drell–Yan and D$\bar{\mathrm{D}}$ mass spectra

In the case of the SU 91 Psi data set, the Drell–Yan and D$\bar{\mathrm{D}}$ components of the mass spectra were found to be well described by exponential functions in the high mass region, while an attenuation factor is required for mass values below 2.5 GeV, to account for the drop in acceptance,

$$C(m) = \mathrm{e}^{-m/c_1} \cdot (1 - c_2 \cdot \mathrm{e}^{-m/c_3})\,. \tag{4.7}$$

Figure 4.10 shows the simulated (generated and reconstructed) Drell–Yan and D$\bar{\mathrm{D}}$ dimuon mass distributions for this setup. The superimposed lines are the result of fitting the data points to the functional just refered, the values of the parameters being $c_1 = 0.732$, $c_2 = 14.6$ and $c_3 = 0.45$ for Drell–Yan and $c_1 = 0.305$, $c_2 = 12.7$ and $c_3 = 0.52$ for D$\bar{\mathrm{D}}$.

The Monte Carlo Drell–Yan and D$\bar{\mathrm{D}}$ mass distributions reconstructed for the other setups are presented in figure 4.11. While in the case of charm we have added together the 7 distributions, since they were found to be perfectly superposable, for Drell–Yan we have merged the 4 p–A and the 3 S–U distributions in two different histograms, to account for the isospin differences. Equation 4.7 does not provide a very good fit to the lower end of the mass distributions displayed in this figure. Since this region does not suffer from statistical fluctuations, instead of looking for some other more complicated empirical function, we can use the data points directly in the definition of these Drell–Yan and D$\bar{\mathrm{D}}$ shapes. The mass region

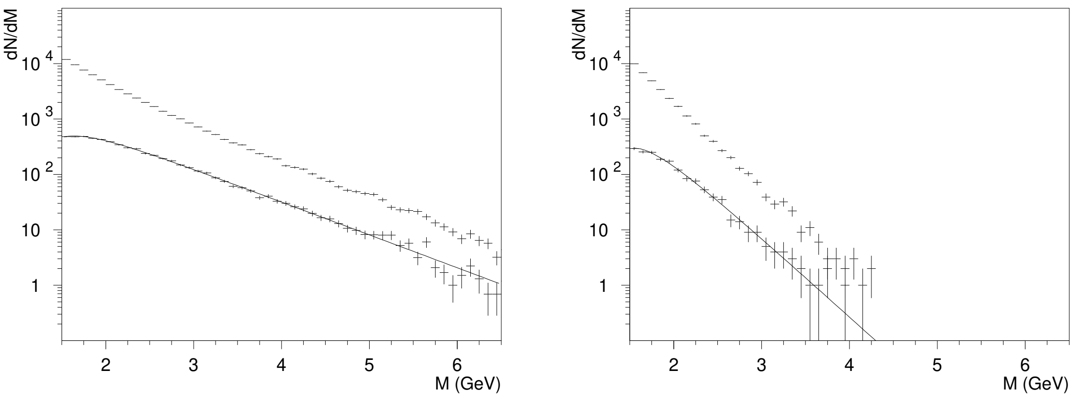

Figure 4.10: Shapes of the simulated (generated above and reconstructed below) Drell–Yan (left) and D$\bar{\mathrm{D}}$ (right) mass distributions, as they appear in the SU 91 Psi data set.

above 2.5 GeV is perfectly exponential, with (inverse) slope 0.302 for D$\bar{\mathrm{D}}$ and 0.716 (0.681) for Drell–Yan in the p–A (S–U) data sets.

The importance of the isospin dependence of Drell–Yan production can be appreciated in figure 4.12 a, where the ratio between the S–U and p–A mass distributions, at the generation level, is displayed. Figure 4.12 b shows the same ratio at the reconstructed level (SU 91 Psi data set excluded). The straight lines superimposed on the data points are the result of a linear fit and help to show that the slopes of the Drell–Yan distributions are indeed quite different from the p–A to the S–U data.

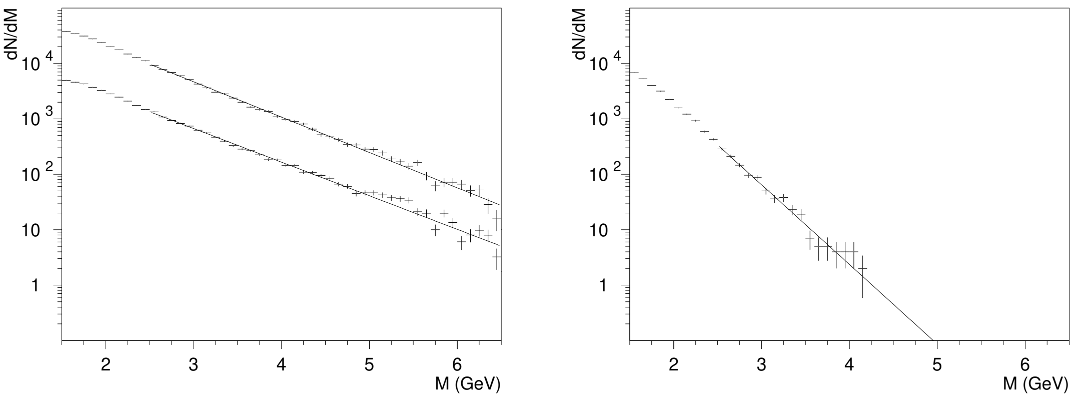

Figure 4.11: Drell–Yan (left) and D$\bar{\mathrm{D}}$ (right) mass distributions, as reconstructed in the p–A and S–U data sets (SU 91 Psi excepted).

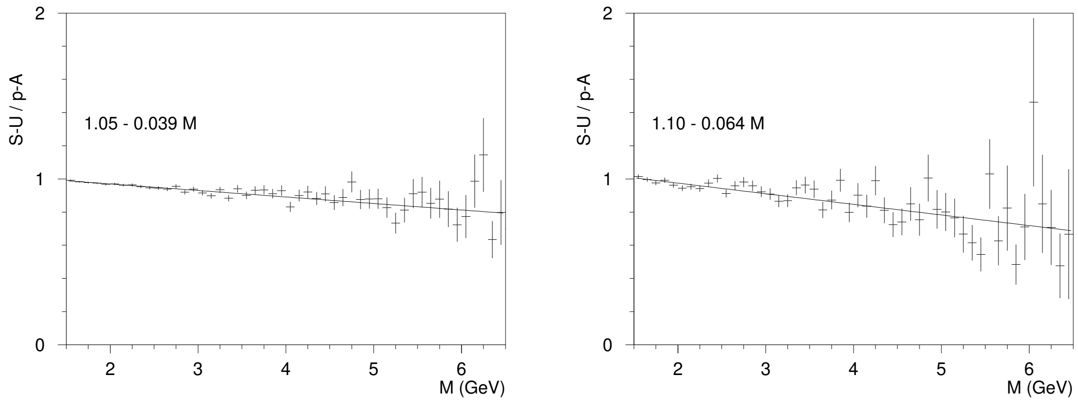

Figure 4.12: Ratio between the Drell–Yan mass distributions simulated for the S–U and p–A data sets, at the generated (left) and reconstructed (right) levels.

4.4 Combinatorial Background

By far the most important contribution to the 'opposite sign' intermediate mass continuum, measured in heavy ion collisions, is the background from the uncorrelated decays of π and K mesons (see figure 4.13). Furthermore, the combinatorial nature of this process makes it particularly dangerous in the search for 'thermal dimuons', since both these processes have the same (quadratic) multiplicity dependence. Therefore, a detailed understanding of the background subtraction procedure is essential in the study of the intermediate mass region.

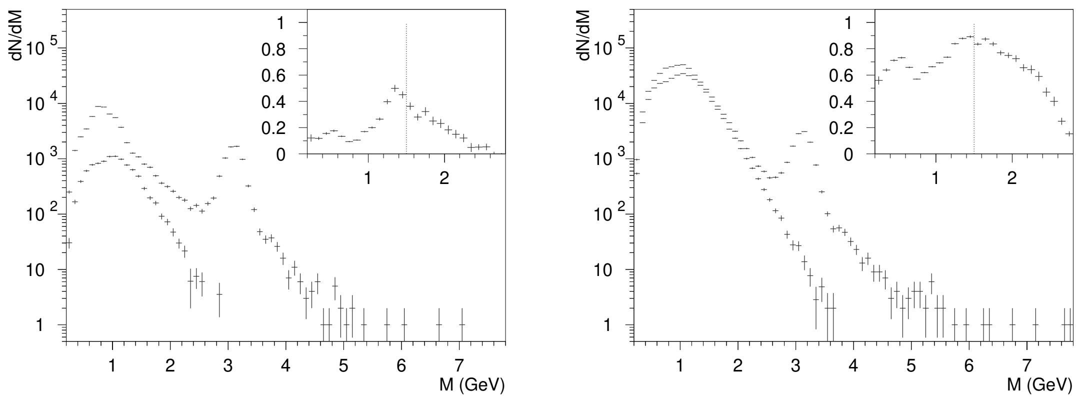

Figure 4.13: Opposite-sign and background dimuon mass distributions from the pU 87 (left) and SU 90 St (right) data sets. The inserts display the corresponding ratio 'background over opposite-sign'.

In the present study we consider as background the processes that contribute both to the opposite-sign *and* to the like-sign distributions. For instance, the muon pairs originated from the (semi-leptonic) decays of charm mesons are considered as a 'signal' process since a $c\bar{c}$ pair produced in a collision might originate an opposite-sign muon pair but not a like-sign pair. Of course, when only one of the muons comes from a D meson, the other coming from a π or a K, then both opposite-sign and like-sign events will be produced, therefore being considered as a background contribution. The same happens when a muon comes from the decay of a J/ψ but not the other.

While the 'signal' processes give rise to prompt muons, basically produced at the interaction vertex, the 'background' muon pairs result from the in-flight decay of π and K mesons, usually some cm downstream from the target. Therefore, the fraction of triggers corresponding to background events is strongly affected by the amount and absorption properties of the materials placed between the target and the muon spectrometer. This is illustrated in figure 4.14, where the ratio 'background over opposite-sign' is plotted for the two p–W setups, as well as for the SU 90 St and SU 91 Psi setups.

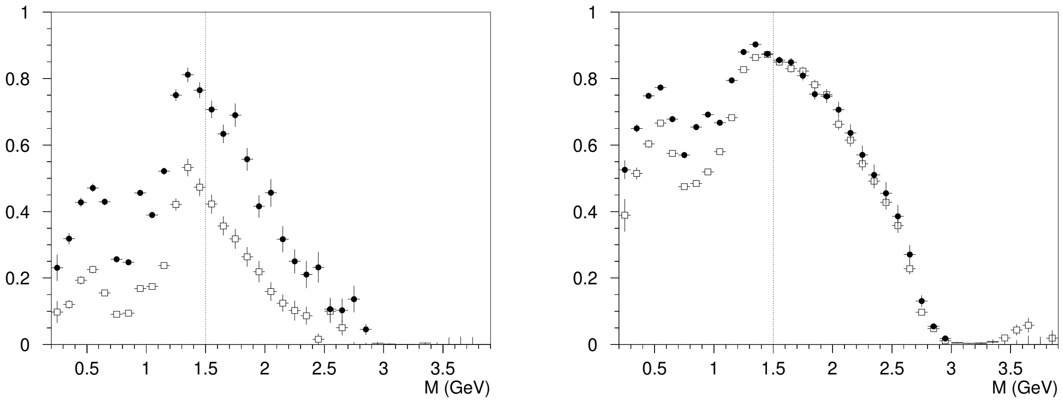

Figure 4.14: Ratio 'background over opposite-sign' for p–W (left) and S–U (right) data sets: closed circles for pW 88 V and SU 90 St; open squares for pW 88 D and SU 91 Psi.

The combinatorial background in the opposite-sign mass spectra can be estimated by the following expression [Var 87, Lou 89], the subscript indicating the sign of the spectrometer's magnetic field:

$$\frac{\mathrm{d}N^{\,\mathrm{Bg}}}{\mathrm{d}M} = 2 \cdot R^{\mathrm{Bg}} \cdot \left\{ \sqrt{\left.\frac{\mathrm{d}N}{\mathrm{d}M}\right|_{\oplus}^{++} \cdot \left.\frac{\mathrm{d}N}{\mathrm{d}M}\right|_{\oplus}^{--}} + \sqrt{\left.\frac{\mathrm{d}N}{\mathrm{d}M}\right|_{\ominus}^{++} \cdot \left.\frac{\mathrm{d}N}{\mathrm{d}M}\right|_{\ominus}^{--}} \right\}, \qquad (4.8)$$

The like-sign functions of the right side (exponentials for all the data sets except SU 91 Psi) are previously fitted to the corresponding measured mass spectra. Clearly, these fits are done for each E_{T} bin, in the case of the S–U data analysis.

The value of the R^{Bg} factor depends on the number of *accepted* positive and negative muons. Therefore, it depends on eventual acceptance (trigger) biases and on the multiplicity (or E_{T}) of the collision. R^{Bg} is expected to be 1 *if* the parent π and K mesons are (charge) uncorrelated, have poissonian multiplicity distributions and there are no acceptance bias.

Charge decorrelation means that the probability to have an event with N^+ positive mesons and N^- negative mesons, $p(N^+, N^-)$, is equal to the product $p(N^+) \cdot p(N^-)$. Then, the number of $+-$ muon pairs (from mesons decay) can be written as

$$N^{+-} = < N^+ > \cdot < N^- > \cdot A^{+-} \,, \tag{4.9}$$

the corresponding number of like-sign muon pairs being

$$\begin{cases} N^{++} = [< {N^+}^2 > - < N^+ >] \cdot \frac{A^{++}}{2} & , \\ N^{--} = [< {N^-}^2 > - < N^- >] \cdot \frac{A^{--}}{2} & . \end{cases} \tag{4.10}$$

If the multiplicity distributions of the mesons are poissonian,

$$< N^2 > - < N >^2 = < N > \,, \tag{4.11}$$

we get

$$N^{+-} = 2 \cdot \sqrt{N^{++} \cdot N^{--}} \cdot \frac{A^{+-}}{\sqrt{A^{++} \cdot A^{--}}} \,. \tag{4.12}$$

The 'image cut' (see equation 3.6 on page 53), used in the NA38 experiment, makes sure that the detector (trigger) treats in the same way all the muon pairs, irrespective of their charges. Therefore, the ratio of acceptances in equation 4.12 does not contribute to the R^{Bg} factor. This is not the case, for instance, in the HELIOS-3 experiment, whose trigger system makes it more probable to accept an opposite-sign event than a like-sign event. This is why the R^{Bg} factor, for high multiplicity events, is estimated to be 1.09 in HELIOS-3, while it is taken as 1 in NA38.

In low multiplicity events, like those produced in p–A collisions, the probability to have a certain (small) number of positive mesons is certainly much more correlated to the corresponding probability of negative mesons. For instance, in a p–p collision, charge conservation implies that there must be two more positive than negative particles in the final state. Another example of a correlation induced by physics (not by the detector) is associated K production. Since there are no valence antiquarks in proton (or nucleus) induced collisions, it is possible to produce positive kaons associated to Λ particles, while the K^- can only be produced together with K^+. The existence of such correlations is responsible for a bigger R^{Bg} factor. For instance, the HELIOS-3 collaboration uses R^{Bg}=1.57 in p–W collisions [Lon 94].

As will be seen in the next chapter, the p–A value of R^{Bg} appropriate for the NA38 experiment can be extracted from the experimentally measured p–W data, by comparing the mass spectra of the two setups, very different in what concerns their hadron absorption properties (see figure 3.1). While the 'signal' cross sections must be the same in both data sets, the amount of background from π and K decays is higher in the setup with shorter hadron absorber.

Reversing both the muons' charge and the polarity of the magnetic field should be equivalent to not doing any change. This means that the same functional form should provide a good description of both spectral shapes. Therefore, the free parameters in the *simultaneous* fit to the 4 combinations of dimuons 'charge' times magnetic field polarity are the 4 normalizations and two 'slopes' (for the 'convergent' and 'divergent' configurations):

$$\frac{\mathrm{d}N}{\mathrm{d}M} = \begin{cases} p_1 \ \exp\{-M/p_5\} & \text{if} \quad --\ \ominus\,, \\ p_2 \ \exp\{-M/p_6\} & \text{if} \quad ++\ \ominus\,, \\ p_3 \ \exp\{-M/p_6\} & \text{if} \quad --\ \oplus\,, \\ p_4 \ \exp\{-M/p_5\} & \text{if} \quad ++\ \oplus\,. \end{cases} \tag{4.13}$$

Figure 4.15 shows an example of such a fit. The 4 different windows visible in the figure correspond to the 4 charge combinations: $--\ \ominus$, $++\ \ominus$, $--\ \oplus$ and $++\ \oplus$.

In the case of the SU 91 Psi data set, due to its smaller acceptance for low mass values, the shape of the like-sign distributions is no longer a simple exponential, a sligth modification of the functional forms being required. Figure 4.16 shows that it is possible to have a good description of the data by replacing the exponentials

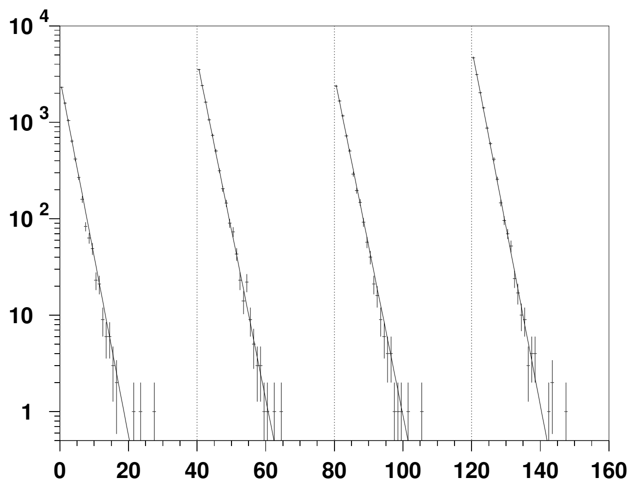

Figure 4.15: Fit of the like-sign mass spectra in the SU 91 Phi data set (all E_{T}). Each 40 channels map the mass region between 1.5 and 5.5 GeV.

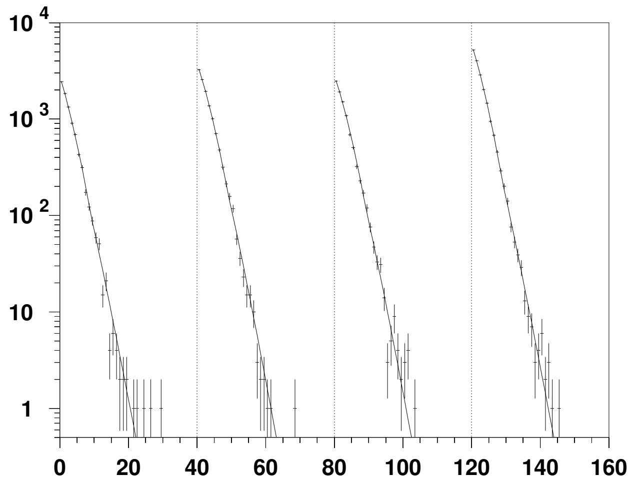

Figure 4.16: Same as previous figure but for the SU 91 Psi data set.

by:

$$\frac{\mathrm{d}N}{\mathrm{d}M} = \begin{cases} p_1 \ \exp\{-0.5 \ (M - p_5)^2/\sigma_1^2\} & \text{if} \quad - - \ \ominus \, , \\ p_2 \ \exp\{-0.5 \ (M - p_6)^2/\sigma_2^2\} & \text{if} \quad + + \ \ominus \, , \\ p_3 \ \exp\{-0.5 \ (M - p_6)^2/\sigma_2^2\} & \text{if} \quad - - \ \oplus \, , \\ p_4 \ \exp\{-0.5 \ (M - p_5)^2/\sigma_1^2\} & \text{if} \quad + + \ \oplus \, , \end{cases} \tag{4.14}$$

with

$$\sigma_1 = \begin{cases} p_7 & \text{if} \quad 2.4 < M \, , \\ p_7 \cdot \{1 + p_9 \ (M - 2.4)\} & \text{otherwise} \end{cases}$$

and

$$\sigma_2 = \begin{cases} p_8 & \text{if} \quad 2.4 < M \, , \\ p_8 \cdot \{1 + p_9 \ (M - 2.4)\} & \text{otherwise} \, . \end{cases}$$

Naturally, the description of the combinatorial meson decay contribution must be done together with the analysis of the signal processes (next chapter). Indeed, any selection cut or event binning (in E_{T}, for instance) must affect in just the same way the opposite-sign and like-sign samples.

It is interesting to get a feeling for the change in the amount of background events from p–A to S–U collisions and as a function of the setup used in the data taking (namely for the p–W data sets). We can get an idea of this evolution by using the ratio between the quantity of background events (estimated with equation 4.8, as explained above), in some mass window, and the number of J/ψ events,

Data set	$N^{J/\psi}$	$N^{\mathrm{Bg}}/N^{J/\psi}$	
		1.5–2.5	2.7–3.5
pW 88 V	7929	0.56 ± 0.011	—
pW 88 D	6971	0.16 ± 0.005	—
pU 87	6417	0.14 ± 0.005	—
pU 88	2108	0.16 ± 0.009	—
SU 90 St	11814	2.85 ± 0.03	0.018 ± 0.0012
SU 90 Al	5930	3.03 ± 0.05	0.020 ± 0.0018
SU 91 Phi	12877	2.84 ± 0.03	0.015 ± 0.0011
SU 91 Psi	28400	1.61 ± 0.01	0.014 ± 0.0007

Table 4.5: Ratios between the amount of background (integrated in two different mass regions) and J/ψ events.

estimated as the number of opposite-sign events minus the number of background events, in the mass region from 2.7 to 3.5 GeV. Table 4.5 contains the values of this ratio taking for the background the mass window from 1.5 to 2.5 GeV. Since this value is affected by the degradation of the low mass acceptance in the SU 91 Psi setup, the same ratio is also shown for the mass window used to estimate the number of J/ψ events.

Going from 1 to 32 incident nucleons, the number of background events increases about 18 times faster than the number of J/ψ events ($2.9/0.16 = 18$). If we parameterize this increase as A^{α}, and assume $\alpha_{\psi} = 0.92$, we get $\alpha_{\mathrm{Bg}} \sim 1.7$. Since the J/$\psi$ production is suppressed from proton to sulphur induced events, it is desirable to get an estimation of the background increase independent from the J/ψ. A good alternative to the (relative) normalization provided by the J/ψ, is the (absolute) normalization using the known luminosities (see section 3.2). Table 4.6 presents such a normalized background (using the values for the mass window 1.5–2.5 GeV). We see that the background increases by about a factor 400 from p–W to S–U collisions (using the most similar setups). Again, we interpret such an increase in terms of the power law in A, getting $\alpha_{\mathrm{Bg}} \sim 1.6$, in reasonable agreement with the previous estimation. Both normalization procedures lead to an increase by a factor ~ 3.4 when some 60 cm immediately down-stream from the target are

Data set	N^{Bg}	$\mathcal{L}$ (nb^{-1})	$N^{\mathrm{Bg}}/\mathcal{L}$
pW 88 V	4463	153	29.2
pW 88 D	1147	132	8.7
SU 90 St	33691	8.95	3764
SU 90 Al	17946	4.50	3988

Table 4.6: Ratios between the amount of background (in the 1.5–2.5 GeV mass region) and the integrated luminosity of the corresponding data set.

left empty.

References:

[Agu 88] M. Aguillar-Benitez *et al.,* Z. Phys. **C40** (1988) 321.
[Ald 90] D.M. Alde *et al.* (E772 Coll.), Phys. Rev. Lett. **64** (1990) 2479.
[Ama 91] P. Amaudruz *et al.* (NA37/NMC Coll.), Z. Phys. **C51** (1991) 387.
[Arn 94] M. Arneodo, Phys. Rep. **240** (1994) 301; CERN Preprint PPE/92-113.
[Bad 84] J. Badier *et al.* (NA3 Coll.), Z. Phys. **C26** (1984) 489.
[Cas 93] P. Castorina, A. Donachie and P. Harriman, Z. Phys. **C60** (1993) 135.
[Glü 92] M. Glück, E. Reya, A. Vogt, Z. Phys. **C53** (1992) 127.
[Lon 94] G. London, Proc. of the 'Workshop on Dilepton Production in Relativistic Heavy Ion Collisions', GSI, Darmstadt, Germany, 1994 (Ed. GSI), p. 130.
[Lou 89] C. Lourenço and J. Varela, "Methods of background estimation", NA38 Internal Note, November 1989.
[Plo 93] H. Plothow-Besch, Comp. Phys. Comm. **75** (1993) 396.
[Sjö 94] T. Sjöstrand, Comp. Phys. Comm. **82** (1994) 74.
[Var 87] J. Varela, "Soustraction du bruit de fond", NA38 Internal Note, December 1987.

Chapter 5

Data analysis of the high and intermediate mass regions

In this chapter we present the methods of analysis and the corresponding results concerning the high and intermediate mass regions of the dimuon spectra.

We start by a general discussion on the method used in the analysis, present the E_{T} distributions measured in S–U collisions and discuss the vertex efficiency correction.

Then we continue with the *relative* results on the HMR: the ratios ψ'/ψ and ψ/DY, in p–A versus S–U (integrated in E_{T}), and their evolution, as a function of E_{T}, in the S–U data.

The HMR analysis ends with the absolute cross–sections: the Drell–Yan K-factor and the J/ψ and ψ' production cross–sections times their branching ratio into muons.

The analysis of the IMR starts with the p–A data, including the *measurement* of the R^{Bg} factor and an estimation of the absolute cross–section for charm production. Then the S–U data is compared to the expected sources on the basis of the p–A results.

5.1 Alternative ways to study the signal

There are several ways of getting information on the 'signal' processes from the measured opposite-sign mass spectra.

5.1.1 Do not consider the background

The easiest way to deal with the combinatorial background polluting the opposite-sign mass spectra is just to ignore it ... This simple approach (the simplest of all) is not as dummy as it sounds, if we are only interested in the relative behaviour of the resonances. Indeed, it has even been used within the NA38 collaboration to study the relative behaviour of the ratio ψ'/ψ from p–U to S–U collisions and as a function of E_{T} [Ron 93]. Of course, it is completely useless if we are interested in understanding the physical origin of the signal events as a whole (resonances or not) or if we want to extract absolute cross-sections.

5.1.2 Get the signal directly

We can extract the 'signal' distribution by subtracting from the opposite-sign spectra an estimation of the background, based on the measured like-sign samples (using equation 4.8),

$$\frac{\mathrm{d}N}{\mathrm{d}M}^{\mathrm{Signal}} = \frac{\mathrm{d}N}{\mathrm{d}M}^{\mathrm{OS}} - \frac{\mathrm{d}N}{\mathrm{d}M}^{\mathrm{Bg}} . \tag{5.1}$$

Then, the analysis work is directly done on the signal distributions. This simple and direct method (used in NA38's first paper [Bag 89], for instance) is good enough to provide a first look into the data, but it has some problems that prevent its use in more accurate physics analysis. In particular, it destroys the poissonian nature of the data, since the difference between two Poisson distributions is no longer a Poisson distribution. Therefore, the fits to the 'signal' distribution cannot be done using the maximum likelihood method. On the other hand, the results obtained with the χ^2 method are not reliable when some of the bins have low statistics. Furthermore, this direct subtraction procedure gives a biased (overestimated) 'signal', since bins with zero events in the $--$ sample but *not* in the $++$ sample (or vice-versa) give zero background. At least, the like-sign distributions must be 'smoothed' before being used in the subtraction procedure. This is particularly bad when the subtraction is not performed in one single kinematical variable but in multidimensional cells, as must be the case since the background over signal changes as a function of the interaction sub-target, p_{T}, polar angle of the muons, etc. Also, the direct use of equation 4.8 requires the *a priori* knowledge of the R^{Bg} value.

5.1.3 Simultaneous fit of opposite-sign and like-sign distributions

This method has two steps. First, we find some functional forms that give a good description of the measured $++$ and $--$ mass spectra. Then we make a *simultaneous* fit of the *five* measured distributions: $+-$, $--\ominus$, $++\ominus$, $--\oplus$ and $++\oplus$. This method was used in the studies of J/ψ production conducted on the data collected before 1990 [Bag 91a,b], where exponentials give a good description of the like-sign mass spectra (see section 4.4). In this case, the opposite-sign distribution is fitted to

$$\frac{\mathrm{d}N^{+-}}{\mathrm{d}M} = \frac{\mathrm{d}N^{\,\mathrm{Sinal}}}{\mathrm{d}M} + 2 \times R^{\mathrm{Bg}} \times \left\{ \sqrt{p_1 \;\exp\left\{-M/p_5\right\} \times p_2 \;\exp\left\{-M/p_6\right\}} \right.$$
$$\left. + \sqrt{p_3 \;\exp\left\{-M/p_6\right\} \times p_4 \;\exp\left\{-M/p_5\right\}} \right\}, \quad (5.2)$$

with R^{Bg} set to 1.0 or to 1.25 (for example) depending on the reaction being S–U or p–A. To use this procedure in the SU 91 Psi data set the 6 free parameters used in the description of the background contribution must become 9, as was shown in section 4.4. To this number, the description of the 'signal' component adds, at least, 4 free parameters ...

If we want to make a simultaneous fit to *several data sets* (for example, to extract the R^{Bg} value, if the data sets have different enough hadron absorption properties) then it becomes impractical to do a simultaneous fit to the opposite-sign and like-sign distributions.

Besides the large number of parameters left free in the fit, this method includes the opposite-sign data, together with the like-sign, in the determination of the background contribution, making the background shape sensitive to the (unknown) signal description. For instance, a bad description of the J/ψ shape could lead to a distortion in the background curve. If we change our understanding of the 'signal' contributions (their functional descriptions) we might get a different background.

5.1.4 Consider the meson decays as a signal contribution

As will be shown later, we do not know the shapes of all the signal processes contributing to our (S–U) data. Therefore, we must fix the background shape exclusively on the basis of the like-sign spectra and prior to the fit to the opposite-sign distribution. In this alternative method, we start by making a simultaneous fit to the 4 like-sign mass spectra to set the analytical parametrization describing the background contribution (see section 4.4 on page 68). Then, we do the analysis of the opposite-sign distribution, considering the background contribution in exactly the same way as the signal ones, eventually leaving free its absolute normalization (to extract the R^{Bg} value) or imposing it *a priori*. This is the method used in the present work.

The same method can be applied with a background shape obtained by mixing muons from different like-sign events, instead of making a fit. Unfortunately, such alternative is very demanding in CPU time and it has its own problematic points. In particular, care must be taken when choosing the muons to be combined. Muons of different events are obviously uncorrelated but, for instance, we should not combine muons produced in different sub-targets or with very different values for the associated E_{T}.

5.2 E_{T} distributions and vertex efficiency correction in S–U collisions

In the present work, we are not interested in the study of the E_{T} distributions *de per se*. The E_{T} variable is used exclusively to tag the events as a function of the centrality of the collision. While in the case of p–A collisions all the events are treated together, the S–U events are distributed into 4 different classes, according to their E_{T} value, and the analysis of the dimuon mass distribution is done separately for each of these classes (and for the 'all E_{T}' class).

5.2.1 Differences between data sets

Since we want to combine events from several different S–U data sets, in the same E_{T} class, we must first make sure that the E_{T} variables from each setup are consistent with each other. Furthermore, if we want to extrapolate from the E_{T} measurement some estimation of the energy density achieved in the S–U collisions, also the absolute normalization of the E_{T} scale is of importance.

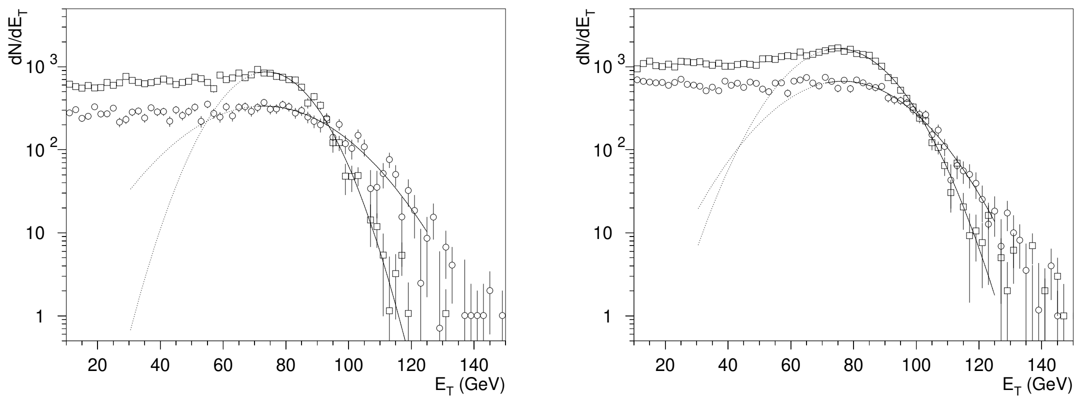

Figure 5.1: E_{T} distributions (corrected for ϵ_v) of the signal events with mass above 1.5 GeV, from the SU 90 (left) and SU 91 (right) data sets.

Two different electromagnetic calorimeters were used in the data taking with sulphur beams. One with 5 rings, covering the (pseudo) rapidity range from 1.7 to 4.1, and the other with only the 3 most external rings, outside of the muon spectrometer acceptance window. Therefore, the corresponding E_{T} distributions have different resolutions. This is clearly illustrated in figure 5.1, where we can see that the SU 90 Al and SU 91 Phi E_{T} distributions (circles) have broader tails than the SU 90 St and SU 91 Psi distributions (squares).

The scales of the E_{T} distributions were renormalized so that the mean values of the gaussians fitted to their 'knees' agree with each other. The absolute values of these scalling factors were determined by comparison with the $E_{\rm T}$ distribution of the S–U data collected in 1992, considered as being the one with better known absolute calibration. These 'renormalization' constants are: 0.82, 0.92, 0.88 and 0.87, for the SU 90 St, SU 90 Al, SU 91 Phi and SU 91 Psi data sets, respectively.

5.2.2 Definition of the 4 $E_{\rm T}$ classes

All the events with $E_{\rm T}$ (after renormalization) smaller than 10 GeV were rejected, since the identification of the interaction sub-target has a low efficiency ($\epsilon_v \lesssim 15\,\%$) for those very peripheral collisions, as was shown in figure 3.4, section 3.5.

The remaining events were distributed according to their $E_{\rm T}$ value in 4 bins, of low edge: 10, 39, 58 and 75 GeV. These border lines were determined so that the 4 bins of the SU 92 data set (the one with higher statistics) are equi-populated in signal events (of mass above 1.5 GeV). This allows to study the signal behaviour in 4 bins of roughly equal statistics. Since it is the *statistical error* on the number of signal (mainly J/ψ) events that we want to equilibrate between the 4 sub-samples, the partitions must be found prior to any weighting of the events. The correction of ϵ_v, which depends on the data set and is necessary to properly compare the several $E_{\rm T}$ distributions, does not change the borders of the (*statistically* equi-populated) bins, although it affects the mean $E_{\rm T}$ of each bin.

The binning found from the $E_{\rm T}$ distribution of a 'standard' data set will not provide the best possible equi-population of the event samples collected with a smaller calorimeter, because in this case the resolution in $E_{\rm T}$ is worst. But taking the same (absolute) $E_{\rm T}$ limits is the best way to ensure that we get the same fractions of the *physical* $E_{\rm T}$ distribution (or cross section) in each of the 4 bins, for all the different data sets. If bin number 4 of some data set would correspond to a different (physical) centrality range than the bin number 4 of another data set, then we would have to make a separate analysis for each data set, and we could not 'add' the results from both samples.

The $E_{\rm T}$ distributions of the several data sets (after correcting for their specific ϵ_v) should be comparable with each other (and provide an equally good estimation of the *true* distribution). In particular, the mean $E_{\rm T}$ values within each bin should be similar. As is shown in table 5.1, where these values are collected, the last bin clearly reflects the effect of the different $E_{\rm T}$ resolutions.

Data set	10–39	39–58	58–75	> 75
SU 90 St	25.1 (8.3)	48.7 (5.4)	66.8 (4.9)	83.9 (6.6)
SU 90 Al	24.8 (8.6)	48.5 (5.6)	66.7 (4.9)	90.1 (11.1)
SU 91 Phi	24.4 (8.2)	48.5 (5.5)	66.6 (4.9)	89.5 (11.0)
SU 91 Psi	24.9 (8.2)	49.0 (5.5)	66.9 (5.0)	85.9 (8.4)

Table 5.1: Mean values (and RMS) per $\Delta E_{\rm T}$ slice and data set, obtained from the signal $E_{\rm T}$ distribution (without any cut on the mass of the muon pair).

A final comment on the E_{T} binning. The population of the bins would be different if we wanted to get equal *relative error bars* on the ψ'/ψ ratio rather than equal number of signal events. Several reasons support the method chosen. First, we do not know *a priori* how to bin the data to get equal relative error bars on the ψ'/ψ ratio. That would require an iteractive, each time changing the E_{T} binning after seeing the ψ'/ψ values. Second, we are interested in studying the behaviour of all the processes contributing to the signal mass distribution. For example, the optimum binning to study the ratio 'data over known sources' in the intermediate mass continuum would probably be a different one. Third, besides the ratios, the *number* of events of each (signal) process, per E_{T} bin, are equally important (afterall, they are proportional to the absolute cross–sections).

5.2.3 Vertex efficiency correction in the mass distributions

We want to get absolute cross–sections for the production of the several signal processes that contribute to the mass distribution. Besides the luminosities, that only depend on the data set (see section 3.2), and the acceptances, that depend on the data set and on the process (see section 4.2), we need to correct for the efficiency of the algorithm that identifies the interaction sub-target, ϵ_v. Before starting the analysis of the mass distributions it is important to consider what is the best way to incorporate such a correction in the analysis procedure.

5.2.3.1 No correction at all

Clearly, the simplest way to deal with the ϵ_v correction is to ignore it. Again, this apparently absurd approach is not as silly as it sounds and it has been used in some analysis work done within NA38 (the same that neglects the combinatorial background 'complications'). If we are not interested in absolute cross–sections, if we only analyze one data set, if all the processes contributing to the mass distribution, including the J/ψ and ψ' but also the combinatorial background, (would) have the same correction, then (and only then) such an approach might be used. Of course, in the case of the present (somewhat more ambitious) analysis we must do something better.

5.2.3.2 Event per event correction

Since the vertex identification efficiency depends on E_{T}, a possible way to take it into account is to correct for it on a event by event basis, filling the mass histograms with a weight equal to the inverse of ϵ_v. This method of event per event correction has been generally used within NA38 but there are several problems associated with it.

One of the problems is that the weighting procedure spoils the poissonian nature of the mass spectra. *En tout rigueur*, this should prevent the use of the maximum likelihood method of fitting. This is usually considered as a tolerable lack of precision, as long as the mean weights per mass bin are close to unity. The 'minimum χ^2' method of fitting allows the use of a specially calculated set of (non-poissonian) errors, but this method should not be applied when low statistics bins are involved.

Even using a low E_{T} cut (set at 10 GeV), essentially defined on the basis of the maximum weight any single event is allowed to get ($\sim$ 6), it is possible to have important changes on the contents of some (very low statistics) mass bins. In the most extreme case, we can see the contents of some (high) mass bin being multiplied by $\sim$ 6, just because the only event it contains (before 'correction') happens to be associated with a low value of E_{T}. Clearly, this might affect the results of a fit to the mass spectra, in particular if the *shape* of the high mass distribution is to be determined from the data points.

The large value of the correction corresponding to the low E_{T} events leads to still another problem. Indeed, not only the shape of the mass distribution might change, also its integral is affected. Lets consider the events at the 'source' level. They will be produced associated to some E_{T} value and only a fraction $\epsilon_v(E_{\mathrm{T}})$ will be 'accepted' in the final sample of events. Integrating within each ΔE_{T} bin, leads to a mean efficiency given by

$$< \epsilon_v(\Delta E_{\mathrm{T}}) > = \int \frac{\mathrm{d}N}{\mathrm{d}E_{\mathrm{T}}}\ \epsilon_v(E_{\mathrm{T}})\ \mathrm{d}E_{\mathrm{T}} \Bigg/ \int \frac{\mathrm{d}N}{\mathrm{d}E_{\mathrm{T}}}\ \mathrm{d}E_{\mathrm{T}}\ . \tag{5.3}$$

Going in the other sense, from the accepted to the source level, we would expect a mean correction of $1/ < \epsilon_v >$ to be applied to the sample of events selected for the final analysis. Actually, an event by event correction leads to a different (and wrong) mean correction,

$$< 1/\epsilon_v(\Delta E_{\mathrm{T}}) > = \int \frac{\mathrm{d}N}{\mathrm{d}E_{\mathrm{T}}}\ \frac{1}{\epsilon_v(E_{\mathrm{T}})}\ \mathrm{d}E_{\mathrm{T}} \Bigg/ \int \frac{\mathrm{d}N}{\mathrm{d}E_{\mathrm{T}}}\ \mathrm{d}E_{\mathrm{T}}\ . \tag{5.4}$$

Clearly, this correction, $< 1/\epsilon_v(\Delta E_{\mathrm{T}}) >$, is not equivalent to the (correct) value, $1/ < \epsilon_v(\Delta E_{\mathrm{T}}) >$, the difference being quite important (some 16 %) in the lowest E_{T} bin, where $< \epsilon_v(\Delta E_{\mathrm{T}}) >$ is substantially lower than unity (see table 5.2). For the higher E_{T} bins it does not make any visible difference, $1/ < \epsilon_v(\Delta E_{\mathrm{T}}) >$ being equal to $< 1/\epsilon_v(\Delta E_{\mathrm{T}}) >$.

5.2.3.3 Check for some mass dependence

In this paragraph we want to address the following question: does ϵ_v depend on the (signal) process? If not, we should obtain the same value for the ψ'/ψ ratio, for instance, whether or not the ϵ_v correction is applied. We already know that there is a change in the relative production of J/ψ and Drell–Yan events, as a function

ΔE_{T} (GeV)	$< \epsilon_v >$ (%)	$1/ < \epsilon_v >$	$< 1/\epsilon_v >$
10–39	68.2	1.47	1.71
39–58	91.8	1.09	1.09
58–75	93.2	1.07	1.07
> 75	95.6	1.05	1.05

Table 5.2: Difference between the 'global' and the 'event by event' vertex efficiency correction methods. These (mean) values correspond to the opposite-sign events of mass greater than 3 GeV, collected in the SU 91 Psi.

of E_{T} (the famous 'J/ψ suppression'). We will see later in this chapter that the ψ' is also (even more) suppressed. Therefore, it is clear that the E_{T} distributions associated with these different processes do not have the same shape (otherwise their ratio would be flat). So, we would expect that the mean value of ϵ_v, defined by equation 5.3, would change its value when calculated in a mass range dominated, for instance, by J/ψ or by Drell–Yan events.

Actually, it turns out that changing the mass interval does not imply any visible difference in the ϵ_v value, as is shown in table 5.3. Most likely, the broad E_{T} bins used in this analysis smear out the differences between the distributions associated to the several dimuon mass ranges.

ΔE_{T} (GeV)	J/ψ	ψ'	DY
10–39	68.2	67.8	70.0
39–58	91.8	91.9	91.8
58–75	93.2	93.1	93.2
> 75	95.5	95.7	95.6

Table 5.3: Mean values of ϵ_v (in %) in three different mass ranges: 3.0–3.5 GeV (J/ψ); 3.5–4.1 GeV (ψ'); 4.1–5.5 GeV (DY). These values correspond to the opposite-sign events collected in the SU 91 Psi data set.

The stability of ϵ_v as a function of the mass is probably better appreciated by looking at figure 5.2, which displays the ratio between the *signal* mass distributions, in some ΔE_{T} bin, with and without (event per event) weighting, by the $1/\epsilon_v(E_{\mathrm{T}})$ correction,

$$1/\epsilon_v(M)\bigg|_{\Delta E_{\mathrm{T}}} = \int_{\Delta E_{\mathrm{T}}} \frac{\mathrm{d}^2 N}{\mathrm{d}M \mathrm{d}E_{\mathrm{T}}} \, \frac{1}{\epsilon_v(E_{\mathrm{T}})} \, \mathrm{d}E_{\mathrm{T}} \bigg/ \int_{\Delta E_{\mathrm{T}}} \frac{\mathrm{d}^2 N}{\mathrm{d}M \mathrm{d}E_{\mathrm{T}}} \, \mathrm{d}E_{\mathrm{T}} \, . \tag{5.5}$$

This figure is showing that, by selecting the events according to the mass of the dimuon, the *shape* of the E_{T} distribution, in 4 *large* bins, does not change by much. The vertex efficiency correction depends on the ΔE_{T} bin and on the data set, but we do not gain anything in applying the correction event by event.

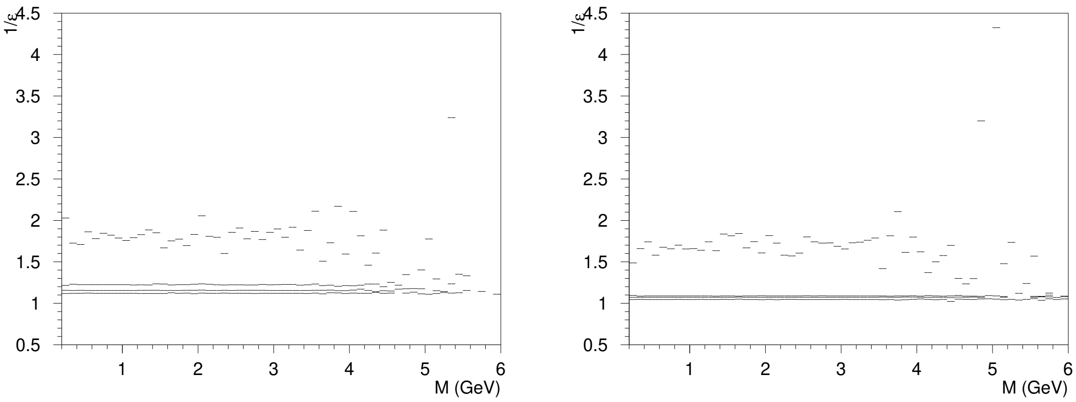

Figure 5.2: Ratio between the signal mass distribution corrected for the vertex efficiency and the same mass distribution without any correction, for the SU 90 St (left) and SU 91 Psi (right) data sets.

Multiplying the whole mass distribution by one single ('global') correction factor gives the same final result, without the problems (of too large 'correction' factors) clearly visible in figure 5.2, for the first E_T bin and the high mass region.

5.2.3.4 Global correction on the fitting functions

Since the ϵ_v correction does not depend on the dimuon mass, within a broad ΔE_T bin and a specific data set, the study of the *relative* contributions from the several processes to the mass spectra can be done directly on the measured mass distributions. But, in order to get absolute cross sections and also to combine in a single analysis step all the statistics (from the 4 S–U data sets) corresponding to a certain ΔE_T, we have to apply a global (per E_T bin and data set) correction.

Instead of applying a $1/\epsilon_v$ correction factor to the measured data, thereby destroying the poissonian nature of the distribution, it is better to apply an efficiency, ϵ_v, to the functions used to fit the data. In a way, this is equivalent to have the action of the (inefficient) vertex identification algorithm implemented in the Monte Carlo simulation program.

5.2.3.5 Like-sign versus opposite-sign correction

Besides the signal contributions, with shapes (and acceptances) derived by simulation, also the combinatorial (meson decay) background contributes to the measured opposite-sign mass distribution. Since the background spectra is derived (both in shape and in normalization) from the (also measured) like-sign data, no further corrections are needed to get it consistent with the opposite-sign spectra ('equally biased'). This would not be the case if the background contribution was derived by simulation.

Indeed, unlike what we just saw by comparing different *signal* processes, in the case of the like-sign events, their E_{T} distribution is sufficiently different from the one of the opposite-sign events to have visible effects on the ϵ_v values. The mean values of ϵ_v associated with opposite-sign and like-sign events of mass above 1.5 GeV, are presented in table 5.4, for the SU 91 Psi data set. We see that, in the lowest ΔE_{T} bin, the interaction sub-target recognition is 5 % more efficient for like-sign than for opposite-sign events, because of the difference in the corresponding mean E_{T} values.

ΔE_{T} (GeV)	$< \epsilon_v^{+-} >$	$< \epsilon_v^{\mathrm{Bg}} >$	$< \epsilon_v^{+-} > / < \epsilon_v^{\mathrm{Bg}} >$
10–39	70.0	73.5	0.95
39–58	91.8	91.9	1.00
58–75	93.2	93.2	1.00
> 75	95.6	95.6	1.00

Table 5.4: Mean values of ϵ_v (in %) for the opposite-sign and like-sign events collected in the SU 91 Psi data set (and their ratio).

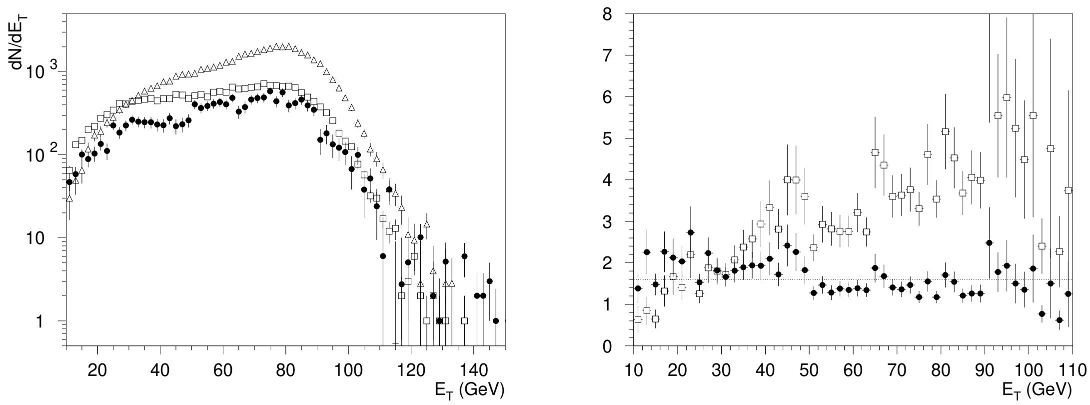

Figure 5.3: Left: E_{T} distributions (from the SU 91 Psi data set) associated with signal events in 1.5–2.5 GeV (circles) and 3.0–5.5 GeV (squares) and with background events in 1.5–2.5 GeV (triangles). Right: their ratios, "J/ψ over continuum" (circles) and "background over signal" (squares).

In order to further clarify this question, figure 5.3 compares the E_{T} distribution associated to 'signal' dimuons with mass values between 1.5 and 2.5 GeV ('continuum') with the same distribution but for events with mass above 3.0 GeV (essentially dominated by the J/ψ contribution). From the ratio of this two distributions (somewhat related to a "J/ψ relative to continuum suppression, as a function of E_{T}") we see a change in shape (the horizontal dotted line helps to guide the eye), but so slight that it does not influence the mean value of ϵ_v. The substantially different E_T distribution of the background dimuons (with mass values between 1.5 and 2.5 GeV) is also included in this figure. The ratio background to signal clearly shows an increase with E_T, revealing the quadratic multiplicity dependence of the *combinatorial* background to be compared with the (almost) linear dependence of the signal processes.

5.3 Relative results in the High Mass Region

In this section we will present the results concerning the high mass region that do not need the knowledge of absolute normalizations. This is the case, for instance, for the ratios of particle production, like the ψ'/ψ.

5.3.1 p–W, p–U and S–U (integrated in E_T)

In order to study the ψ' behaviour, we must have a good understanding of the 'continuum' on top of which it sits, since only around half of the events in its mass range are indeed ψ' events (due to the detector's mass resolution). While the high mass continuum is certainly well explained by the Drell–Yan process, for the mass values between the ϕ and the J/ψ we also have, at least, the contribution from the semi-leptonic decay of D$\bar{\mathrm{D}}$ pairs.

Since it is somewhat ambiguous to disentangle two 'continuous' contributions by means of a fit, we restrict the analysis of the HMR to the region above 3 GeV, for which the charm component can be safely neglected (it is certainly below 10 % of the Drell–Yan contribution, as will be shown later).

Therefore, we fit the measured (opposite-sign) dimuon mass distribution, in this high mass region, to a superposition of J/ψ, ψ' and Drell–Yan contributions, as symbolically expressed by

$$\frac{\mathrm{d}N^{+-}}{\mathrm{d}M} = < \epsilon_v^{+-} > \cdot \left\{ p_1\, A^{J/\psi}\, \frac{\mathrm{d}N^{J/\psi}}{\mathrm{d}M} + p_2\, A^{\psi'}\, \frac{\mathrm{d}N^{\psi'}}{\mathrm{d}M} + p_3\, A^{\mathrm{DY}}\, \frac{\mathrm{d}N^{\mathrm{DY}}}{\mathrm{d}M} \right\} + \frac{\mathrm{d}N^{\mathrm{Bg}}}{\mathrm{d}M} \quad . \tag{5.6}$$

The 'signal' shapes, previously normalized to unity in the mass window used to compute the acceptances (1.5–5.5 GeV), are multiplied by these acceptances, A, and by the *global* ϵ_v values, so that the fit (performed through the program MINUIT, using the maximum likelihood method) sets the p_1, p_2 and p_3 free parameters to the (corrected) absolute number of events of each process.

Since the mass region between 4.2 and 5.5 GeV is exclusively filled by Drell–Yan events and we are only fitting its normalization, this region is taken in the fit as a single point.

5.3.1.1 Results from each data set

We start by presenting the results of the fits done (independently to each data set. Since, for the moment, we are concentrating on *relative* results, we rewrite equation 5.6 to have as free parameters the *ratios* ψ'/ψ and ψ/DY (having the uninteresting normalization in the number of Drell–Yan events). Table 5.5 collects the obtained results, except for the (too low statistics) pU 88 and SU 90 Al data sets. As always, 'DY' refers to the mass region between 1.5 and 5.5 GeV, where the acceptances were computed. The two p–W, as well as the three S–U, data sets give compatible results, within the error bars.

Data set	ψ'/ψ (%)	ψ/DY	χ^2/ndf
pW 88 V	1.89±0.24	2.36±0.30	1.08
pW 88 D	1.70±0.24	2.82±0.45	0.45
pU 87	1.62±0.27	2.48±0.37	1.16
SU 90 St	1.05±0.19	1.92±0.21	0.73
SU 91 Phi	0.92±0.17	1.98±0.18	1.42
SU 91 Psi	0.89±0.11	2.10±0.13	1.36

Table 5.5: Values of the ratios ψ'/ψ and ψ/DY obtained by fitting each data set independently.

5.3.1.2 Results from a simultaneous fit

In order to 'add' the results from the several data sets of each projectile–target combination, a fit is done simultaneously on all those mass spectra, leaving also free the fraction of signal that comes from each specific data set. Indeed, the number of 'signal' events must be the same in those several data sets (since the absolute cross–sections for the production of those processes do not depend on the setup), apart from a global factor, merely expressing the different integrated luminosities. On the contrary, the background contribution is strongly dependent on the hadron absorption properties of the setup, therefore being specific of each data set. This procedure is equivalent to impose that all data sets give the same values for the *ratios* between the several 'signal' processes.

Figure 5.4 gives a somewhat technical view of the fitting procedure, as performed on the p–W and p–U data. The first 12 points map the mass region from 3.0 to 4.2 GeV (in 100 MeV bins) while point 13 sums the (exclusively Drell–Yan) window between 4.2 and 5.5 GeV. The following 13 points have the same meaning but are from the other data set being (simultaneously) fitted. Figures 5.5 and 5.6 give a more usual representation of the fit to the p–A and S–U data sets.

The corresponding results, also including the (absolute) number of Drell–Yan events, are collected in table 5.6.

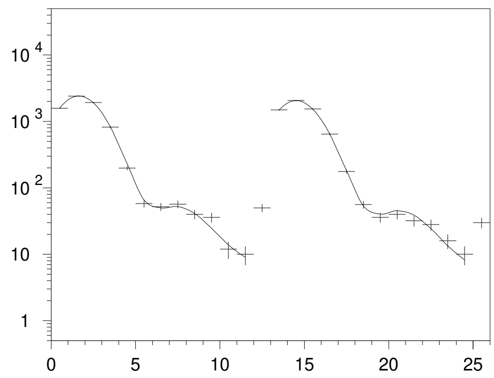

Figure 5.4: Illustration of the (simultaneous) fitting method, in the p–W (left) and p–U (right) data.

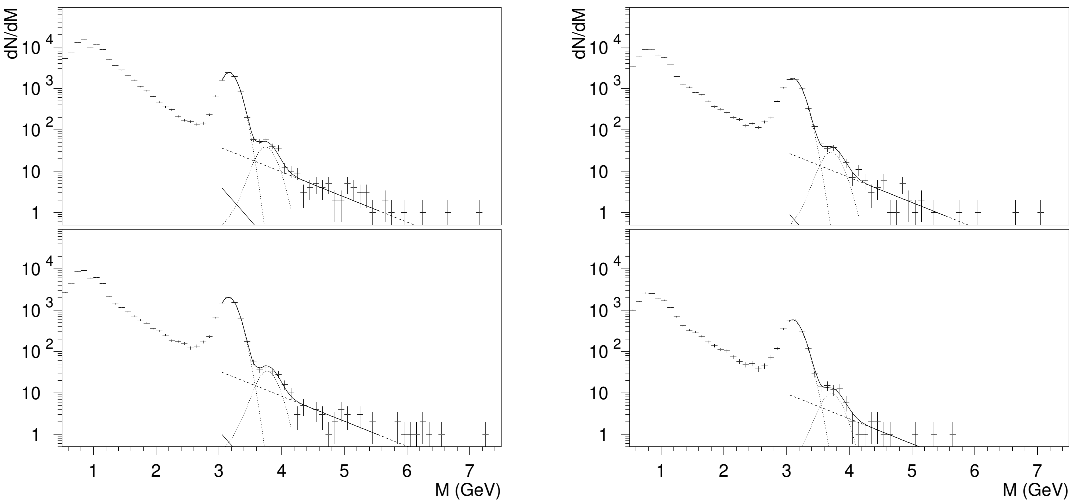

Figure 5.5: Result of the (simultaneous) fit, in the p–W (left) and p–U (right) data.

	ψ'/ψ (%)	ψ/DY	$N^{\rm DY}$ ($\times 10^3$)	χ^2/ndf
p–W	1.80±0.17	2.55±0.25	29.5±2.9	0.80
p–U	1.77±0.22	2.76±0.38	15.5±2.1	0.95
S–U	0.93±0.08	2.03±0.09	184.1±8.0	1.12

Table 5.6: Results from the simultaneous fit to all the data sets of each projectile–target combination. $N^{\rm DY}$ is the (total) number of Drell–Yan events, corrected for acceptances and ϵ_v efficiency.

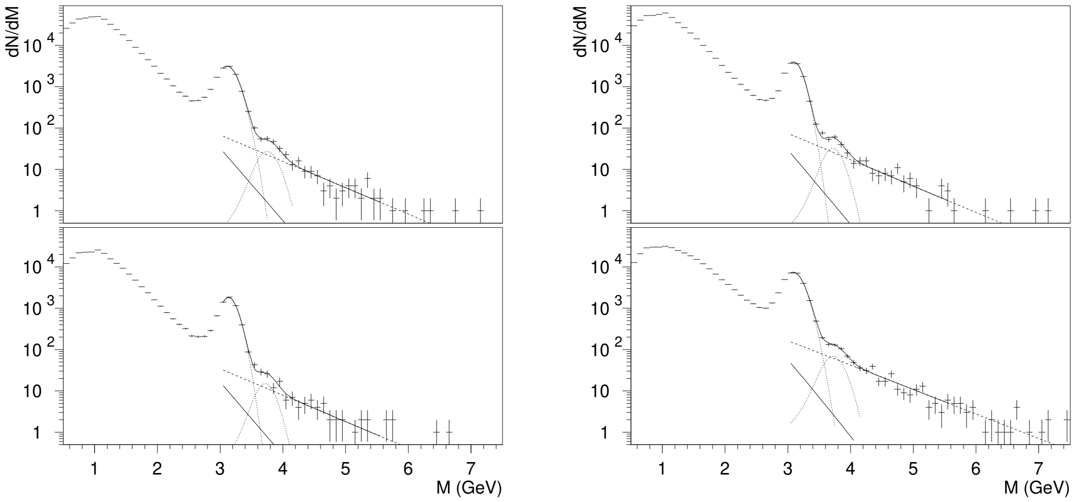

Figure 5.6: Result of the (simultaneous) fit to the S–U data sets: SU 90 St (left top); SU 90 Al (left bottom); SU 91 Phi (right top); SU 91 Psi (right bottom).

The ratio ψ'/ψ (ratio of production cross-sections times branching ratios into muon pairs, since the luminosities are the same for both resonances) shows an impressive decrease from the values measured in p–A collisions to the value measured in S–U,

$$\left.\frac{\psi'}{J/\psi}\right|_{SU} \Bigg/ \left.\frac{\psi'}{J/\psi}\right|_{pA} = \frac{0.93 \pm 0.08}{1.79 \pm 0.19} = 0.52 \pm 0.07\ . \tag{5.7}$$

Also the ratio ψ/DY drops from p–A to S–U but it is not appropriate to do such a direct comparison since Drell–Yan is isospin dependent and the proton is certainly not isoscalar (while the sulphur is). We should first extrapolate the p–A result into a N–A value, where N stands for 'nucleon' (half a deuteron). We do this by comparing the Drell–Yan cross–sections given by PYTHIA for the 4 possible combinations (see section 4.1). In just the same way as we added the nucleon–nucleon cross–sections to get the p–U value, for N–U we obtain

$$\sigma_{NU} = 0.5 \cdot (\sigma_{pU} + \sigma_{nU}) = 0.5 \cdot (62.9 + 48.8) = 55.9 \text{ nb}\ . \tag{5.8}$$

From this value we see that the Drell–Yan cross–section in N–U collisions is smaller than in p–U collisions (by 55.9/62.9=0.89). Since J/ψ production is essentially dominated by fusion of gluons, equally abundant in protons or neutrons, to get the ψ/DY ratio in a N–A interaction we just have to correct the p–A value for the Drell–Yan part. This isospin correction is the same, 12 %, for p–W or p–U interactions. So, if we take the ψ/DY value in p–A to be the mean between the p–W and p–U values, we should evaluate the 'J/ψ suppression' when going from

N–A to S–U collisions as,

$$\left.\frac{J/\psi}{\mathrm{DY}}\right|_{SU} \Big/ \left.\frac{J/\psi}{\mathrm{DY}}\right|_{NA} = \frac{2.03 \pm 0.09}{(2.61 \pm 0.30) \times 1.12} = 0.78 \pm 0.07\,. \tag{5.9}$$

5.3.2 Comparison with previous measurements

The values found for the ratio ψ'/ψ in p–W and p–U collisions can be directly compared to the measurements of other experiments, already presented in figure 1.8 on page 21. This is done in table 5.7 and in figure 5.7, where besides the points of the other experiments (circles) and the values obtained in this work (squares) we have also included some preliminary results [Lou 95] concerning other NA38 (and NA51) data, collected with a 450 GeV proton beam: p–C, p–Al, p–Cu and p–W (triangles); p–H_2 and p–D_2 (stars). The horizontal line is drawn at 1.8 %.

	p_{lab} (GeV)	$B\sigma^{\psi'}$ / $B\sigma^{\psi}$ (%)	Exp.t
p–W	200	1.80 ± 0.17	NA 38
p–U	200	1.77 ± 0.22	NA 38
p–C	450	2.02 ± 0.27	NA 38
p–Al	450	1.23 ± 0.35	NA 38
p–Cu	450	1.69 ± 0.14	NA 38
p–W	450	1.67 ± 0.20	NA 38
p–H_2	450	1.97 ± 0.06	NA 51
p–D_2	450	2.03 ± 0.06	NA 51
p–p	$\sqrt{s} = 63$	1.9 ± 0.6	ISR
p–Li	300	1.88 ± 0.26	E 705
p–Be	400	1.7 ± 0.5	E 288
p–C	225	1.6 ± 0.9	E 444

Table 5.7: Values of the ratio ψ'/ψ obtained with several targets and energies.

Figure 5.7 clearly shows that the ratio ψ'/ψ is essentialy insensitive to any changes of the target nucleus or of the collision energy. In other words, whatever happens to a J/ψ in the nuclear medium, the same happens to the ψ', in p–A collisions.

5.3.3 Relative A-dependences

An alternative way of expressing the different behaviour of the J/ψ, ψ' and Drell–Yan physical processes, when going from p–A to S–U interactions, is by looking at their 'A-dependences'. This is done assuming that the production cross–section of these mechanisms increases as a power law in A. For instance,

$$\sigma^{\psi}|_{SU} = \sigma^{\psi}|_{pU} \times 32^{\alpha^{\psi}}\,. \tag{5.10}$$

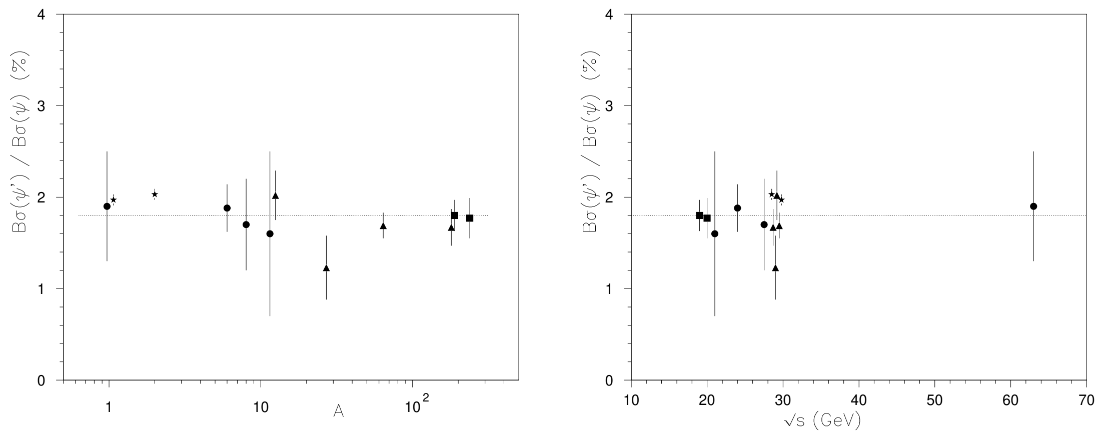

Figure 5.7: Ratio $B\sigma^{\psi'}\ /\ B\sigma^{\psi}$ in p–A collisions as a function of A (left) and as a function of the reaction energy (right).

This way, and since the branching ratios are the same in p–A or S–U, we can translate the $B\sigma^{\psi'}\ /\ B\sigma^{\psi}$ ratio into a $\Delta\alpha$,

$$\alpha^{\psi'} - \alpha^{J/\psi} = \ln\left(\frac{\sigma^{\psi'}/\sigma^{J/\psi}|_{SU}}{\sigma^{\psi'}/\sigma^{J/\psi}|_{pU}}\right) \Big/ \ln(32)\,. \tag{5.11}$$

From the particle ratios reported above we get $\alpha^{\psi'} = \alpha^{J/\psi} - 0.19$ and $\alpha^{J/\psi} = \alpha^{\mathrm{DY}} - 0.09$. Assuming $\alpha^{\mathrm{DY}} = 1$, we estimate $\alpha^{J/\psi} \sim 0.91$ and $\alpha^{\psi'} \sim 0.72$.

While the value found for $\alpha^{J/\psi}$ of the *projectile*, agrees with the value found by changing the *target* ($\sim$ 0.92, see section 1.9 on page 20), the $\alpha^{\psi'}$ value is considerably lower. This indicates that the projectile dependence of J/ψ production is quite similar to the target A-dependence, while the ψ' resonance exhibits a different behaviour.

5.3.4 S–U results in 4 E_{T} bins

In the case of S–U collisions, the ratio between ψ' and J/ψ yields was also obtained as a function of E_{T}. As done for the 'all E_{T}' sample, the background shape (and normalization) is previously obtained by fitting the corresponding like-sign spectra (now per ΔE_{T} bin). The 'luminosity fractions' of each data set are left free in these fits, therefore being allowed to change from one ΔE_{T} bin to another. This is necessary since the partition of the events per ΔE_{T} bin depends on the data set, due to different calorimeters (E_{T} resolutions) and different $\epsilon_v(E_{\mathrm{T}})$.

As an example, figure 5.8 shows the fit to the mass distributions corresponding to the last ΔE_{T} bin. The ψ'/ψ and ψ/DY values resulting from these fits are collected in table 5.8.

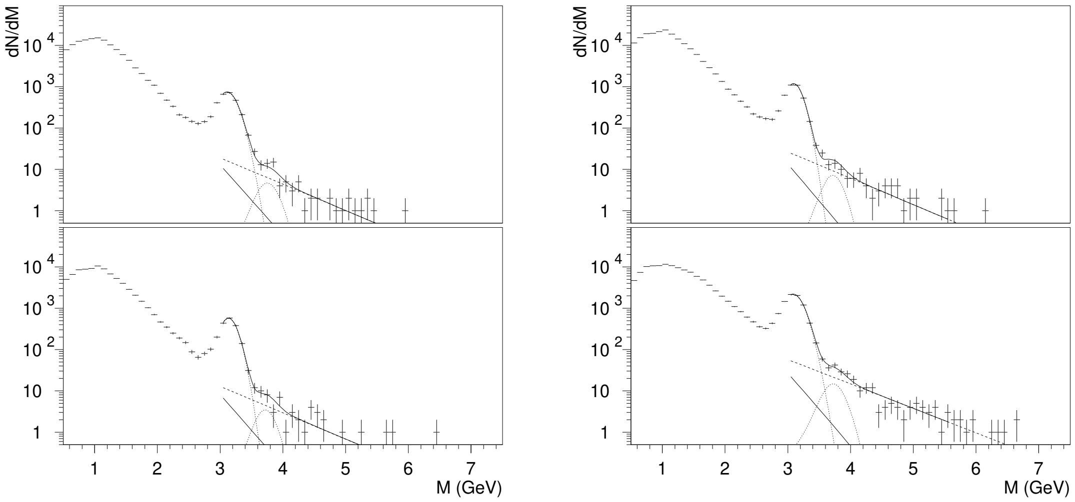

Figure 5.8: Same as figure 5.6 but only using events with E_T above 75 GeV.

As would be expected after seeing the decrease from p–A to (all E_T) S–U, the ratios ψ'/ψ and ψ/DY also exhibit a clear tendency to decrease as a function of E_T, within S–U collisions.

ΔE_T	ψ'/ψ (%)	ψ/DY	χ^2/ndf
10–39	1.14±0.16	2.48±0.25	1.02
39–58	1.09±0.15	2.54±0.26	1.21
58–75	0.84±0.15	1.77±0.13	1.25
>75	0.68±0.15	1.70±0.13	0.80

Table 5.8: Values of the ratios ψ'/ψ and ψ/DY obtained for each ΔE_T bin.

Since the E_T variable is quite specific of the NA38 experiment, it is useful to have other centrality estimators. Using a simple geometrical model [Bag 90] the following alternative variables have been computed: the mean impact parameter, b; the mean overlap area of the two nuclei, S; and the corresponding energy density, ϵ, calculated from the (Bjorken) formula

$$\epsilon \; = \; \frac{3 \cdot E_T^0}{\tau \cdot \Delta y \cdot S} \, , \tag{5.12}$$

where $\Delta y = 2.4$ and $\tau = 1$ fm. Another variable that can be used as an estimator of centrality, particularly interesting when comparing p–A and nucleus–nucleus collisions [Ger 92], is the mean length the particles travel inside nuclear matter, L. This parameter is estimated assuming that the *measured* increase in the (squared) mean p_T value of the J/ψ, relative to some starting scenario identified with p–p collisions, is proportional to the length of nuclear medium crossed (by analogy with the multiple scattering mechanism),

$$< p_{\mathrm{T}}^2 >^{J/\psi} (\Delta E_{\mathrm{T}}) - < p_{\mathrm{T}}^2 >^{J/\psi} (pp) \propto L(\Delta E_{\mathrm{T}})\,. \tag{5.13}$$

The values of this variable have also been computed, for each ΔE_{T} bin, being included in table 5.9, together with the other centrality estimators.

$< E_{\mathrm{T}} >$ (GeV)	b (fm)	S (fm^2)	ϵ (GeV/fm^3)	L (fm)
24.8 (8.3)	7.03 ± 0.71	23.4 ± 5.2	1.32 ± 0.30	6.7 ± 0.8
48.7 (5.5)	5.47 ± 0.63	35.0 ± 4.5	1.74 ± 0.22	7.9 ± 0.9
66.8 (4.9)	4.06 ± 0.68	43.3 ± 2.7	1.93 ± 0.12	9.1 ± 1.1
87.4 (9.3)	2.36 ± 0.94	45.8 ± 0.4	2.39 ± 0.14	10.3 ± 1.3

Table 5.9: Values of several centrality estimators, alternative to E_{T}.

The 'charmonia suppression', as a function of E_{T}, can be appreciated in figure 5.9, where the values of both ratios, ψ'/ψ and ψ/DY, are presented. The p–A points, corrected for isospin in the case of ψ/DY, are included to ilustrate the drop from p–A to S–U.

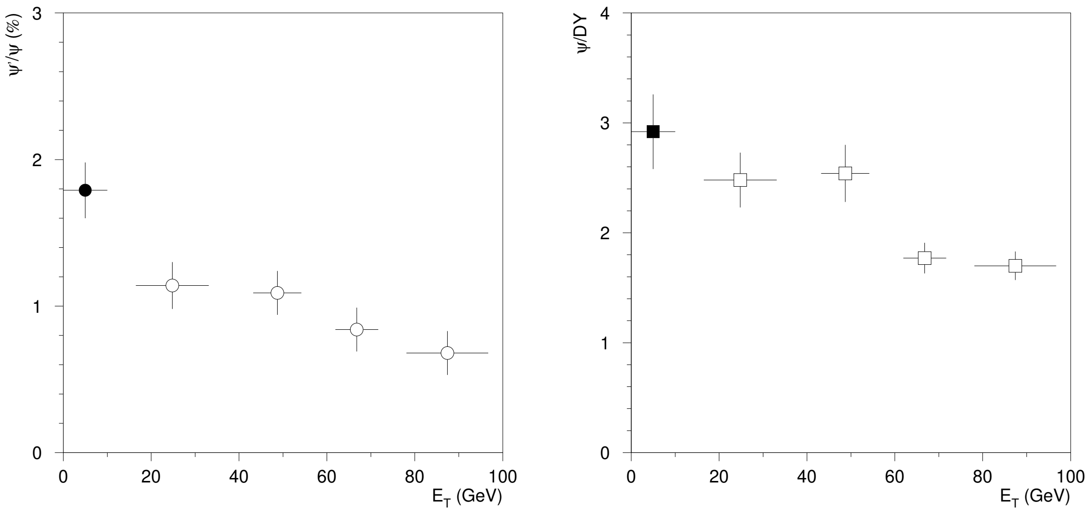

Figure 5.9: Ratios ψ'/ψ and ψ/DY in the 4 E_{T} bins of S–U. The p–A values are included merely as an illustration.

5.4 Absolute cross sections in the HMR

In this section we present the absolute cross–sections for the production of J/ψ, ψ' and Drell–Yan events (times the braching ratio into muons in the case of the resonances).

As already discussed above, the procedure of simultaneously fitting the several data sets of a given combination projectile–target, besides giving the number of events of each physical process, also gives the fraction of events contributed by each data set. The pW 88 V contributes 53.4 % of the p–W events while the pU 87 is responsible for 74.8 % of the p–U ones. The distribution of the S–U events is: 18.9 % (90 St); 9.1 % (90 Al); 18.8 % (91 Phi); 53.2 % (91 Psi). Knowing these fractions and the total number of events, we get the corresponding absolute cross–sections using the luminosities given before, specific of each data set.

It is important to compare the *ratios of luminosities* obtained by the fitting procedure with the (completely independent) luminosity measurements described in section 3.2. In the p–W case, from the fit, we get $\mathcal{L}$ (pW 88 V) / $\mathcal{L}$ (pW 88 D)= 1.15, to be compared with the ratio of luminosities, 153 nb^{-1}/132 nb^{-1}=1.16. For S–U, since we only know the '90 luminosities, we can evaluate the ratio SU 90 St over SU 90 Al: 2.06 from the fit and 1.99 from the absolute luminosity values. The excelent agreement found between these two quite independent evaluations, gives further support both to the simultaneous fitting procedure and to the absolute luminosity estimations. In the p–U case, however, we get $\mathcal{L}$ (pU 87) / $\mathcal{L}$ (pU 88)= 2.97 from the fit while the ratio of absolute luminosities would suggest a factor 3.86. This confirms that the absolute luminosities of the p–U data sets should not be trusted. Therefore, we will not present any p–U absolute cross–sections.

5.4.1 Drell-Yan cross-sections and K factors

In table 5.10 we collect the known luminosities, the corresponding number of Drell–Yan events and the K factor we get by comparing the calculated Drell–Yan cross–sections with the theoretical predictions given in section 4.1, always in the restricted kinematical domain chosen for the present analysis.

	$\mathcal{L}$ (nb^{-1})	$N^{\rm DY}$ ($\times 10^3$)	$\sigma^{\rm DY}$ (μb)	K
pW 88 V	153	15.8 ± 1.5	0.103 ± 0.01	2.11 ± 0.2
pW 88 D	132	13.7 ± 1.4	0.104 ± 0.01	2.13 ± 0.2
SU 90 St	8.95	34.8 ± 1.5	3.89 ± 0.17	2.17 ± 0.1
SU 90 Al	4.50	16.8 ± 0.7	3.72 ± 0.16	2.08 ± 0.1

Table 5.10: The Drell–Yan K factor in p–W and S–U collisions.

5.4.2 J/ψ and ψ' cross sections

To get the J/ψ and ψ' cross–sections (multiplied by the corresponding branching ratios into muons) we have redone the fit to the p–W and S–U data sets, this time with the free parameters being the absolute normalization of the J/ψ, ψ' and

	$N^{J/\psi}$	$N^{\psi'}$
p–W	75171 ± 694	1350 ± 128
S–U	373900 ± 1700	3475 ± 298

Table 5.11: Total number of J/ψ and ψ' events, corrected for acceptances and ϵ_v efficiency.

Drell–Yan contributions (see table 5.11), rather than their ratios (this facilitates the calculation of the error bars).

For each projectile–target combination, the two (independent) normalizations available are in perfect agreement. Therefore, table 5.12 only includes the corresponding mean value of the J/ψ and ψ' cross–sections.

	$\mathcal{L}$ (nb^{-1})	$B\sigma^{J/\psi}$	$B\sigma^{\psi'}$
p–W	285	264±2 nb	4.7±0.4 nb
S–U	48.1	7.78±0.04 μb	72±6 nb

Table 5.12: J/ψ and ψ' cross–sections, times their branching ratio into muons, within our phase space window: $3 < y_{\rm lab} < 4$, $|\cos(\theta)| < 0.5$.

5.4.3 Comparison with previous measurements

The Drell–Yan K factors found in p–W and in S–U collisions can be directly compared to the values previously measured by other experiments, reported in table 1.1 on page 16, and to the value we get for the p–Pt data of NA3, 2.1±0.3 (end of section 4.1). Our values are perfectly compatible with the others, specially when we add to the statistical errors given in table 5.10 the systematical uncertainty, dominated by the normalization procedure and roughly estimated to be around 10 %.

In the case of the J/ψ resonance, to compare with the measurements of other experiments we must extrapolate the values obtained into a different phase space region. To get the whole $\cos(\theta)$ domain (a safe extrapolation) our values should be multiplied by 2. To go from our rapidity domain, between 3 and 4 in the laboratory system, to the $x_F > 0$ domain of the previously published measurements, we have to assume some kinematical distributions that cannot be certified beyond our acceptance window. Using reasonable x_F distributions [Bag 91b], it is possible to estimate that the J/ψ cross–section should be multiplied by ~ 1.07 to go from the rapidity domain to the x_F domain.

From the value found for p–W collisions, 564 ± 5 nb, we can obtain the corresponding J/ψ cross–section 'per nucleon', using $\alpha^{J/\psi} = 0.92$. The result is 4.64 nb, perfectly compatible with the values previously reported (and collected in table 1.2 on page 20), as is shown in figure 5.10.

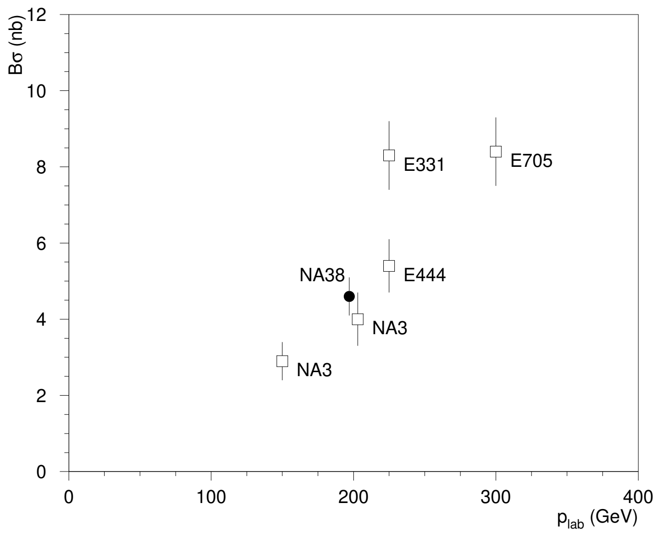

Figure 5.10: J/ψ cross-sections (times branching ratios into muons), per target nucleon and for $x_F > 0$, as a function of $p_{\rm lab}$.

The corresponding positive x_F J/ψ cross–section in S–U collisions is 16.64 ± 0.08 μb, leading to 4.47 nb/nucleon if we take $\alpha^{J/\psi} = 0.92$, both for the target and for the projectile. In figure 5.10 this S–U value would be indistinguishable from the p–W point.

We should stress that these values are in perfect agreement with the numbers previously published [Bag 91b] by NA38: 698 ± 37 nb for p–U (or 4.54 nb/nucleon) and 16.33 ± 0.60 μb for S–U (from the data collected in 1987).

5.5 The Intermediate Mass Region in p–A collisions

5.5.1 Relative studies

We now turn to the study of the dimuon continuum between the low mass vector mesons and the J/ψ, in the p–A data sets.

Using the high mass region to fix the Drell–Yan normalization, we are able to overcome the correlation between both 'continuous' signal processes in the fit to the intermediate mass region and get the charm normalization. The combinatorial background has a substantial contribution to this mass region. In the case of p–W interactions, where we have data taken with two very different setups (see section 4.4), we can easily isolate the charm component, since (by definition) the background is the only contribution that might change with the geometry and properties of the absorber materials used in the experimental setup.

We have (simultaneously) fitted both p–W mass distributions, between 1.5 and 2.5 GeV, leaving as free parameters in this fit the R^{Bg} factor and the normalization of the $\mathrm{D\bar{D}}$ contribution (relative to the Drell–Yan normalization). The other processes were kept fixed to the values determined from the fit to the mass region above 3 GeV. Figure 5.11 shows the fitted (signal) mass spectra. The results of this fit are $R^{\mathrm{Bg}} = 1.19 \pm 0.04$ and $\mathrm{D\bar{D}/DY} = 0.86 \pm 0.06$, with a $\chi^2/\mathrm{ndf} = 1.59$.

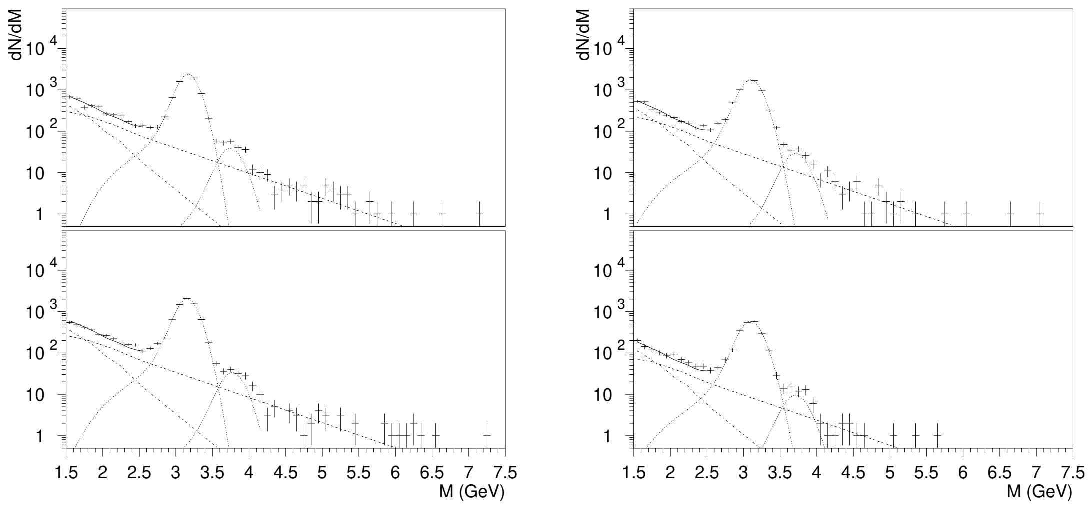

Figure 5.11: 'Signal' dimuon mass distributions in p–W (left) and p–U (right) collisions, with the J/ψ, ψ' and Drell–Yan normalized from the HMR fit.

In the p–U analysis, where a 'measurement' of R^{Bg} is not possible, we have imposed the value found in p–W. The corresponding fit, having the ratio $\mathrm{D\bar{D}/DY}$ as the only free parameter, is also illustrated in figure 5.11, leading to a ratio $\mathrm{D\bar{D}/DY} = 0.96 \pm 0.04$, with 1.36 as the corresponding χ^2/ndf. Notice that $\mathrm{D\bar{D}/DY}$ is the ratio of cross–sections (times branching ratios in the case of charm), in the phase space region chosen for the analysis (where the acceptance values were calculated).

5.5.2 Absolute studies

We have just seen that the *shape* of the dimuon mass distribution in the 'continuum' between the low mass vector mesons and the J/ψ resonance, can be explained, in p–A interactions, by a superposition of the Drell–Yan process (fixed by the HMR analysis and extrapolated down in mass) superimposed on the contribution from the semi-leptonic decays of the charmed mesons. Before we accept this 'model' as the correct description of the data, we must see if it also holds from the *normalization* point of view.

From the ratio $D\bar{D}$/DY and the number of Drell–Yan events (see table 5.6 on page 87) we get the number of charm events (corrected for acceptances and efficiencies), which can be normalized into nb by using the (p–W) luminosity. The value obtained, 0.48 nb per nucleon, corresponds to the cross–section for producing a pair of charmed mesons, times the probability to have both mesons decaying into muons, times the probability to have the muon pair in our phase space domain.

To get a more informative quantity we have used PYTHIA to obtain the *ratio* between the total number of generated events and the number of events with a pair of muons in our kinematical window. This factor, 19.7×10^3, corrects both for the fraction of phase space accessible to NA38 and for (a ponderated mean of) the branching ratios (squared) for the charmed mesons decay into muons. Notice that the Λ_c contribution to the muon spectra was neglected in this simulation.

This way we deduce our estimation of the total charm production cross–section, in p–p collisions at 200 GeV: 9.5 ± 2 μb. The quoted error is just meant to give some feeling for the uncertainties associated with the data normalization, the kinematical distributions of the charmed mesons and their branching ratios into muons, etc.

5.5.3 Comparison with previous direct measurements

The charm cross–section value obtained in this way is not far from what we would expect, on the basis of the direct measurements provided by other experiments, already presented in section 1.10 on page 21.

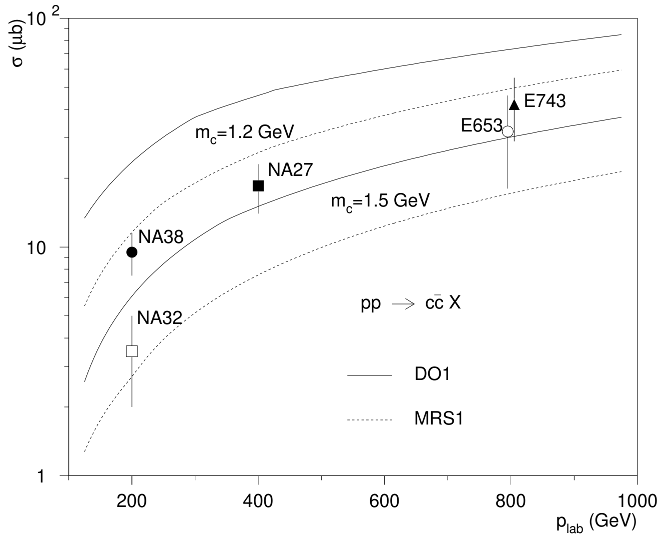

Figure 5.12: Charm cross-section value estimated (within some hypothesis, see text) from the NA38 p–W data, compared to the values already presented in figure 1.9 on page 22.

In order to better illustrate this comparison, we have included our estimated value in the figure 5.12 (a copy of figure 1.9). The theoretical calculations (curves) help to guide the eye and stress the consistency of our point.

5.6 The IMR in S–U interactions

From the results presented in the previous section, we conclude that the superposition of the Drell–Yan process and the simultaneous semi-leptonic decays of $D\bar{D}$ pairs into muons, provides a good description, *in shape and in normalization*, of the dimuon continuum measured in p–W and p–U collisions between the ϕ and J/ψ resonances. After this successful understanding of the p–A data on the basis of these 'known sources' it seems reasonable to make a further extrapolation into S–U interactions and compare the resulting 'expectations' with the data.

5.6.1 S-U excess relative to p–A linear extrapolation

To minimise the dependence on the (more uncertain) absolute normalizations, we take from the p–A analysis the *ratio* between the $D\bar{D}$ and Drell–Yan contributions to the dimuon mass spectra and assume that it remains the same in S–U collisions. Yet, we should not forget that Drell–Yan is sensitive to the proportion of protons and neutrons in the nuclei and that we are working with data taken with a proton rather than a deuteron beam. Therefore, we expect the ratio $D\bar{D}$/DY to be 1.01 in S–U, instead of the value (0.90) found in p–A.

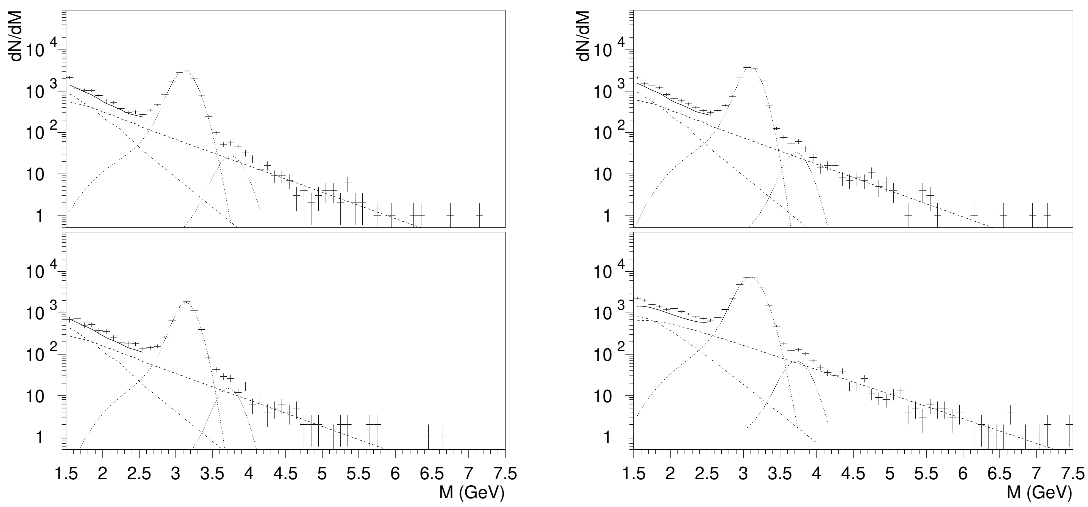

Figure 5.13: 'Signal' dimuon mass distributions in the four S–U data sets, in the same order as in figure 5.6, wherefrom the normalization of the HMR processes is taken.

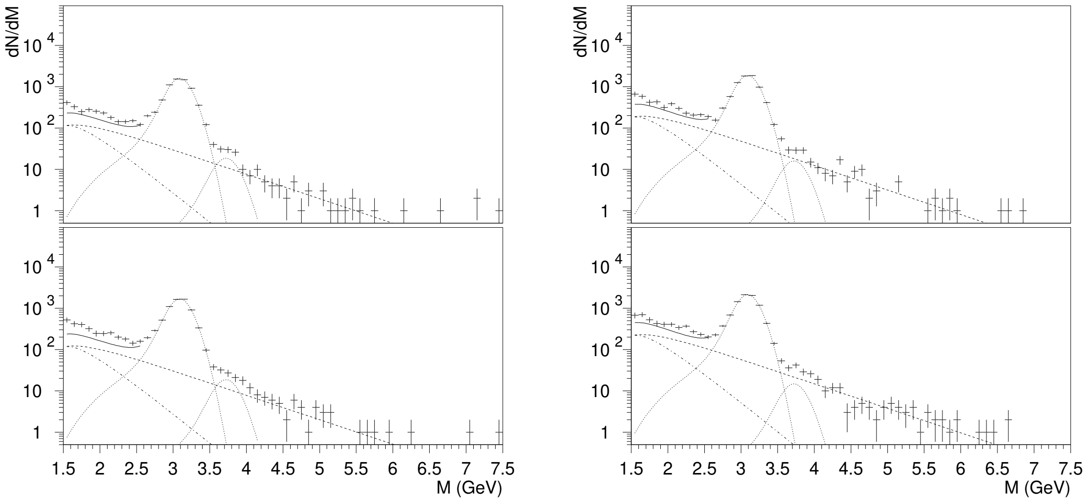

Figure 5.14: 'Signal' dimuon mass distributions from the SU 91 Psi data set, in the 4 ΔE_{T} bins. The J/ψ, ψ' and Drell–Yan contributions are normalized from the corresponding HMR fit.

Figure 5.13 shows the charm contribution to the S–U data, normalized by this 'linear' extrapolation of the p–A results. The superposition of this charm estimation on the Drell–Yan line, normalized from the HMR, fails to explain the S–U intermediate mass region, as is clearly visible in this figure.

Figure 5.14 illustrates that the difference between the *measured* signal distribution and the *expected* line does not show any strong change with E_{T}.

5.6.2 Quantification: measured over expected signal

In order to quantify this 'excess', we have computed the ratio between the integral of the 'measured' signal mass distribution and the corresponding 'expected' value, in the mass range from 1.5 to 2.5 GeV. While the p–A value is 1, by construction, for the S–U data we get the value 1.26$\pm$0.1, meaning that we observe 26 % more (signal) events than what would be expected from a linear extrapolation of the proton–nucleus results.

By repeating this procedure in each ΔE_{T} bin, we get the values presented in figure 5.15. The values in the left figure were obtained using always R^{Bg}=1, while those in the right figure correspond to the use of a variable (decreasing as a function of multiplicity) R^{Bg} factor: 1.07, 1.03, 1.00 and 1.00, for the successive ΔE_{T} bins. This set of values is just an 'educated guess'. The difference between the two sets of points indicates how sensitive this study is to a correct evaluation of the background component, mainly in the low E_{T} collisions, where the charged multiplicity might be small enough to make R^{Bg} bigger than unity.

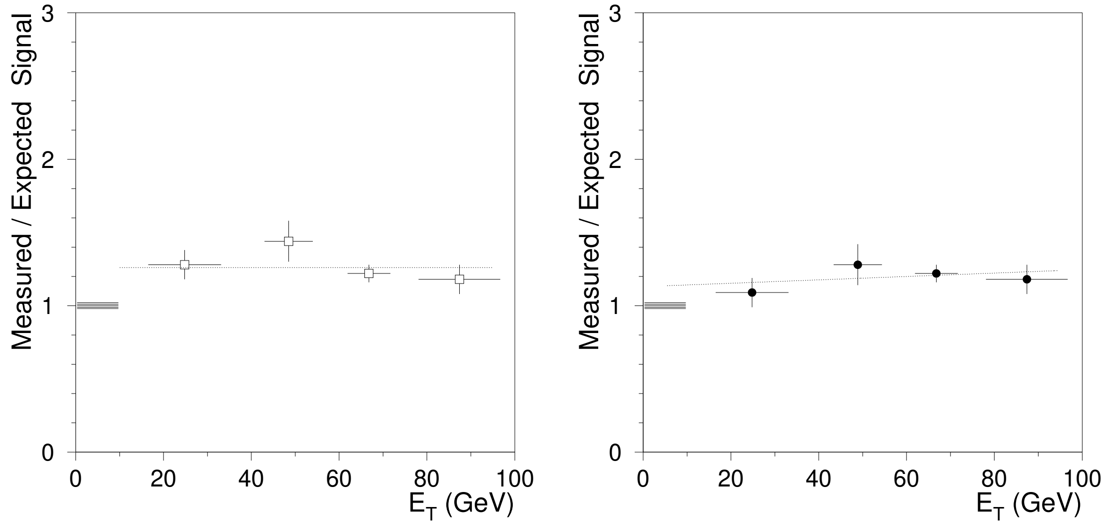

Figure 5.15: Ratio between the measured and the expected signal, as a function of E_{T}, for a constant (left) or variable (right) R^{Bg}.

This figure also illustrates the difficulty in judging the E_{T} dependence of the 'excess'. The 'known sources', Drell–Yan and charm production, being hard processes ($\alpha = 1$), scale linearly with E_{T}. So, if the ratio 'measured over expected signal' is constant, as suggested by the open squares, the 'excess' has a linear E_{T} dependence, like the other processes involved. On the other hand, if we see a linear increase, as compatible with the closed circles, we are dealing with a process that increases quadratically with E_{T}.

5.7 Systematical uncertainties

The main source of (systematical) error in the *relative results* comes from the determination of the *shapes* of the several contributions to the opposite-sign mass spectra. If we change the parametrizations of these shapes, within reasonable limits, the final results (ratios) might change by about 10 %.

For the IMR analysis of the S–U data, not knowing the value of R^{Bg} in the low E_{T} bin adds an important systematical uncertainty.

In the case of the proton *absolute results*, the systematical uncertainty is essentially dominated by the beam counting — for example, due to the pion contamination of the beam — being roughly estimated to be around 10 %.

The *sulphur* absolute normalization requires a difficult extrapolation down to very peripheral collisions ($E_{\mathrm{T}} \sim 0$ GeV). This asks for the knowledge of the differential E_{T} cross–section (for J/ψ production, for instance), whose measurement is not possible from the data collected by the NA38 experiment, in the very low E_{T} region, where the target inefficiencies play a major role (see section 3.5 on page 53.

Since the dimuon trigger favors high multiplicity collisions, the fraction of J/ψ events, for instance, rejected by the low $E_{\rm T}$ cut should not be very large (contrary to what would happen in a 'minimum bias' $E_{\rm T}$ distribution, as those measured by other heavy ion experiments). Therefore, our estimate (8 %) is probably not far from reality and an overall absolute normalization uncertainty of about 10 % seems a reasonable estimation.

5.8 Interpretation of the results

We were able to explain the p–A dimuon mass spectra (above 1.5 GeV), both in shape and in absolute normalization, on the basis of 'conventional wisdom'. These are 'expected' results.

The S–U data, however, shows a 'suppressed' ψ' and an 'excess' in the IMR continuum. It is probably too soon to have a good perspective of all the possible effects that might be required for a correct interpretation of these 'unconventional' results. The following lines might be helpful in future discussions.

5.8.1 The ψ' suppression

Figure 5.16 shows a comparison between the values we have obtained, for the $E_{\rm T}$ dependence of the $B\sigma^{\psi'}$ / $B\sigma^{\psi}$ ratio, and the predictions of some theoretical models.

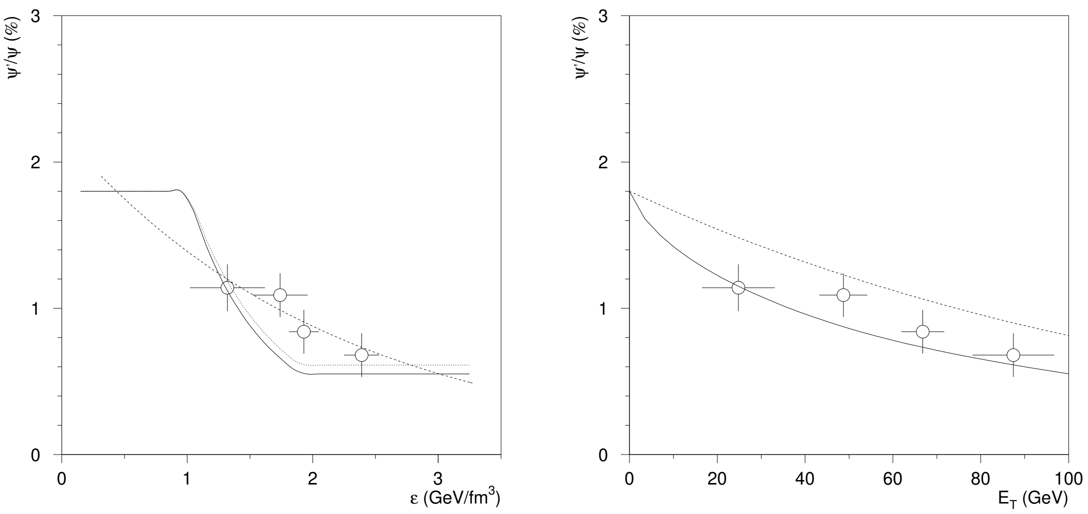

Figure 5.16: Comparison between the measured values and the curves predicted by the 'QGP' and 'nuclear absorption' models.

On the left side figure, the data is plotted as a function of the energy density (see table 5.9 on page 92). The solid line is the curve calculated within the QGP scenario, as explained in section 1.5, normalized to the p–A value, with $\epsilon_c = 1$ GeV/fm^3 and $\epsilon_{J/\psi} = 1.9\,\epsilon_c$ (see equation 1.6 on page 12). The dotted line is the same curve but assuming that 40 % (instead of 30 %) of the observed J/ψ events are the result of a χ_c decay. The dashed line is simply an exponential, with slope 0.46 fm^3/GeV, and illustrates how a 'nuclear absorption' curve could go through the S–U data points. The meaning of the slope parameter depends on the specific absorption model. For instance, it is possible to infer that the ψ' absorption cross–section is $\sim$ 6 mb larger than the J/ψ value. It is not so clear if it is compatible with the observation that the ψ'/ψ ratio stays constant in p–A collisions, as A increases. That might be the case *if* all the p–A collisions (with $A = 1$ or 238) would had the same energy density value ($\sim$ 0.4–0.5 GeV/fm^3).

The figure on the right side compares the data points, as a function of E_{T}, with two predictions [Vog 93] obtained in the framework of the 'comovers' model [Gav 90]. Both curves consider absorption by nucleons and comovers, for which a density of 0.8 fm^{-3} was assumed. The J/ψ and ψ' absorption cross–sections were considered as constant (solid line), with $\sigma(J/\psi\ N) = 3.5$ mb and $\sigma(\psi'\ N) = 8.4$ mb, or growing as the square of the formation times (dashed line), with $\tau_{J/\psi} = 1.2$ fm and $\tau_{\psi'} = 2$ fm. The comover cross–sections were taken as 2/3 of the nucleon ones. The calculation takes into account the nuclear density distributions and averaging over the impact parameter. The E_{T} variable was previously tuned to match the NA38 E_{T} distributions. Both curves were normalized to 1.8 % at E_{T}=0.

5.8.2 The IMR continuum enhancement

Why do we see more events in the S–U IMR continuum than what would be expected by extrapolating the p–A data, assuming a linear (projectile) A-dependence? Let's address some possible explanations.

Are we seeing some evidence of thermal dimuons production? The answer to this question must wait until we know whether the E_{T} dependence of the 'excess' is linear or quadratic.

Could it be that the Drell–Yan contribution is larger in the IMR than what we assumed? In other words, could the Drell–Yan K factor be larger in this mass region than for higher mass values? Maybe, but why would the mass dependence of K in S–U be different from the one in p–A?

What about charm enhancement in nucleus–nucleus collisions? This is a possible explanation. In fact, if we fit the S–U dimuon mass distribution leaving free the normalization of the charm contribution, we get a reasonable description of the data (χ^2/ndf = 2.6) with 1.8 times more charm than the 'expected' amount.

But the first explanation that comes to mind is that there is some amount of un-subtracted background in the signal. Do we see some signs that would support this possibility? The answer is no.

If the 'excess' is originated by mesons decay, then we know its line shape. We can fit the data leaving the R^{Bg} factor free so that an increase of the background normalization will fill the difference between the data and the 'known sources'. When we do this, the fitting procedure sets R^{Bg} to 1.07 but the corresponding reduced χ^2 is 4.2, clearly illustrating the disagreement between the data and this (imposed) hypothesis.

If we repeat the fit leaving free both the charm and the background contributions, the best fit is obtained with $\mathrm{D\bar{D}/DY}$=1.96±0.11 and R^{Bg}=0.98±0.01, showing that the shape of the 'excess' is much more similar to the charm than to the background. The fitting procedure prefers to increase the charm normalization by a factor 2 than to increase the background component by 7 % !

One more hint is provided by the E_{T} dependence of the results. The combinatorial background has a well known quadratic behaviour that should leave a clear E_{T} dependence in the 'measured over expected' ratio. The problem is that we need to know the values of R^{Bg} per ΔE_{T} bin, in order to safely address this question. We cannot extract these values from the data, as we did for p–W, since we do not have data collected with sufficiently different experimental setups. All we can do is repeat the above mentioned fit, leaving free $\mathrm{D\bar{D}/DY}$ and R^{Bg}, per ΔE_{T} bin. In other words, since we are assuming that the normalization of the background component is uncertain, we ask the fitting procedure to tell us whether the 'excess' is better described by charm (enhancement) or by ('un-subtracted') background, as a function of E_{T}. The results of this test are collected in table 5.13.

ΔE_{T} (GeV)	"$\mathrm{D\bar{D}/DY}$"	R^{Bg}	χ^2/ndf	D/S
10–39	1.51±0.19	1.06±0.03	1.33	0.90±0.08
39–58	2.80±0.25	0.93±0.02	1.42	0.99±0.09
58–75	1.90±0.21	0.96±0.02	1.09	1.00±0.05
> 75	1.95±0.21	0.96±0.02	2.21	0.99±0.07

Table 5.13: Values of R^{Bg} per ΔE_{T} bin, if we assume that the 'excess' must be either charm or background. D/S are the corresponding values for the ratio between the measured 'data' and the expected 'sources'.

This is a simple test and the values should not be taken too seriously. Still, there is a strong suggestion that when we leave free the background normalization, the best fits are obtained with R^{Bg} values *lower* than the ones we would use (the 'educated guess'), therefore *increasing* the 'excess'. This test also indicates that R^{Bg} is greater than 1 in the first ΔE_{T} bin, giving some support to the 'closed circles' in figure 5.15, the ones that would be compatible with a quadratic E_{T} dependence for the 'excess' ...

Clearly, a proper analysis of the multiplicity dependence of the 'excess', essential for its physical interpretation, depends crucially on the knowledge of the corresponding background contribution (in particular, on the values of R^{Bg}). Therefore, any experiment that searches for signals of 'thermal dimuon' production (actually, any 'new physics') *must* collect data, in parallel, with (at least) two setups, very different in what concerns their hadron absorption properties. This is the only way to safely 'subtract' the meson decay background. The NA38 experiment did it for p–W collisions. In what concerns S–U, a step was taken in that direction in 1990, when data was taken with 3 different setups [Lou 90]. Unfortunately, the data collected in the third setup, where copper replaced the inner part of the calorimeter, suffered from some problems (like the beam hitting the copper absorber rather than the target) which prevented their use.

Since the background is relatively more important in the upstream sub-targets (see figure 3.3 on page 53) we thought that we might be able to 'extract' the R^{Bg} value by making a simultaneaous fit of the (opposite-sign) dimuon mass distributions, obtained in three different sets of sub-targets. We imposed that the (ratios of the) signal contributions, in each sub-target bin, are those found in the all events sample and fitted the fraction of signal events contributed from each event sub-sample from the mass spectra above 3 GeV. Then we looked in the IMR to see whether the ratio 'measured over expected' would decrease from the upstream to the downstream sub-targets, a sign of 'un-subtracted' background. This test did not provide any significative results. In fact, as is clearly shown in figure 5.17, there is no visible change in the ratio background over signal, as a function of the sub-target, for mass values above 1.5 GeV.

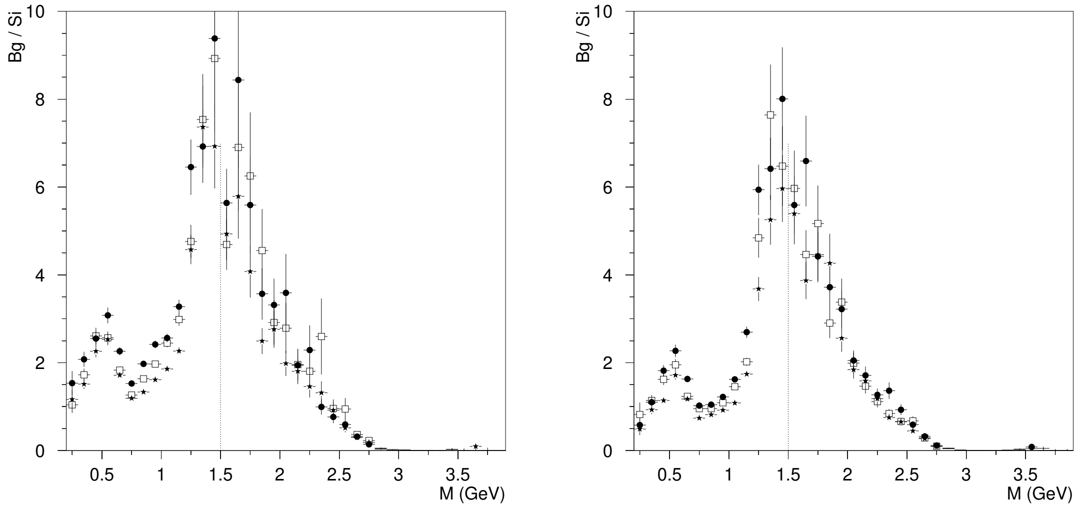

Figure 5.17: Ratio background over signal versus $M_{\mu\mu}$, for sub-targets 1–3 (closed circles), 4–6 (open squares) and 7–10 (stars), in the SU 90 St (left) and SU 91 Psi (right) data sets.

Only in the lower mass region, populated by decays of low energy mesons, the distance between the production point and the start of the absorbers makes a visible difference. Figure 4.14 on page 69 had already shown that the difference between the SU 91 Phi and SU 91 Psi setups, in what concerns the background fraction of events, is only visible in the mass region below 1.4 GeV.

References:

[Bag 89] C. Baglin *et al.* (NA38 Coll.), Phys. Lett. **B220** (1989) 471.

[Bag 90] C. Baglin *et al.* (NA38 Coll.), Phys. Lett. **B251** (1990) 472.

[Bag 91a] C. Baglin *et al.* (NA38 Coll.), Phys. Lett. **B255** (1991) 459; Phys. Lett. **B262** (1991) 362.

[Bag 91b] C. Baglin *et al.* (NA38 Coll.), Phys. Lett. **B270** (1991) 105.

[Ber 88] E.L. Berger, Proc. of the 'ARW on QCD Hard Hadronic Processes', St. Croix, Virgen Islands, 1987 (Argonne Preprint ANL-HEP-CP-88-26) and references therein.

[Gav 90] S. Gavin and R. Vogt, Nucl. Phys. **B345** (1990) 104. R. Vogt and S. Gavin, Proc. of QM'90, Menton, France, 1990; Nucl. Phys. **A525** (1991) 693c. S. Gavin *et al.*, Z. Phys. **C61** (1994) 351.

[Ger 92] C. Gerschel and J. Hüfner, Z. Phys. **C56** (1992) 171; C. Baglin *et al.* (NA38 Coll.), Phys. Lett. **B268** (1991) 453.

[Lou 90] C. Lourenço, "Hadron absorption properties of the NA38 1990 setups: 'Standard', 'Al2O3' and 'Copper'", NA38 Internal Note, October 1990.

[Lou 95] C. Lourenço, Proc. of the Hirschegg '95 Workshop, 'Hadrons in Nuclear Matter', Hirschegg, Austria, 1995 (Ed. GSI); LIP Preprint 95-03.

[Ron 93] B. Ronceux *et al.* (NA38 Coll.), Proc. of QM'93, Borlänge, Sweden, 1993; Nucl. Phys. **A566** (1994) 371c. C. Baglin *et al.* (NA38 Coll.), to appear in Phys. Lett. **B**.

[Vog 93] R. Vogt, private communication. S. Gavin, Proc. of QM'93, Borlänge, Sweden, 1993; Nucl. Phys. **A566** (1994) 383c.

Concluding remarks

Summary of results

The main results obtained in the present work are summarized in the following lines.

The absolute cross–sections measured in p–W and S–U collisions, for J/ψ and Drell–Yan production, agree very well with the values previously known: the Drell–Yan K-factor is found to be $\sim$ 2.1–2.2 and the J/ψ cross–sections (times branching ratio into muons) is $\sim$ 4.6 nb/nucleon, using $\alpha^{J/\psi} = 0.92$, both for the target and for the projectile A-dependence.

The ratio ψ'/ψ is found to be 2 times smaller in S–U collisions than in p–A collisions. A similar drop ('suppression') is also seen as a function of E_{T}, within S–U data.

We have shown that the intermediate mass region produced in p–A collisions *can* be understood on the basis of two well know ('conventional') physical processes: Drell–Yan and decays of charmed mesons. While being a strong reference in the framework of the nucleus–nucleus data analysis, providing its baseline, this is an important result in itself and deserves being stressed.

Finally, while the production of J/ψ and ψ' vector mesons is reduced when going from p–A to S–U interactions, the production of dimuons with mass in the region between the ϕ and J/ψ resonances is clearly *enhanced* in S–U collisions, in relation to what would be expected on the basis of a linear extrapolation of the p–A results.

Ideas for future research

The future work that will arise along the lines of the present study, also including the more recent S–U data collected in 1992, should improve some aspects of the data analysis. The following list is to be considered as a starting point.

- Simulate the multiple scattering, suffered by the muons while crossing the absorber materials, using the Molière description rather than the (Rossi) approximate gaussian formulation.

- Include the influence of the *beam* Fermi momentum in the generation of Drell–Yan and D$\bar{\text{D}}$ events, as already done for the J/ψ and ψ' resonances.

- Generate the events with final state charmed particles decaying into muons without changing their relative branching ratios (while still saving CPU time).

- Use the Monte Carlo output histograms directly in the fit to the experimental data instead of replacing them by analytical functions, that always introduce some additional bias. This new procedure has become available as an extension to the MINUIT program, but requires a different treatment of the background contribution (next point).

- Get the shape of the combinatorial background by mixing muons from different like-sign events. The resulting histogram has a poissonian nature, since no square roots are used in its derivation (therefore, the method indicated in the previous point can be used). It's *normalization* is still given by the standard formula, using the *integrated* number of like-sign events rather than their mass distributions.

- The generation of Drell–Yan and charm contributions depend on the quark and gluon distribution functions, which are not the same in a nucleus or in a nucleon. Therefore, it is desirable to replace the PYTHIA event generator by a different program that considers nuclei as the primary projectile and target particles, using the appropriate structure functions. HIJING is an example of an event generator that simulates hard processes (based on PYTHIA) in nucleus–nucleus collisions and should be tried.

- The p–W data was reconstructed with a setup specification that was not exactly the one used in the data taking process (as is clearly visible in the value of the J/ψ mass, 60 MeV higher than reported in the PDG tables). A new processing of these data in certainly desirable. In particular, it would allow a more direct comparison to the S–U mass spectra, by overlapping both spectra.

- A more complete study of the dimuon mass spectra, including the low mass vector mesons ρ, ω and ϕ as well as their Dalitz decays, would allow the extension of the present results into the lower mass region. In particular, this might allow to see how the 'excess' evolves into the $\sim$ 1 GeV mass region (and compare with similar results of the HELIOS-3 and CERES experiments). Original results on the relative behaviour of high and low mass resonances, like direct ψ/ϕ ratios, not affected by systematics, might also yield useful information for a more complete and consistent theoretical understanding of such questions as 'J/ψ suppression' and 'ϕ enhancement'. The eventual connection between the 'excess' in S–U relative to the p–A linear extrapolation and the 'ϕ enhancement' (or vice-versa) would also be clarified.

- The most difficult, but very important, upgrade of the data analysis presented in this work, is the development of a multidimensional *acceptance and smearing* correction, to be applied on an event by event basis, as a function of the kinematical variables of the muon pair. This method would allow to transform the measured (mass) spectra in 'source' spectra, whatever are their contributions. This is particularly important to understand the physical origin of a *continuous* and unknown ('excess') process. The method used in the present work, requiring the knowledge of the kinematical distributions of a physical process in order to calculate its acceptance, is clearly unable to deconvolute the detector biases out of an *unknown* contribution. This would allow a much easier comparison between our results and those of theoretical models or of other experiments.

In the present work we have shown that an increase of (open) charm production would provide a good explanation of the excess found in the S–U data. Although other explanations are likely to appear in the near future, it would be extremely interesting to have some absolute and direct measurement of charm production in heavy ion collisions, if possible correlated with the dimuon measurement. The very short $c\tau$ of the D mesons (317 μm) and the large multiplicity of charged particles produced in heavy ion collisions, makes it an extremely difficult experiment. But investigating its feasibility is certainly worth the effort, namely considering the use of some LHC–prototype silicon vertex detector in the context of the NA50 experiment.

"There was a point to this story,
but it has temporarily escaped the chronicler's mind."

—Douglas Adams, *So long, and thanks for all the fish* (1984)
(The fourth book of "The Hitch Hikers' Guide to the Galaxy")

Printed at CERN, on April 24, 1996